Modeling and characterization of micro-porous layers in fuel cells

by

Mehdi Andisheh-Tadbir

M.Sc., Shiraz University, 2011
B.Sc., Shiraz University, 2008

Thesis Submitted in Partial Fulfillment of the
Requirements for the Degree of
Doctor of Philosophy

in the
School of Mechatronic Systems Engineering
Faculty of Applied Sciences

SIMON FRASER UNIVERSITY

Spring 2016

Approval

Name: **Mehdi Andisheh-Tadbir**

Degree: **Doctor of Philosophy**

Title: ***Modeling and characterization of micro-porous layers in fuel cells***

Examining Committee: **Chair:** Jason Wang
Assistant Professor

Erik Kjeang
Senior Supervisor
Associate Professor

Majid Bahrami
Co-Supervisor
Professor

Gary Wang
Supervisor
Professor

Siamak Arzanpour
Internal Examiner
Associate Professor
Mechatronic Systems Engineering

Jon Pharoah
External Examiner
Professor
Mechanical and Materials Engineering
Queens University

Date Defended/Approved: December 2, 2015

Abstract

Modern hydrogen powered polymer electrolyte fuel cells (PEFCs) utilize a micro-porous layer (MPL) consisting of carbon nanoparticles and polytetrafluoroethylene (PTFE) to enhance the transport phenomena of reactants and products adjacent to the active catalyst layers. The use of MPLs in advanced PEFCs has aided manufacturing of higher performing fuel cells with substantially reduced cost. However, the underlying mechanisms are not yet completely understood due to a lack of information about the detailed MPL structure and properties.

In the present work, the 3D phase segregated nanostructure of an MPL is revealed for the first time through the development of a customized, non-destructive procedure for monochromatic nano-scale X-ray computed tomography (NXCT) visualization. Utilizing this technique, it is discovered that PTFE is situated in conglomerated regions distributed randomly within connected domains of carbon particles; hence, it is concluded that PTFE acts as a binder for the carbon particles and provides structural support for the MPL. Exposed PTFE surfaces are also observed that will aid the desired hydrophobicity of the material. Additionally, the present approach uniquely enables phase segregated calculation of effective transport properties, as reported herein, which is particularly important for accurate estimation of electrical and thermal conductivity.

Additionally, two analytical models are developed for estimation of thermal conductivity and diffusivity of MPL, as a function of structural properties, i.e., porosity and pore size. Based on these models, the pore size distribution and porosity of an MPL with a high diffusivity and thermal conductivity is proposed.

Finally, a performance model is developed that is used to study the effects of MPL properties on fuel cell performance. Overall, the new imaging technique and associated findings may contribute to further performance improvements and cost reduction in support of fuel cell commercialization for clean energy applications.

Keywords: Micro-porous layer; thermal conductivity; diffusivity; X-ray computed tomography; degradation; performance

To my beloved parents, my dear brother, my lovely sister and my love Golara

Acknowledgements

This research was supported by the Natural Science and Engineering Research Council of Canada, Automotive Partnership Canada, Canada Foundation for Innovation, British Columbia Knowledge Development Fund, Ballard Power Systems, Mercedes-Benz Canada Fuel Cell Division, and Simon Fraser University. The research made use of facilities at SFU Fuel Cell Research Laboratory (FCReL), Laboratory for Alternative Energy Conversion (LAEC), and 4D LABS as well as at Ballard Power Systems.

I would like to express my sincere gratitude to my supervisors Dr Erik Kjeang and Dr Majid Bahrami for the continuous support of my Ph.D study and related research, for their motivation, and immense knowledge. Their guidance helped me in all the time of research and writing of this thesis.

Besides my direct advisors, I would like to thank Prof Gary Wang, for accepting to be in my committee, reviewing my thesis and giving useful feedback.

Also I would like to appreciate the helps from Dr. Claire McCague at LAEC, Mr Francesco P. Orfino at FCReL, and Monica Dutta at Ballard Power Systems for their help and contribution to this research.

I was lucky enough to be a member of two research teams, FCReL and LAEC, where I was exposed to various research projects and could make good friends. I would like to thank my fellow labmates in both research teams for the stimulating discussions, for their supports, and for all the fun we have had in the last four years.

Last but not the least; I would like to thank my family who has always supported me in all stages of my life in general and my education in particular.

.

Table of Contents

Approval ii
Abstract iii
Dedication iv
Acknowledgements v
Table of Contents vi
List of Tables ix
List of Figures x
List of Acronyms xiii
Executive Summary xiv

Chapter 1. Introduction 1
1.1. Research Importance 1
1.2. Research Motivation 3
1.3. Previous Works 4
1.3.1. Thermal Management Studies 4
1.3.2. Performance Models 5
1.3.3. MPL Properties Characterization 6
1.3.4. Degradation Mechanisms 9
Membrane Degradation 9
Chemical Degradation 10
Mechanical Degradation 11
Catalyst Layer Degradation 11
GDL degradation 12
Electrochemical degradation 13
Mechanical degradation 13
1.3.5. Thermal degradation 14
1.4. Research Objectives 14
1.5. Thesis Structure 15

Chapter 2. Analytical Model for the MPL Effective Diffusivity 17
2.1. Unit Cell Geometry 17
2.2. Heat and Mass Transfer Analogy 21
2.3. Results and Discussion 26
2.3.1. Model Validation 26
2.3.2. Effect of Liquid Water 28
2.3.3. Parametric Study 29
MPL Pore Size Distribution 29
MPL Porosity 32
2.4. Conclusions 33

Chapter 3. Analytical Model for the MPL Effective Thermal Conductivity 35
3.1. Modeling Approach 35
3.2. Experimental Study 40
3.2.1. Sample Specifications 40

3.2.2. Thermal Conductivity Measurements 41
3.2.3. Removing the Contact Resistance Effects 42
3.2.4. Thickness Measurements 43
3.3. Results 43
3.3.1. GDL Thicknesses and Total Resistances 44
3.3.2. Effective Thermal Conductivity of MPL 45
3.3.3. Compact Relationship Development 46
3.3.4. Optimal MPL Structure for Enhanced Heat and Mass Transfer 47
3.4. Conclusions 50

Chapter 4. Three-Dimensional Phase Segregation of MPLs by Nano-Scale X-Ray Computed Tomography 51
4.1. Experimental 51
4.1.1. Sample Preparation 51
4.1.2. Image Acquisition 52
4.2. Results and Discussion 55
4.2.1. Segmentation Analysis 55
4.2.2. Carbon and PTFE Distributions 59
4.2.3. MPL Properties 66
4.3. Conclusions 68

Chapter 5. Evidence for MPL Degradation Under Accelerated Stress Test Conditions 70
5.1. Experimental 70
5.1.1. Samples Specifications 71
SEM Samples 71
XCT Samples 72
5.2. Results and Discussion 73
5.2.1. MPL Thickness Changes 73
5.2.2. Structure Changes 74
5.2.3. BOL and EOL Properties 76
5.3. Conclusions 78

Chapter 6. Fuel Cell Modeling, Part I: Hygrothermal PEFC Model 80
6.1. Model Geometry 80
6.2. Governing Equations 81
6.3. Numerical Scheme 84
6.4. Model Validation 85
6.5. Baseline Case 87
6.6. Conclusions 89

Chapter 7. Fuel Cell Modeling, Part II: Performance Model 90
7.1. Model Geometry 90
7.2. Governing Equations 91
7.3. Numerical Scheme 96
7.4. Model Validation 97

7.5. Case Studies 98
7.5.1. MPL Thermal and Electrical Conductivity 98
7.5.2. MPL Diffusivity 99
7.6. Conclusions 100

Chapter 8. Conclusions and Future Works 101
8.1. Thesis Conclusions 101
8.2. Future Works 102

References 104

List of Tables

Table 2.1. Available relations for the effective diffusivity of a porous medium. 24

Table 2.2. Description of the cases investigated in [112] *. 27

Table 3.1. Specifications of Sigracet® samples used in the present study.*..... 40

Table 3.2. Specifications of an optimal MPL design. 49

Table 4.1. NXCT system imaging conditions for the punched and FIB prepared MPL samples. 54

Table 4.2. Comparison of the punch and FIB lift-out sample preparation techniques for NXCT scanning of MPL materials. 55

Table 4.3. MPL properties for the SGL 24BC GDL calculated numerically based on the 3D reconstructed structure obtained from NXCT..... 68

Table 5.1 Effective oxygen diffusivity and thermal conductivity of BOL and EOL samples* 77

Table 6.1. Operating conditions of the stack used for model validation. 87

Table 6.2. Baseline case conditions. 88

Table 7.1. Dimensions and physical properties of the model components. 91

Table 7.2. The list of governing equations in each computational domain. 92

Table 7.3. Source terms at each zone. 92

Table 7.4. Experimental conditions for the experimental investigation reported in [150]. 98

List of Figures

Figure 1.1. High resolution SEM image from the cross section of a GDL. Image [1]. 2

Figure 1.2. The present research roadmap and deliverables. 16

Figure 2.1. An SEM image from a cross section of an MPL [106]. 18

Figure 2.2. Considered unit cell in the present work. 18

Figure 2.3. Pore size distribution of the MPL used in [45]. 20

Figure 2.4. Comparison of the available diffusivity models in the literature to published data [45,46,112]. 25

Figure 2.5. Steps for calculating the effective diffusivity using the proposed model. 26

Figure 2.6. Comparison of the model results with other diffusivity values from the literature. 28

Figure 2.7. The incremental (a), and the cumulative (b), pore size distributions for the five cases studied in section MPL Pore Size Distribution. 30

Figure 2.8. Effective diffusivity of the MPLs introduced in Figure 2.7. 31

Figure 2.9. Variations of the effective diffusivity at different average pore size. 32

Figure 2.10. Variations of effective oxygen diffusivity by MPL porosity. 33

Figure 3.1. Schematic of the carbon particles of the porous MPL under compression. 38

Figure 3.2. Steps to calculate thermal conductivity using the proposed model. 40

Figure 3.3. Schematic of the sample arrangement in TPS 2500S and the equivalent thermal resistance network. 42

Figure 3.4. (a) Variations of thickness under compression for different GDL types; and (b) total thermal resistance calculated from the raw data from TPS 2500S. 44

Figure 3.5. The measured thermal conductivity of the substrate (▲) and MPL (■), and the MPL thermal conductivity predicted by the present analytical model (line) 45

Figure 3.6. Variations of thermal conductivity at various d* and porosity values. 47

Figure 3.7. Effective diffusivity and thermal conductivity at optimal design points. 49

Figure 4.1. Arrangement of X-ray source, detector, and sample in the ZEISS Xradia 810 Ultra 52

Figure 4.2. Images of reconstructed 2D slices of the (a) punched and (b) FIB prepared MPL samples obtained in HRES mode with 16 nm pixel size and 16 μm field of view. 56

Figure 4.3. (a) Gray scale histogram for the stack of 2D images from the FIB prepared MPL sample and (b) bar chart of threshold values with corresponding porosity values calculated by eleven different auto-thresholding algorithms. 58

Figure 4.4. 3D segmented structure of the solid and pore phases of the MPL. The cube dimension is 1.5 μm and the voxel size is 16 nm. 59

Figure 4.5. Mass attenuation coefficients for carbon and PTFE at different X-ray beam energies [129]. The vertical guidelines indicate the mass attenuation coefficients for carbon and PTFE at 5.4 and 8.0 keV. 61

Figure 4.6. (a) Raw LFOV X-ray image of the cubic MPL sampled prepared by FIB lift-out; and (b) a 2D reconstructed slice of a section of the same sample measured in HRES mode. 63

Figure 4.7. Phase differentiated MPL structure: (a) carbon distribution; (b) PTFE distribution; (c) combined pore, carbon, and PTFE distributions; and (d) 3D structure. Carbon is shown in blue, PTFE in yellow, and pore phase in black. The cube dimension is 1.5 μm and the voxel size is 16 nm. 65

Figure 4.8. Cumulative pore size distribution of the SGL 24BC MPL calculated numerically based on the 3D reconstructed structure obtained from NXCT. 67

Figure 5.1. (a) The prepared sample for the Versa system, mounted on a sample holder; (b) SEM image from one stage of sample preparation for the Ultra system. Notice the significant difference in the sample size for the two instruments. 72

Figure 5.2. (a) Distribution of normalized BOL and EOL MPL thickness; and (b) the normalized mean values of MPL samples. 73

Figure 5.3. Through-plane porosity of GDL for the BOL and EOL samples obtained by using Versa with 0.6 μm voxel size at 50 kV acceleration voltage and 4 W power. The sample structures at the bottom are the binarized images at various cross sections that are highlighted by colored borders corresponding to the colored lines shown in the GDL image at the top. 75

Figure 5.4. MPL pore size distributions for the BOL and EOL samples obtained from reconstructed 3D structure of the samples using Ultra at 16 nm voxel size. Each curve is plotted after averaging the PSD of three cubic domains of 4.5 μm. 76

Figure 5.5. The contact angle for the BOL and EOL samples, measured by static sessile drop technique using a goniometer. 78

Figure 6.1. Model geometry, cell components, and boundary conditions: (a) the actual air-cooled stack (FCgen®-1020ACS); (b) half stack model geometry; (c) half-cell model; (d) detailed view of the cell with the considered components. 81

Figure 6.2 Normalized current density distribution measured at different downstream positions (indicated by the symbols) along the lateral direction (indicated by the dashed line) of a single cell in the center of the stack. 85

Figure 6.3. Temperature distribution at z/z* = 0.88. Square symbols represent experimental data; solid line indicates modeling results with 2D current distribution assumption; and dashed line shows modeling results with 1D current distribution assumption. 86

Figure 6.4. Temperature distribution at z/z* = 0.88 for two stack power levels obtained by the present model (lines) and from the measurements (symbols). 87

Figure 6.5. Simulated (a) temperature and (b) RH contours for the baseline open cathode fuel cell. The modeling domain shown here is the left half of a single cell in the stack. 89

Figure 7.1. Model geometry and the considered MEA components in the model. 90

Figure 7.2. Comparison of the simulated polarization curve with the experimental data of [150]. 98

Figure 7.3. Effects of (a) MPL effective thermal conductivity and (b) MPL electron conductivity on PEFC performance. 99

Figure 7.4. Effects of MPL diffusivity on PEFC performance: (a)polarization curve; (b) cell voltage. 99

List of Acronyms

ACS	Air Cooled Stack
BOL	Beginning of Life
CCM	Catalyst Coated Membrane
CL	Catalyst Layer
EOL	End of Life
FC	Fuel Cell
FCReL	Fuel Cell Research Laboratory
FIB	Focused Ion Beam
GDL	Gas Diffusion Layer
HRES	High Resolution
ICE	Internal Combustion Engine
LAEC	Laboratory for Alternative Energy Conversion
LFOV	Large Field of View
MBFC	Mercedes Benz Fuel Cell
MEA	Membrane Electrode Assembly
MIP	Mercury Intrusion Porosimetry
MPL	Micro-Porous Layer
NXCT	Nano-scale X-ray Computed Tomography
PEFC	Polymer Electrolyte Fuel Cell
PSD	Pore Size Distribution
PTFE	Poly Tetra Fluoro Ethylene
RH	Relative Humidity
SEM	Scanning Electron Microscopy
SIMPLE	Semi-Implicit Method for Pressure Linked Equations
TEM	Transmission Electron Microscopy
TPS	Transient Plane Source

Executive Summary

Motivation

Fuel cells are considered as promising zero-emission "21st century energy-conversion devices for mobile, stationary, and portable power". In order to unlock the far-reaching potential of polymer electrolyte fuel cell (PEFC) technology, a wide variety of research and development activities are currently underway in both industry and academia. Major advances in this field often rely on modeling to guide experimental and development work. The micro-porous layer (MPL) is the most recently added component of the membrane electrode assembly (MEA) in order to facilitate fuel cell operation at high current densities. However, the current fundamental understanding of the MPL and its operational effects is primarily empirical. Therefore, the focus of this research is on the development and utilization of fundamental tools to characterize and evaluate MPL materials for fuel cells.

Objectives

The research objectives can be summarized as below:

- To develop analytical model for the MPL effective diffusivity including the rarefied gas effects (Knudsen diffusion)
- To develop analytical model for the MPL effective thermal conductivity
- To characterize MPL structure and segregate PTFE phase from carbon phase
- To find the possible pathways for MPL degradation
- To develop a numerical model for studying the hygrothermal behavior of low humidity air cooled PEFC
- To predict the changes in the fuel cell performance due to the changes in MPL thermal/electrical conductivity and diffusivity

Methodology

Development and utilization of fundamental tools to characterize and evaluate MPL materials for fuel cells is chosen as the focus of this work. However, to study the

effect of MPL properties on fuel cell performance, which is one of the important metrics in fuel cell industry, a performance model is also developed. Therefore, the project is divided into two main paths: i) development of tools to characterize MPL material; and ii) development of tools to evaluate PEFC performance

On the first path, the several MPL samples are analyzed using nano-scale X-ray tomography. The obtained 3D images of the samples are used to reconstruct the structure;the 3D structures are then segmented , a methodology for separation of different phases in low density materials is developed; and finally the MPL effective thermal conductivity and diffusivity are calculated.. In parallel to that experimental work, two analytical models are developed and validated to estimate the diffusivity and thermal conductivity of MPL. The developed procedure in this path is utilized in studying the MPL degradation process by comparing the structure of a beginning of life (BOL) and end of life (EOL) sample.

The other path has initiated by developing a decoupled hygrothermal model which, due to its limitations, is only used for investigating the temperature and humidity distributions of air-cooled stacks. The model is then upgraded into a simple performance model, where the obtained property values from the first path are implemented in, to predict the performance.

Contributions

The list of contributions resulted from this research is listed below:

- Development of an analytical model for the effective diffusivity of MPL
  - **M. Andisheh-Tadbir**, M. El Hannach, E. Kjeang, M Bahrami, “Analytical modeling of effective diffusivity in micro-porous layers,” 226th ECS conference, October 4-9, 2014.
  - **M. Andisheh-Tadbir**, M. El Hannach, E. Kjeang, M Bahrami, “An analytical relationship for calculating the effective diffusivity of micro-porous layers,” International Journal of Hydrogen Energy 40, 10242-10250.

- Development of an analytical model for the effective thermal conductivity of MPL

- **M. Andisheh-Tadbir**, Erik Kjeang, Majid Bahrami, ‘Thermal conductivity of microporous layers: Analytical modeling and experimental validation,” Journal of Power Sources 296, 344-351.

- Reconstruction of the MPL structure using nano-scale X ray computed tomography and segregation of the three phases
  - **M. Andisheh-Tadbir**, A. Pokhrel, Y. Singh, R. White, M. El Hannach, F.P. Orfino, M. Dutta, E. Kjeang, “Nano-scale X-ray computed tomography of micro-porous layers,” 228th ECS conference October 11-15, 2015.
  - **M. Andisheh-Tadbir**, F.P. Orfino, E. Kjeang, “Three-Dimensional Phase Segregation of Micro-Porous Layers for Fuel Cells by Nano-Scale X-Ray Computed Tomography,” Submitted to journal.

- Finding the possible pathway for MPL degradation
  - **M. Andisheh-Tadbir**, M. Dutta, F.P. Orfino, Erik Kjeang, “Evidence for micro-porous layer degradation under accelerated stress test conditions,” 228th ECS conference October 11-15, 2015.

- Development of a 3D numerical model for low humidity air-cooled stacks
  - **M. Andisheh Tadbir**, A. Desouza, M. Bahrami, E. Kjeang, “Cell level modeling of the hydrothermal characteristics of open cathode polymer electrolyte membrane fuel cells,” International Journal of Hydrogen Energy 39,14993-15004.
  - **M. Andisheh Tadbir**, S. Shahsavari, M. Bahrami, E. Kjeang, “Thermal management of an air-cooled PEM fuel cell: Cell level simulation,” ASME 10th Fuel Cell Science, Engineering and Technology Conference, July 23-26, 2012, San Diego, CA, USA., Paper No. ESFuelCell2012-91440.
  - **M. Andisheh Tadbir**, A. Desouza, M. Bahrami, E. Kjeang, “Thermal design of air-cooled fuel cells,” Hydrogen and Fuel Cells Conference, June 16-19, 2013, Vancouver, Canada.
- Development of a 3D numerical performance model to assess the effects of MPL properties on PEFC performance
  - **M. Andisheh-Tadbir**, Z. Tayarani, M. El Hannach, E. Kjeang, “Effect on MPL properties on PEM fuel cell performance”, Technical report for Mercedes Benz-Fuel Cell
  - **M Andisheh-Tadbir**, Z Tayarani, M El Hannach, E Kjeang, “Impact of micro-porous layer properties on fuel cell performance,” 226th ECS conference, October 4-9, 2014

Chapter 1.

Introduction

1.1. Research Importance

Fuel cell engines, in general, and polymer electrolyte fuel cells (PEFCs), in particular, are potential substitutes for internal combustion engines (ICEs). Their wide range of applicability makes them good candidates not only for stationary power generation but also for mobile applications. FC's theoretical efficiency compared to ICE is significantly higher; FC have the potential of zero-emission power generation; FC's maintenance could be less challenging as its core is free from moving parts; FC's power output is scalable from mW to MW. These appealing features are good reasons to shift towards FC from ICE. However, there are significant challenges to make FCs commercially available, especially in automotive field.

Considering the current stage of FC performance, we are in a good position and the current FC technology is not far from being *mature*. Decades of research and development in this field have led to the existence of high power density stacks with acceptable durability. Any success in this area owes its entity to the numerous investigations done by different researchers all over the globe.

One of the main components of PEFC is the membrane electrode assembly (MEA), which is the fuel cell's heart that contains the anode and cathode electrodes, as well as the membrane. Gas diffusion layer (GDL), as one of the basic elements of MEA, is potentially susceptible to different modes of degradation. GDL, which is shown in Figure 1.1, is typically a dual-layer carbon-based material composed of a macro-porous substrate, which usually contains carbon fibers, binder, and polytetrafluoroethylene (PTFE), and a thin delicate micro-porous layer (MPL), which is usually made of carbon

nano-particles and PTFE. Other types of additives may also be added to these two layers to improve their functionality.

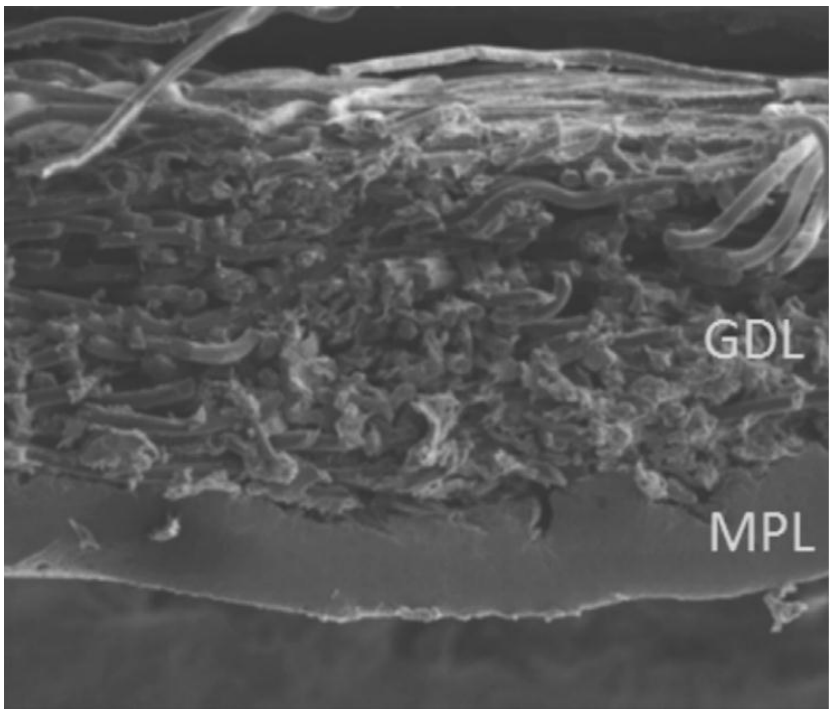

Figure 1.1. High resolution SEM image from the cross section of a GDL. Image [1].

The MPL generally consists of a porous mix of carbon nanoparticles (e.g., carbon black) and a hydrophobic agent such as PTFE. The enhancement achieved in fuel cell performance, which is a major incentive for using this layer, is primarily due to its ability to assist liquid water management by mitigating cathode catalyst layer flooding during high current density operation [2,3]. This is generally attributed to the small pore sizes and hydrophobic nature of the MPL that reduces the risk for liquid water accumulation at the CL-GDL interface. The MPL may also force liquid water to permeate into the membrane, which can improve membrane hydration and ionic conductivity. Furthermore, the MPL is believed to enhance the overall electrical and thermal conductivity of the MEA by reducing the contact resistances between the GDL substrate and catalyst layer [2]; however, experimental evidence of increased thermal resistance has also been reported [1]. Notably, the fundamental understanding of the complex transport phenomena involving the MPL would benefit from detailed information regarding its structure and properties.

In order to unlock the far-reaching potential of PEFC technology, a wide variety of research and development activities are currently underway in both industry and academia. Major advances in this field often rely on modeling to guide experimental and development work. Common modeling approaches in fuel cell science and technology were recently reviewed by Wang [4]. Fuel cell modeling is a complex process, because it deals with multi-scale geometries, electrochemical reactions, mass and heat transfer, and deformation phenomena. A comprehensive fuel cell model should include the transport equations from the nano- and micro-scale catalyst layers, gas diffusion layers, and membrane to mini-scale channels and large-scale stacks with multiple cells with consideration of solid, ionomer, gas, and liquid phases. However, considering the available computational resources, it is not possible to include all the details in such models. Hence, depending upon the fuel cell conditions, the required accuracy, and the aim of the research, different modeling scenarios may emerge. Many research activities to date considered macroscopic modeling [5–10] while others focused on pore scale modeling of different fuel cell components [11–13]. Most established fuel cell models assume fully hydrated membranes and isothermal conditions [14–16] which are generally acceptable for liquid-cooled fuel cells operating under well-humidified conditions. However, such assumptions are not valid for a system that operates on a vehicle in non-ideal conditions.

1.2. Research Motivation

The present research has been performed in collaboration with two local companies: Ballard Power Systems; and Mercedes Benz-Fuel Cell Division (MBFC). At the first stages of this work, the focus was on the hygrothermal management of PEFC stacks by modeling the operation of a low humidity open-cathode stack, i.e., Ballard FCgen®-1020ACS stack. The issues with the open-cathode stacks are more related to the system thermal and hydration behaviour. Appearance of local hot spots and dry regions inside the MEA, as well as non-uniformity of the temperature and humidity distribution can lead to low performance of fuel cell and reduce the lifetime. Therefore, the incentive was to find some strategies to cool down the system, while keeping the temperature gradients inside the stack low. This motivated us to develop a numerical

tool that can help resolving the hygrothermal issues in low humidity PEFCs, and furthermore, upgrading the model to predict the performance for various operating conditions.

Meanwhile, through our collaboration with industry and the conducted literature review, we found the challenges facing the cost and durability of PEFCs are amongst the hottest research topics in the field. MPL is a recent addition to the MEA, and therefore literature lacks from fundamental studies on this particular layer. The available models in the literature for predicting MPL properties are not specifically developed for MPL, and still there is not a good understanding of its structure. In addition to the aforementioned lack of knowledge in the field, the increase in application of MPL in almost all types advanced PEFCs was a persuading incentive for focusing on characterization of this thin layer and investigation of its properties on fuel cell performance.

1.3. Previous Works

PEFC modeling is an active field of research in which various engineering disciplines are involved. This section is divided into four sub-sections: thermal management studies, performance models, MPL properties models, and the literature on degradation mechanisms.

1.3.1. Thermal Management Studies

Thermal management, which is often done by appropriate design of the bipolar plates and cooling channels in stack level and by advanced design of MEA components in MEA level, is a necessity for PEFCs. Heat generation inside the cells and its distribution could result in different thermal behavior of the stack. Ju *et al.* [17] examined different heat generation mechanisms in a single channel PEFC. Their model was accurate in predicting the thermal behavior on the single-channel level; however, it could not capture the temperature or RH gradients on the cell level. Bapat and Thynell [18] studied the effects of anisotropic thermal properties and contact resistance on the temperature distribution using a two-dimensional single-phase model based on a single channel domain, but did not investigate the effects of those properties on the RH

distribution. This approach was experimentally examined by Matian *et al.* [19]. Wider cooling channels were shown to enhance the rate of heat transfer from the stack with the tradeoffs of reduced mechanical stability and increased complexity of plate design and manufacturing. The Ballard Nexa stack pioneered the use of air cooling through a separate flow field configuration [20]. However, due to their complexity, the Nexa stack was replaced with the modern Ballard FCgen®-1020ACS stack with combined cathode air supply and cooling channels. Alternative strategies are also available in the literature that may increase the complexity of the stack design and operation under transient conditions [21,22].

Another important phenomenon that occurs more often in low humidity operating conditions (e.g., air-cooled stacks) is membrane dehydration. Membrane water content, which is a function of water activity, will directly affect proton conductivity [15] and consequently ohmic losses. It is shown in [23] that low humidity operation will reduce the overall fuel cell performance. Therefore, self-humidifying MEAs should be utilized to avoid membrane dehydration. A vast amount of research is focused on water transport modeling and water management in PEFCs. These investigations are mostly directed towards resolving the flooding issues under high humidity conditions [24,25] in order to increase power density. In air-cooled fuel cells, however, drying is more critical than flooding. Zhang *et al.* [26] compared the fuel cell performance obtained experimentally with fully humidified and completely dry gases under isothermal conditions, and found that the cell performance decreased at dry conditions due to poor ionomer phase proton conductivity. It was also demonstrated that cell operation at a combination of dry gases and high temperature was particularly challenging. No such studies have been reported for open cathode and/or air-cooled PEFCs, known to operate under dry, *non-isothermal* conditions, as observed before by our colleagues at FCReL [27].

1.3.2. Performance Models

Performance modeling of PEFC has been an active research area for the past decades. Performance of a PEFC is usually characterized by a polarization curve that represents the generated current at various cell voltages. In these models, depending on the complexity of the implemented approach and the required output, various physics

may be included or excluded. In general, to predict the PEFC performance, flow of reactant gases inside the channels, porous GDLs and catalyst layers need to be solved. Additionally, the transport of heat, electrons, protons, liquid water, and the dissolved water inside the membrane should be modeled coupled with the flow domain to have an accurate prediction of performance.

The first models in the literature were mostly steady state, one dimensional, and isothermal. By the improvements in the computational resources, more complicated models emerged. Springer and Gottesfeld [28] performed a 1D steady state and isothermal study on fuel cell performance assuming pseudo-homogeneous catalyst layer structure at high current densities and neglected the effects of liquid water. Several authors focused only on the cathode catalyst layer [29–31] using 1D steady state isothermal models. Some other researcher tried to model the two phase flow inside the MEA [32,33]. In the latter works, the models were two-dimensional and two-phase but only the cathode side was modeled. Recently, complex three-dimensional models of PEFCs become popular as the computational resources advance dramatically [7,34–37]. Apart from the challenges regarding the electrochemistry and stability of the numerical model, modeling the liquid water transport inside the porous material is a difficult task. Several approaches can be used to address the liquid water transport. In this research, mixture model is used to solve the transport of liquid water inside the porous GDL and catalyst layer [38].

1.3.3. MPL Properties Characterization

Wide application of the MPL in recent MEAs dictates the need for accurate models for estimating its transport properties. However, since the MPL is a recently developed material, the number of published works with the focus on this thin and delicate layer is limited [39–45]. The number of publications are even less if one is looking for the effective transport properties, i.e., thermal/electrical conductivity, diffusivity, etc. [45–47]. Measuring the MPL properties is a challenging task since the MPL needs a physical support and cannot be analyzed as a separate layer [46]. Similar to its measurements, modeling the MPL properties is also a difficult task [45,48], since it involves the reconstruction of the complex structure numerically and solving the diffusion

equation in the nano-scale pores where the continuum assumption may be invalid and the Knudsen diffusion may prevail. Usually, complex numerical algorithms are employed to reconstruct a small portion of the MPL. This step is followed by a computationally intensive stage to solve the diffusion equations inside the void spaces of the reconstructed domain [45]. Although this approach leads to reliable and accurate results, an analytical relationship that correlates certain design parameters to the MPL diffusivity could be helpful and requires much less computational efforts. Present relationships are either based on the effective medium theory [49,50], pore network models [51], percolation theories [52], or stochastic-based numerical modeling [53]. However, none of the existing methods is capable of providing an accurate, generally applicable function for the MPL properties. Unit cell approach is another way of modeling the transport properties of porous materials. A unit cell is a simple geometry that inherits the most important specifications of a porous medium and roughly represents the entire medium structure. This approach is previously used by our colleagues in [1,54] to model the thermal conductivity of GDL and it is proven to be applicable to model the transport properties of the fuel cell components.

Porosity and pore size distribution (PSD) are the two main quantities that reveal important information about the pore structure of porous media. In the case of the MPL, mercury intrusion porosimetry (MIP) and focused ion beam integrated with scanning electron microscopy (FIB-SEM) have been used to experimentally measure these quantities [45,48]. MIP is the most commonly used method to measure porosity and PSD, but requires the MPL to be coated on a non-porous, rigid substrate for direct measurements [45], which may lead to inconsistencies compared to the MPL in its intended configuration coated on a macro-porous GDL substrate. It is noteworthy that extraction of MPL-specific information from MIP measurements on full GDLs (i.e., substrate coated with MPL) has proven difficult and inaccurate [45,55]. Alternatively, the FIB-SEM technique can be used to characterize the structure of porous fuel cell components [45,48,56,57]. In this approach, a stack of SEM images from successively FIB milled slices of a sample is used to reconstruct the three-dimensional structure of the porous medium. The resolution of the 2D images obtained by this method can be as high as a few nm, but an important concern is the amount of ion beam damage to the structure. It is known that the ion beam, even at a low beam current, can melt the

structure at the focal position and thereby alter the sample structure and associated images [58,59]. Additionally, it is not possible to distinguish the carbon and PTFE phases using this approach, due to a lack of image contrast.

X-ray computed tomography is a non-destructive technique used to obtain the 3D structure of porous materials from high quality 2D images on the micro- and nano-scales. In this technique, the sample is placed on a rotating stage between an X-ray source and a detector and 2D radiographs from the sample are captured as the sample is rotating. The entire stack of 2D radiographs is then used to reconstruct the 3D geometry of the sample using complex image processing algorithms. X-ray computed tomography using either a laboratory scanner or a synchrotron X-ray source has recently been used for the visualization of fuel cell components, most commonly for micro-scale analysis of the GDL substrate and for liquid water visualization. A 35 keV monochromatic synchrotron X-ray source was used in [60] to observe the GDL structure, as the first step of *in situ* liquid water visualization. The effects of compression on the GDL structure [61,62], spatial variation of substrate porosity [63,64], *ex situ* liquid water intrusion [65,66], and the impact of MPL thickness on the liquid water distribution [67] have also been assessed. Damage induced by the high-intensity synchrotron radiation leading to PEFC performance degradation has however been observed [68]. In contrast to micro-scale imaging of the GDL substrate, higher resolution is required to observe the nano-scale features of the CLs and MPLs. For this purpose, a laboratory system for nano-scale X-ray computed tomography (NXCT) was recently used to image and reconstruct the 3D structure of a CL [58,69]. The reliability of this approach was assessed by comparing the NXCT images with transmission electron microscopy (TEM) images [58]. To the best knowledge of the authors, only one similar study on the MPL has been published to date [70], which focused on a comparison of NXCT and FIB-SEM imaging capabilities. The MPL tortuosity, structural diffusivity (without considering the Knudsen effects), and pore size distribution were calculated based on the structures obtained from FIB-SEM and NXCT techniques [70]. Other MPL properties such as electrical and thermal conductivity have been estimated based on FIB-SEM data [45,71] or analytical models [72,73]; however, none of the aforementioned studies have been able to identify the PTFE phase of the MPL, and therefore, the reliability of the obtained structures and properties is highly uncertain.

1.3.4. Degradation Mechanisms

High-volume fuel cell production and commercialization may not be achieved unless durability challenges are addressed. Degradation of fuel cell components results in cell voltage drop rates between 2-60 $\mu V\ h^{-1}$ [74]. Various mechanisms for degradation of fuel cell components have been recognized by different researchers [75]. Researchers in our group, FCReL, have recently investigated various membrane degradation mechanisms and proposed new strategies to increase the membrane lifetime. Wong and Kjeang [76] assessed chemical degradation of membrane due to Fenton's reaction and found high cell voltages (>0.7V) can increase membrane degradation rate up to ten folds. Chemical and mechanical degradation of catalyst coated membranes and their effects on water sorption was studied in [77]. Sever membrane thinning was observed during the accelerated stress tests (AST) and reduced amount of ionomer mass fraction unveiled material loss due to relentless chemical/mechanical membrane degradation [77]. Decay in mechanical properties of catalyst coated membrane, due to combined chemical and mechanical degradation, was also examined in [78], and an increase in the brittleness of membrane was detected. Enhanced stability of fuel cell membranes owing to Pt-in-membrane bands was also observed in [79]. Corrosion of carbon particles, as another mode of degradation, can affect pore morphology and surface characteristics [80]. Highest corrosion rates occur at potentials higher than 0.8V. This failure mode mostly appears in start-stop cycles of automotive fuel cells, where the cathodic cell potential can be as high as 1.4V [81]. More comprehensive reviews on degradation of fuel cell components can be found in [82–87].

Durability assessment of PEFC is usually performed by running accelerated stress tests (AST). In ASTs, fuel cell components are being examined under harsh operating conditions (e.g., high temperature and relative humidity) and degradation rates or fuel cell lifetime is estimated by statistical analysis and data fitting to aging models [74].

Membrane Degradation

To compete with the internal combustion engines, fuel cell membrane needs to survive at least 10 years (5500 h) in a vehicle. Three modes of membrane degradation

are often mentioned throughout the literature; a) chemical, b) mechanical, and c) shorting. Each of these degradation modes is mitigated utilizing various approaches. Using stabilizing additives to the membrane, manufacturing of reinforced membranes, and applying thick MPL coatings on the substrate to cushion the topographical irregularities of substrate (to reduce the risk of shorting), are some examples of the techniques being used for mitigating membrane degradation. In the following subsections each of these degradation modes are introduced and discussed in more details.

Chemical Degradation

Chemical degradation of membrane is a time dependent process and it has been recognized as “a primary life limiting process” in PEM fuel cells [82]. This process can be distinguished by monitoring CO_2, H_2SO_4, and mainly HF emissions from the outlet gases. However, this may not be the best indicator of failure, as highly localized membrane degradation can also result in membrane failure with no significant HF emission. It is observed that a uniformly degraded membrane did not fail even after 50% inventory loss [82].

It is indicated in [95,96] that the hydroxyl radical (OH), hydroperoxyl radical (OOH), and hydrogen peroxide (H_2O_2) detected directly or indirectly during fuel cell operation are the main reason for chemical degradation of membrane. Among these radicals, OH is the most reactive one and it may react with weak chemical bonds in both main chain and side chain of the membrane.

To mitigate the chemical degradation, complete elimination of harmful OH radicals is extremely difficult. However, OH radicals can be scavenged before inducing damage to the membrane. This should be done through another reaction that has higher kinetic rates than the reaction of OH with the reactive groups of degrading membrane. It is reported in literature that Ce^{3+}, Mn^{2+}, and their metal oxides are good mitigating agents of membrane chemical degradation [97–99]. However, high concentrations of metal ions in the membrane can result in performance drop due to the replacement of acidic protons by these ions. It is shown that 5 mol% Ce^{3+} loading enhances life considerably while does not drop the performance significantly.

Mechanical Degradation

Mechanical stresses induced by expansion/contraction of membrane during fuel cell operation are the potential initiators of mechanical degradation of membrane. Fluctuations in fuel cell operating conditions, which have their origin in various power demands, lead to initiation and propagation of micro cracks in the membrane. One of the main driving forces for the mechanical membrane degradation is the hygrothermal stresses. Therefore, to mitigate mechanical degradation usually it is tried to reduce these types of stress and reinforce the membranes against them.

Manufacturing composite membranes with a reinforcement layer is one way of reducing hygral expansion and increasing membrane strength (e.g., Gore-Select® 5720). These membranes are fabricated by blending polyelectrolytes with elastomers such as PVDF, or ceramics such as silica, alumina, titania, and zeolites. Other approaches for mitigating membrane mechanical degradation are controlling fuel cell operating conditions and designing a fuel cell appropriately. High rates of humidity cycling or higher operating temperatures affect fuel cell life adversely [100]. Moreover, it is shown in [44] that narrower flow field channels are beneficial to reducing membrane mechanical degradation rate. Furthermore, membrane manufacturing process can also affect its durability. It is shown experimentally that extruded polymeric membranes have superiority to solution cast membranes; however, the exact reason is yet unknown [82]. The latter item is a potential time independent degradation process.

Catalyst Layer Degradation

The catalyst layer is one of the most important components within the MEA, and electrochemical degradation of PEM fuel cells was the subject for a vast number of publications since the early 1960s. So far, carbon-supported Pt is known as the most popular catalyst for PEM fuel cells due to its low over potential and high catalytic activity for both hydrogen oxidation reaction (HOR) and oxygen reduction reaction (ORR). The main reason for Pt catalyst degradation is reported to be the loss of active sites and surface area as a result of either dissolution, particle growth, or erosion/corrosion during operation [101]. Hence, the degradation process for the catalyst can be regarded as time dependent degradation. Besides from the Pt catalyst, carbon support and ionomer may

face degradation as well. For the ionomer phase, degradation mechanisms are similar to those of membrane degradation [85,102] as outlined in section “Membrane Degradation” Hence, only the carbon support degradation is discussed in this section.

Corrosion and oxidation of carbon support is one of the key catalyst layer degradation mechanisms and considered a time dependent process. Corrosion of carbon support in the catalyst layer can lead to membrane delamination and this can result in inability of protons to reach the catalyst nano particles [101]. Moreover, carbon corrosion can lead to Pt particles being unanchored from the carbon. This leads to migration of Pt within the MEA by water, and as a result, Pt loss from the MEA or Pt agglomeration can happen. The main mitigation strategy for carbon support degradation is focused on novel material development [101]. Besides from that, modification of heat treatment process can also increase the stability of Pt/C catalyst.

GDL degradation

Reconstruction of GDL (substrate and MPL) structure and evaluation of its properties were appealing topics of investigation recently [12,45,48,53,71,88]. Degradation of GDL, on the other hand, has not been given the required attention. GDL degradation is usually characterized by the changes in its properties (e.g., porosity, pore size distribution, thickness, hydrophobicity). It is stated in [75] that the changes in GDL properties can be mostly attributed to the MPL. Structure of MPL is prone to change due to erosion from mechanical/thermal stresses [89,90] or from corrosion due to electrochemical mechanisms [40,91–93]. Corrosion of carbon particles in the MPL was between 15-20% of the total amount of corrosion in the MEA over short corrosion times [40]. PTFE and carbon loss as a result of corrosion/erosion may lead to reduction in hydrophobicity and electrical/thermal conductivity [85]. The structure of GDL/MPL may also be weakened due to material loss that can be caused by freeze/thaw cycles [94] or even corrosion/erosion [89].

Electrochemical degradation

Electrochemical degradation of GDL can be mostly attributed to the time dependent carbon corrosion process. Carbon is thermodynamically unstable under cathode conditions of PEFC. Carbon is oxidized to CO_2 above 0.207 V vs. SHE. In GDL, corrosion of carbon alters the surface characteristics and morphology [92,93], and is expected to particularly affect the MPL structure. Moreover, decrease in rigidity and increase in strain under PEM fuel cell clamping pressure due to electrochemical degradation is reported in [103].

Various reactions for carbon corrosion are identified in the literature. Water vapour, OH radicals, and Pt, which are available in a PEFC, are the common species in many of these reactions. Depending on the location of carbon (catalyst layer, MPL, or substrate) different carbon corrosion mechanism exists. Compared to the substrate, in the MPL, which is adjacent to the catalyst layer, more degradation is probable as there are both Pt particles and OH radicals that enhance corrosion process.

Mechanical degradation

GDL mechanical degradation is caused by clamping pressure, erosion by reactant and water flows, and water freezing at low temperatures. GDL thickness change under high compression clamping pressure can be permanent [104], which can be referred to as time independent degradation. Any change in the structure of GDL may lead to property changes and can be considered as degradation. The hydrophobic coating may deteriorate after high clamping pressures [105]. Drop in hydrophobicity can also occur due to loss of PTFE from MPL after the surface is being eroded by the flow of liquid water. High flow rates and high temperatures increase the rate of erosion. Erosion leads to increased electrical resistance and porosity. It is shown in [89] that the fuel cell performance with eroded GDLs at low current densities is comparable to that of a fresh GDL; however, at high current densities concentration losses increase significantly.

1.3.5. Thermal degradation

Freezing conditions during the fuel cell start-up and hot pressing during the MEA manufacturing process result in weakening of substrate and MPL structures in the form of time dependent and time independent processes, respectively. This will lead to material loss of either PTFE or carbon by erosion during fuel cell operation [94]. Thermal degradation in GDL happens mostly due to freeze/thaw cycles. Trapped pools of water can also cause thermal degradation of GDL. This means that any kinds of cracks and holes that have emerged during the manufacturing process may initiate such degradation (time independent).

1.4. Research Objectives

In the previous sections, some of the challenges facing fuel cell research were briefly introduced. The motivations for performing the present research were also explained. In this section, the main objectives of the research and the roadmap to achieve those goals are described. Then the physics of the proposed problem is elucidated and the approaches taken to address the issue are clarified.

As described earlier, the focus of this research is on the development and utilization of fundamental tools to characterize and evaluate MPL materials for fuel cells. Based on this goal and the aforementioned motivations, several objectives are chosen to follow in this thesis. The first objective is to develop analytical models for estimation of MPL effective diffusivity and thermal conductivity based on the structural information. The analytical model is based on unit cell approach and includes the effects of rarefied gas in the nano-scale pores. The second objective is to characterize MPL structure by using nano-scale computed tomography. It is tried to segregate PTFE phase from carbon phase. Therefore, the obtained structure has three phases: carbon, PTFE, and void. The most accurate MPL thermal conductivity and electrical conductivity, which can be impacted by the PTFE content and distribution, will also be reported. The next objective is to find possible pathways for MPL degradation by comparing the structures and properties of BOL and EOL MPL samples. Developing numerical models for predicting fuel cell performance and studying PEFC behaviour under various conditions

and MPL properties is the final objective of this research, for which two different models are developed. One is a decoupled hygrothermal model, that is used to study the thermal and hydration behavior of a low humidity air-cooled stack, and the second one is a fully coupled model that is used to predict PEFC performance for various MPL properties.

1.5. Thesis Structure

A roadmap of the project is shown in Figure 1.2. Two main paths of the present research is depicted in this figure with their required steps. The right side steps are covered in Chapter 2 to Chapter 5 and the steps on the left path are covered in Chapter 6 and Chapter 7.

The developed analytical models for the effective diffusivity and thermal conductivity of MPL are explained in Chapter 2 and Chapter 3. Chapter 4 and Chapter 5 describe the MPL structure evaluation techniques. The developed approach for segregation of various phases in MPL is presented in Chapter 4 and the possible degradation pathway for MPL is suggested in Chapter 5. Chapter 6 discusses the developed hygrothermal model which is used to assess hygrothermal characteristics of low humidity air-cooled stacks and Chapter 7 presents the model that is used for performance prediction. Finally in Chapter 8, summary of findings, conclusions, and the future works are explained.

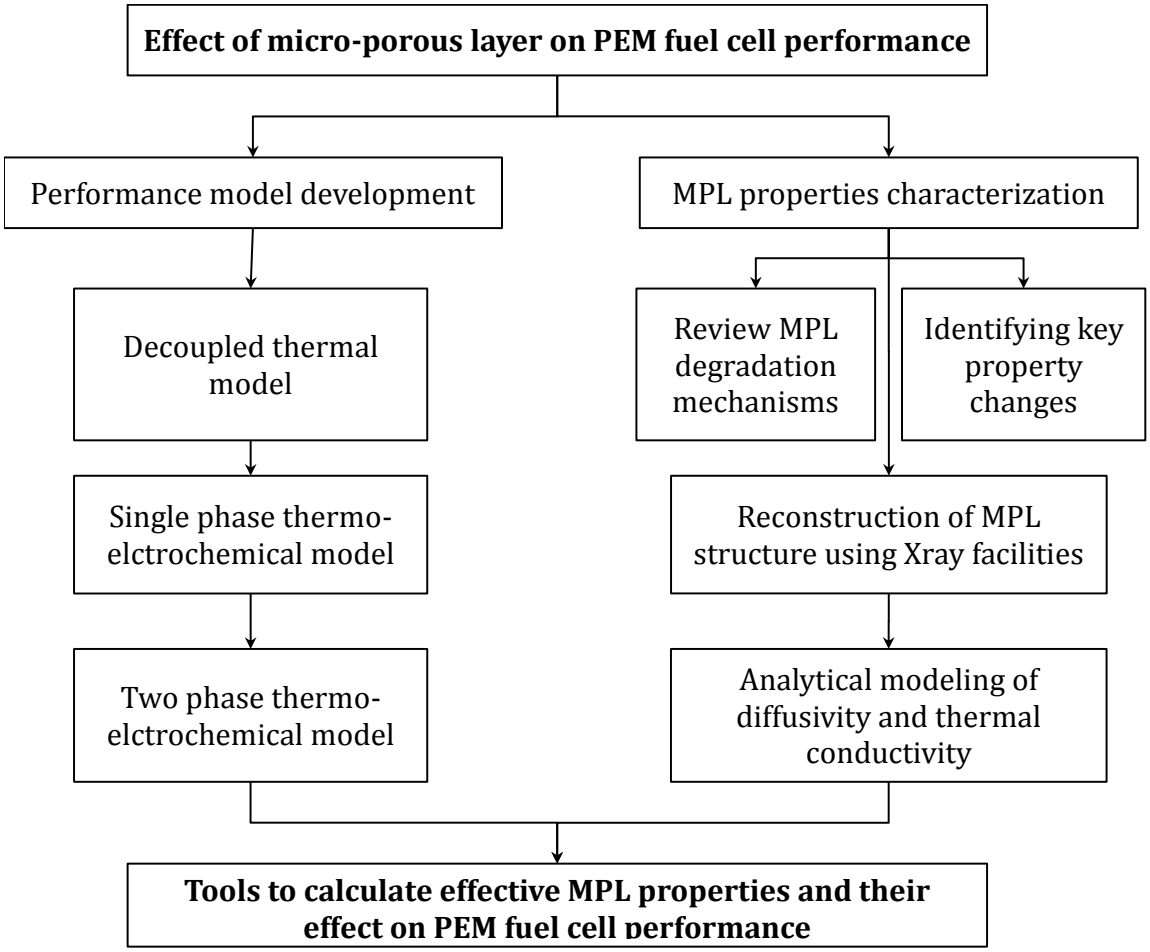

Figure 1.2. The present research roadmap and deliverables.

Chapter 2.

Analytical Model for the MPL Effective Diffusivity

Details of the developed model for estimation of the MPL effective diffusivity is explained in this chapter. This model can be used to calculate the effective MPL diffusivity based on pore size distribution and porosity. Mathematical model is explained in section 2.1 and 2.2. Then in section 2.3, the model is validated against the available data in the literature and a parametric study is performed on the model parameters and section 2.4 summarized the findings.

2.1. Unit Cell Geometry

A fully analytical solution of the mass transport equation inside a randomly structured porous material is not feasible. Simplifying assumptions are therefore required to derive an analytical model for predicting the transport properties of porous structures. In this work, the unit cell approach is used for modeling the effective diffusivity of MPL. Scanning electron microscopy, SEM, images from the surface and cross section of MPL helped us selecting a simplified geometry that represents the MPL structure. Fig.1 shows an SEM image from the cross section of a typical MPL [106]. The structure of the MPL is complex and random; however, it is possible to divide structure into two domains: domain I that constitutes of large pores and domain II that is the packed bed of agglomerates surrounding those large pores. In Figure 2.1 circles show the large pores (domain I) and their surrounding squares represent the packed bed of agglomerates (domain II).

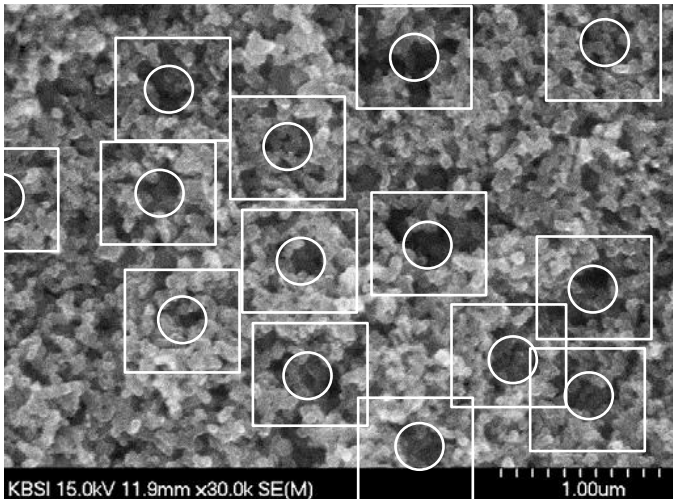

Figure 2.1. An SEM image from a cross section of an MPL [106]**.**

In this investigation, a unit cell is devised that has both of these domains. The considered unit cell, which is shown in Figure 2.2, is a cube that has a spherical pore with diameter d_I in the middle. The sphere is domain I, and its surrounding region in domain II, which is a homogeneous porous zone with the porosity of ε_{II} and the pore size of d_{II}. The relationship between the overall MPL porosity and the unit cell dimensions is found from the geometrical interrelations.

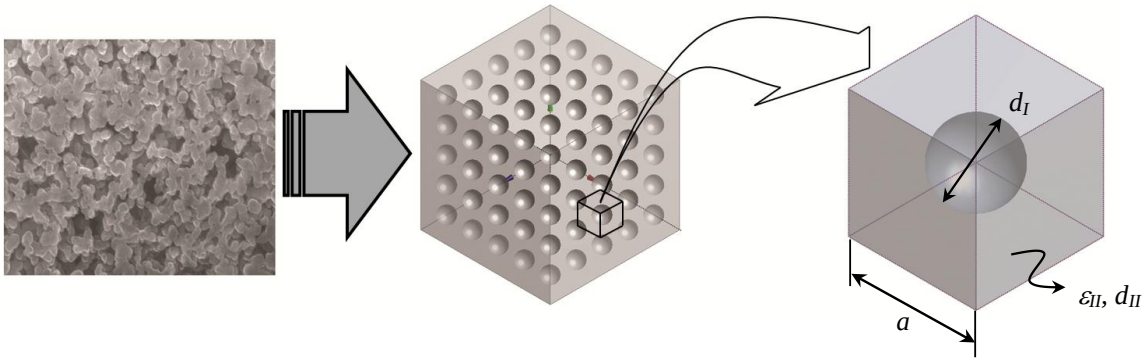

Figure 2.2. Considered unit cell in the present work.

$$\varepsilon_{MPL} = \frac{V_{void}}{V_{tot}} = 1-(1-\varepsilon_{II})\left[1-\frac{\pi d_I^3}{6a^3}\right] \quad (1)$$

In Eq. (1), the secondary domain's porosity, ε_{II}, primary pore diameter, d_I, and unit cell length, a, are unknown. Once the pore size distribution is known, these parameters can be calculated through a procedure that will be explained in the following paragraphs.

The average pore size for a porous zone can be found based on the probability density function of its pores. Hence, the average MPL pore size in this work is obtained from the following relationship.

$$d_{avg} = \sum_j f d_j = \sum_j \frac{V_{inc}^j}{V_{tot}} d_j \tag{2}$$

In Eq. (2), f is the probability of having a pore with diameter d_j, which is the ratio of the incremental pore size (V_{inc}^j) to the total volume of the pores V_{tot}. The information regarding the incremental and total pore volumes is obtained from the porosimetry measurements, e.g., by mercury intrusion porosimetry.

To associate the physical structure to the present model, d_I and d_{II} are needed to be defined and determined from the pore size distribution. The primary domain diameter, d_I, is defined as the average size for the pores that are larger than d_{avg}, in a similar fashion the secondary pore diameter, d_{II}, is the average size of the pores that are smaller than d_{avg}. Therefore, the three characteristic lengths, d_{avg}, d_I, and d_{II} are found respectively from the total average pore size, upper side average pore size, and lower side average pore size. As an instance, the pore size distribution of the MPL studied in [45] is shown in Figure 2.3. Indicated in Figure 2.3 are the average, primary, and secondary pore sizes, i.e., 125, 191, and 76 nm.

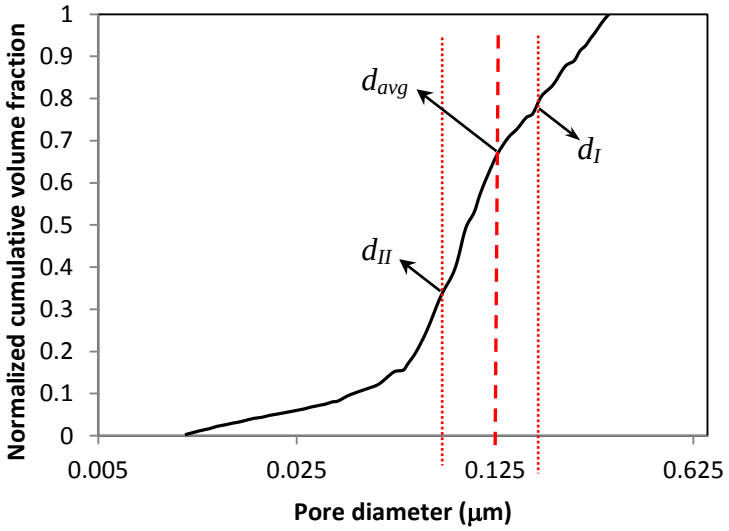

Figure 2.3. Pore size distribution of the MPL used in [45]**.**

Note that in this work an MPL is modeled by a unit cell that has only two distinct pore sizes. So the pore size distribution for the considered unit cell has only two values d_I and d_{II}. Substituting these two pore sizes in Eq. (2) leads to a relationship between the pore size and other model parameters.

$$d_{avg} = \frac{V_{inc}^{I}}{V_{tot}} d_I + \frac{V_{inc}^{II}}{V_{tot}} d_{II} = \frac{\frac{\pi}{6} d_I^4 + \varepsilon_{II}\left(a^3 - \frac{\pi}{6} d_I^3\right) d_{II}}{\frac{\pi}{6} d_I^3 + \varepsilon_{II}\left(a^3 - \frac{\pi}{6} d_I^3\right)} \tag{3}$$

Simultaneous solution of Eqs. (1) and (3) gives the unit cell dimension, *a*, and the secondary zone porosity, ε_{II}. The porosity of the secondary zone, which is an effective porous medium around the primary domain, should be always smaller than or equal to the MPL porosity.

$$\varepsilon_{II} = \frac{(d_I - d_{avg})\varepsilon_{MPL}}{(d_{II} - d_{avg})\varepsilon_{MPL} + (d_I - d_{II})} \tag{4}$$

$$a = d_I \left(\frac{\pi}{6\left(1 - \frac{\left(1-\varepsilon_{MPL}\right)}{1-\varepsilon_{II}}\right)} \right)^{\frac{1}{3}} \tag{5}$$

2.2. Heat and Mass Transfer Analogy

After finding all the required geometrical parameters from the previous steps, in this section the details of the diffusivity model is explained. The effective diffusion coefficient can be calculated by using the analogy between the heat and mass transfer. The governing equation for the diffusion of heat or mass is the Laplace's equation with a diffusion coefficient, which is thermal conductivity for the transport of heat and mass diffusion coefficient for the transport of mass. Hence, using the heat conduction solution and replacing thermal conductivity with diffusivity, one can find the solution for the mass diffusion for the same geometry and similar boundary conditions. The effective thermal conductivity of a solid sphere embedded inside a cube is obtained analytically in [107] and is shown in Eq. (6).

$$k_{eff} = \frac{3k_c k_s \alpha + (2k_c + k_s)k_c(1-\alpha)}{3k_c \alpha + (2k_c + k_s)(1-\alpha)} \tag{6}$$

In Eq. (6) k_s and k_c are the thermal conductivities of sphere and cube, and α is the volume fraction of the sphere in the entire medium and is calculated as follows.

$$\alpha = \frac{\pi}{6}\left(\frac{d_I}{a}\right)^3 \tag{7}$$

Replacing the thermal conductivities with the diffusion coefficients of domains I and II , provide us with the desired relationship for the effective diffusivity of the unit cell.

$$D^i_{eff} = \frac{3D^i_{II} D^i_I \alpha + (2D^i_{II} + D^i_I)D^i_{II}(1-\alpha)}{3D^i_{II} \alpha + (2D^i_{II} + D^i_I)(1-\alpha)} \tag{8}$$

where D_{eff}^{i} is the effective diffusivity of species *i* through the MPL, D_{I}^{i} is the gas diffusion coefficient in domain *I* (the spherical pore), and D_{II}^{i} is the gas effective diffusion coefficients of the i^{th} species in domain *II* (the effective porous medium around the domain *I*).

To calculate the gas diffusion coefficient in domain *I* and *II*, the diffusion regime needs to be determined. Diffusion mainly occurs due to collision of gas molecules to each other and to the pore walls. The former is called bulk diffusion and the latter is called Knudsen diffusion. To determine the appropriate diffusion mechanism in a medium, Knudsen number is calculated through Eq. (9).

$$Kn = \frac{\lambda}{l} \tag{9}$$

In Eq.(9), λ is the mean free path of gas molecules and l is the characteristic length scale of the medium. When Kn<<1, we are in continuum regime and the diffusion process is dominated by the bulk diffusion. Conversely, when Kn>>1 the diffusion process is dominated by the Knudsen diffusion. In the MPL, the pore sizes are in the range of 20 to 300 nm. Considering the mean free path of 63 nm for oxygen at standard conditions [108], Knudsen number is found to be ~0.2-3.0. This implies that the transport of species inside the MPL is occurring in the mixed diffusion regime, where both Knudsen and bulk diffusion are contributing to the diffusion phenomenon.

Eq. (10) shows the Bosanquet's formula [109], which is used in this work to calculate the diffusion coefficient in the mixed diffusion regime.

$$D_i = \left[\frac{1}{D_i^b} + \frac{1}{D_i^{Kn}} \right]^{-1} \tag{10}$$

Bulk diffusion coefficients for different species can be found in the open literature as functions of pressure and temperature. For instance, bulk diffusion coefficient for an oxygen-nitrogen pair at different pressures and temperatures can be found from Eq. (11) [110],

$$\ln(pD_{O_2}^b) = \ln(1.13\times10^{-5}) + 1.724\ln T \tag{11}$$

where p is the pressure in [atm], T is the gas temperature in [K], and $D_{O_2}^b$ is the bulk diffusion coefficient of oxygen in [$cm^2\ s^{-1}$].

To obtain the Knudsen diffusion, Eq. (12) is used [111], in which d is a characteristic length scale of the medium, R is the universal gas constant, and M_i is the molecular mass of the i^{th} species.

$$D_i^{Kn} = \frac{4}{3} d \sqrt{\frac{RT}{2\pi M_i}} \tag{12}$$

D_I, which is the gas diffusion coefficient of the stored gas inside the primary pore, can be obtained by substituting Eq. (12) in (10) with d_I as the pore size. Therefore, D_I can be found from the following.

$$D_I^i = \left(\frac{1}{D_b^i} + \frac{3}{d_I} \sqrt{\frac{\pi M_i}{8RT}} \right)^{-1} \tag{13}$$

The effective gas diffusion coefficient in domain *II*, D_{II}, needs to be calculated from the available relationships for the effective diffusivity for packed beds. Several equations are available in the literature for estimating the effective diffusivity inside a porous material. Some of the most common ones are listed in Table 2.1. In Table 2.1, D is the diffusion coefficient of the gas inside the pores and D_{eff} is the effective diffusion coefficient in the porous medium. Therefore, for a medium with large pore size, where Kn<<1, D is the bulk diffusion; for a medium with Kn ~ 1, D should be calculated through Eq. (10); and for a medium with very small pore size, where Kn>>1, D should be obtained from Eq. (12). In this work to estimate the effective diffusivity in domain *II*, the formula proposed by Mezedure et al. [51] is utilized. This formula is obtained for various size spherical particles and as it is discussed later in this paper, it gives the closest values to the published data in the literature.

Table 2.1. Available relations for the effective diffusivity of a porous medium.

Reference	Relationship	Note
Bruggeman [49]	$D_{eff} = D\varepsilon^{1.5}$	Packed spherical particles
Mezedur et al. [51]	$D_{eff} = D\left[1-(1-\varepsilon)^{0.46}\right]$	Multi length scale particle based porous media
Tomadakis and Sotirchos [52]	$D_{eff} = D\varepsilon\left(\frac{\varepsilon-0.11}{1-0.11}\right)^{0.785}$	Fibrous porous media
Neale and Nader [50]	$D_{eff} = D\left(\frac{2\varepsilon}{3-\varepsilon}\right)$	Packed spherical particles
Zamel et al. [112]	$D_{eff} = D\left(1-2.76\varepsilon\cosh(3\varepsilon-1.92)\left[\frac{3(1-\varepsilon)}{3-\varepsilon}\right]\right)$	Fibrous gas diffusion layers

Figure 2.4 presents the predicted effective diffusivities, by the models introduced in Table 2.1, for seven different MPL structure reported in literature. Comparing the predicted diffusivities with the available data in the literature, a considerable difference is observed. Bruggeman's approximation [49], Neale and Nader relationship [50], and Tomadakis and Sotirchos' formula [52] over predict the data considerably, while Zamel et al.'s model [53] under predict the actual values. The closest model to the published data is Mezedur et al.'s formula [51]. Therefore, this model is implemented in the present investigation to approximate the effective diffusivity of in domain *II*. Note that Mezedur et al.'s model fails to capture the trends of data in some cases, that is why it needs to be modified to be used for MPL.

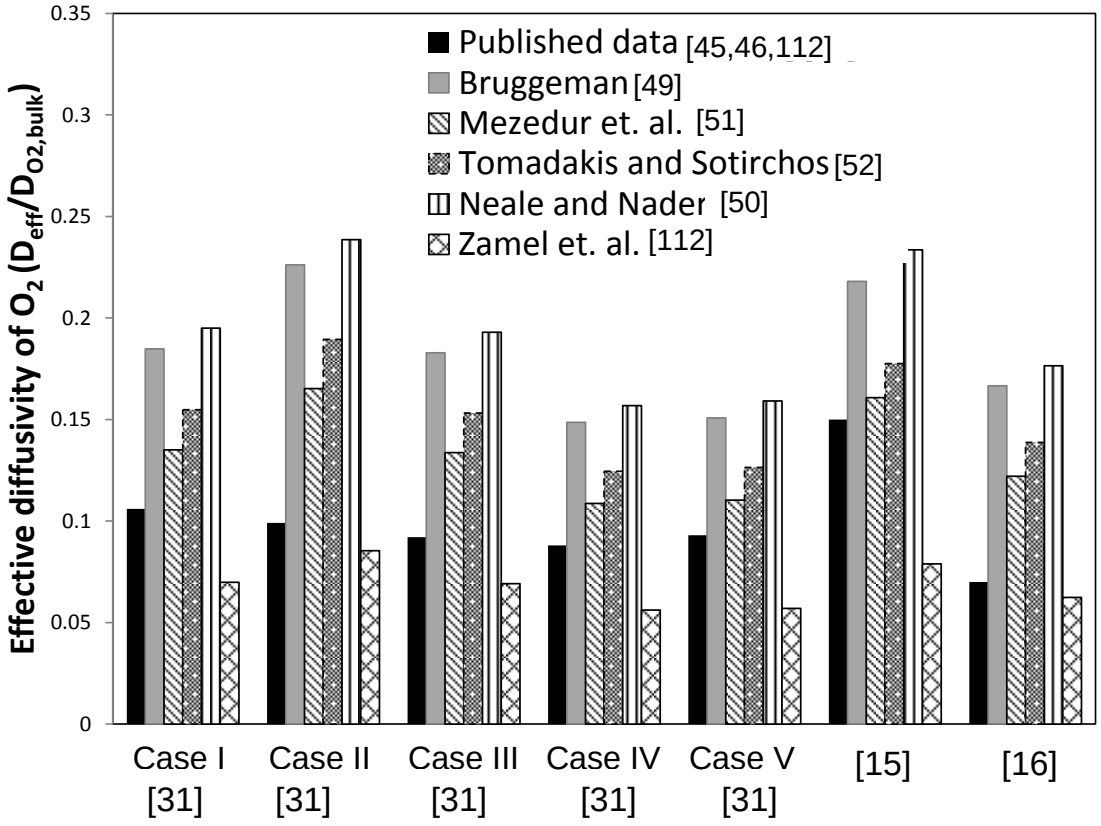

Figure 2.4. Comparison of the available diffusivity models in the literature to published data [45,46,112]**.**

To get D_{II}, Mezedur et al.'s formula is used [51]; however, D is substituted by the modified diffusion coefficient for a pore of diameter d_{II}. The following is the obtained relationship for calculating D_{II}.

$$D_{II}^{i} = \left[1-(1-\varepsilon_{II})^{0.46}\right]\left(\frac{1}{D_b^i}+\frac{3}{d_{II}}\sqrt{\frac{\pi M_i}{8RT}}\right)^{-1} \tag{14}$$

The sequence of calculations to obtain the effective MPL diffusivity is depicted inFigure 2.5.

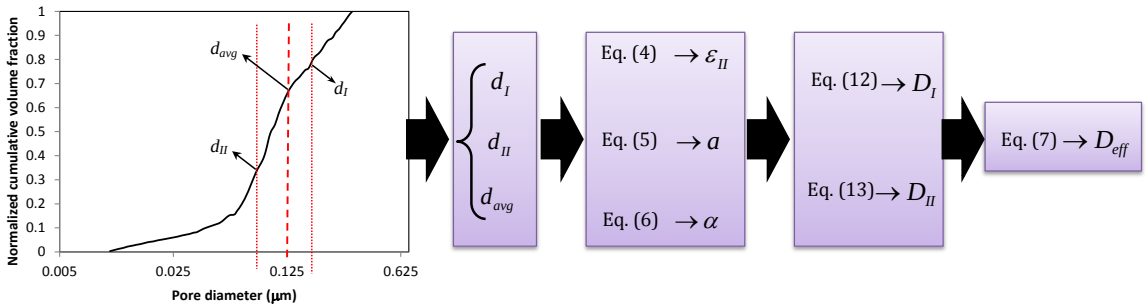

Figure 2.5. Steps for calculating the effective diffusivity using the proposed model.

2.3. Results and Discussion

In this section, first, the results from the present work are compared with the available data in the literature. Then, the effects of MPL pore size and porosity on the effective diffusivity are examined.

2.3.1. Model Validation

There are only a few experimental data points available for the MPL diffusivity in the literature [45,46]. In a research conducted in our team, the MPL diffusivity is obtained by using the FIB/SEM technique [45]. In that work, the relative diffusivity for their considered MPL was obtained 0.15±0.03 for oxygen. The porosity of the MPL was reported as 62%. To use the present model, the values for d_{avg}, d_I and d_{II} needs to calculated from the pore size distribution, *c.f.* Figure 2.3. Following the approach presented in section 2.1, the respective values for d_{avg}, d_I and d_{II} are obtained as 124, 191, and 76 nm. Substituting these values into the present model, *cf.* Figure 2.5, the relative diffusivity is calculated as 0.157 for oxygen, which deviates from the measured data by less than 5%.

Chan et al. [46] also did another measurement on the GDL diffusivity (fibrous substrate and MPL) using a Loschmidt cell. Their reported value for the effective oxygen diffusivity inside the MPL was $1.5\pm0.2\times10^{-6}$ m^2 s^{-1}, which was equal to the relative diffusivity of 0.07±0.01. Their MPL porosity was 64% and the primary and secondary pores extracted from the reported pore size distribution were 204 and 44 nm,

respectively. Inserting these parameters into the present model leads to 0.068 for the relative diffusivity of oxygen, i.e., less than 3% deviation.

In another work, Zamel et al. [112] reported the effective diffusivity for five different MPLs that were constructed through stochastic numerical model. These cases are introduced in Table 2.2. The predicted values for these MPLs by the present model are shown in Fig. 6 and are compared to the published data. The estimated values by Mezedur et. al. [51] approach is also shown in Figure 2.6that reveal this model over-predicts the effective diffusivity for most cases. Specially, for case II, where the pore size distribution has two peaks, because in the present model, the entire structure is modeled with two distinct pores, which would be close to the two peaks in case of MPLs with bimodal pore size distribution. The present model shows a reasonable accuracy with maximum deviation of around 15%.

Table 2.2. Description of the cases investigated in [112] ***.**

Case	Porosity (%)	d_{avg} (nm)	d_{I} (nm)	d_{II} (nm)
I	65	66	87	45
II	65	92	124	36
III	65	65	116	38
IV	65	48	99	30
V	65	49	71	31

* The present pore sizes are extracted from the reported pore size distributions in [112].

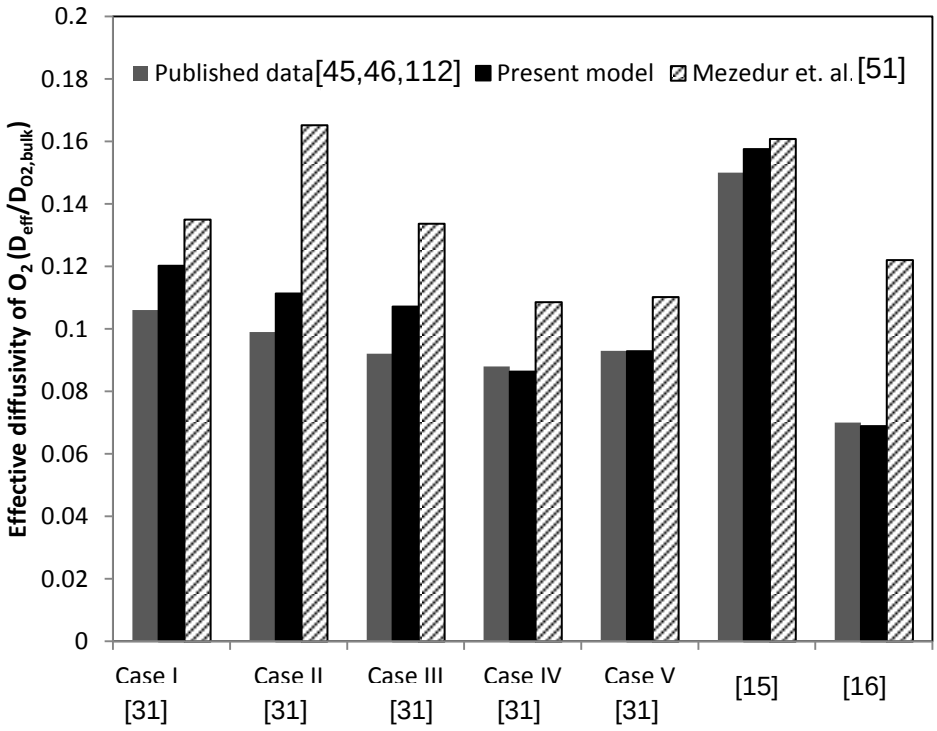

Figure 2.6. Comparison of the model results with other diffusivity values from the literature.

2.3.2. Effect of Liquid Water

In this model, the effect of liquid water inside the MPL is not considered. Because it is expected that the volume fraction of liquid water inside the MPL is low due to the high hydrophobicity of the MPL and its small pore sizes. These two characteristics of the MPL impede liquid water entering to the MPL and push it towards the membrane. Therefore, water is transferred from the MPL to the GDL and cathode flow channels mostly in the form of water vapor. In case of high saturation levels inside the MPL, some modifications to the model should be made, e.g., multiplying a $(1\text{-}s)^m$ term to the results [113], where s is the saturation level. The accurate way of extending the model to predict the diffusivity values, when liquid water is present, is to know the liquid water distribution in the structure and treat the liquid water droplets as solid phase. This means the liquid water blocks the pathways for gas diffusion.

2.3.3. Parametric Study

In this section, a parametric study is performed to investigate the effects of various parameters on the effective diffusivity of MPL, using the proposed model. The input parameters to model are the pore size distribution and MPL porosity. Although manufacturing some of the assumed structures in this section may not be feasible, the parametric study performed here will provide the GDL manufacturers with useful information, especially the trends in diffusivity of MPL as a function of structural parameters.

MPL Pore Size Distribution

The MPL pore size distribution is a controlling parameter in determining its effective diffusivity. The pore sizes in the MPL can be controlled using different pore forming agents and different drying conditions [106]. Furthermore, as discussed in [114] and [115], the MPL porosity and pore size distribution alter with different PTFE contents. In this section, the effective diffusivities for some arbitrarily chosen MPL pore size distributions are obtained. It is tried to cover a wide range of possible pore size distributions. These cases are named based on their corresponding diameters; namely d_{ll}, d_{avg}, and d_{l} values. The porosity of the MPLs is considered 60% for these five cases. Note that although the effect of PTFE content on diffusivity is not included in the present model explicitly, the obtained pore size distribution from mercury intrusion porosimetry, implicitly includes those effects.

Figure 2.7 shows the pore size distributions of the MPLs for which the effective diffusivity values are calculated. To generate these distributions, it is assumed the pores are distributed normally. Hence, the normal probability density function, *c.f.* Eq. (15), is used.

$$f(x) = \frac{\exp\left(-\frac{1}{2}\left(\frac{x-\mu}{\sigma}\right)^2\right)}{\sigma\sqrt{2\pi}} \tag{15}$$

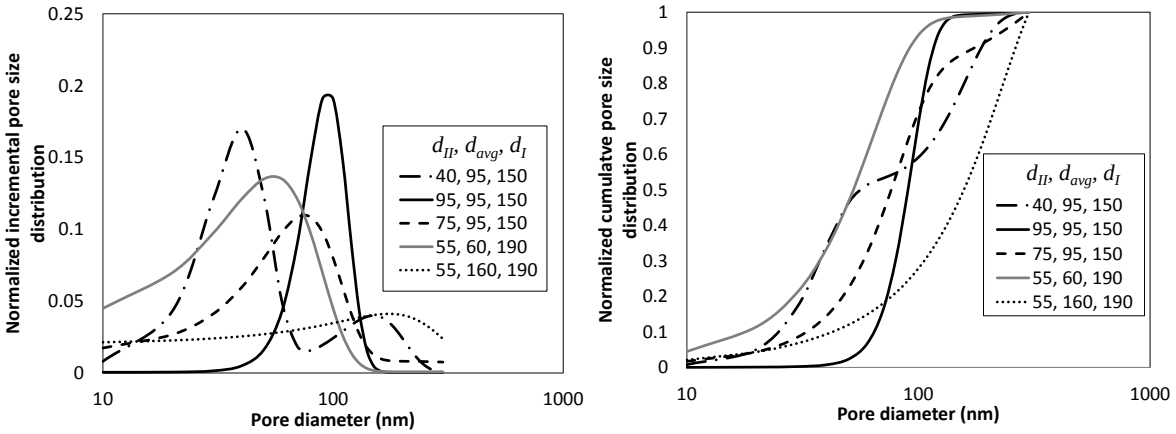

(a) (b)

Figure 2.7. The incremental (a), and the cumulative (b), pore size distributions for the five cases studied in section MPL Pore Size Distribution.

In Eq. (15), μ and σ are the mean and variance of the pore sizes. To find a pore size distribution for a specific MPL with specific values of d_I, d_{II}, and d_{avg}, the normal probability density functions with the mean values of d_I and d_{II} should be first summed up. Then the variance of each distribution should be changed until the mean value of the summation of these two distributions becomes equal to the desired average pore diameter. Note that various pore size distributions might exist for a certain d_I, d_{II}, and d_{avg}.

For the first three cases, the average and primary pore diameters are considered 95 and 150 nm respectively, and the secondary pore diameter is varied. In the last two cases, the average pore diameter is altered. The effective diffusivity of oxygen for each of these cases is plotted in Figure 2.8. Comparing the first three cases, it is observed that by increasing the secondary pore size, the effective diffusivity increases significantly. If the total volume of smaller pores in the pore size distribution of an MPL is large and the peak of the incremental pore size distribution shifts towards the left, a small effective diffusivity should be expected.

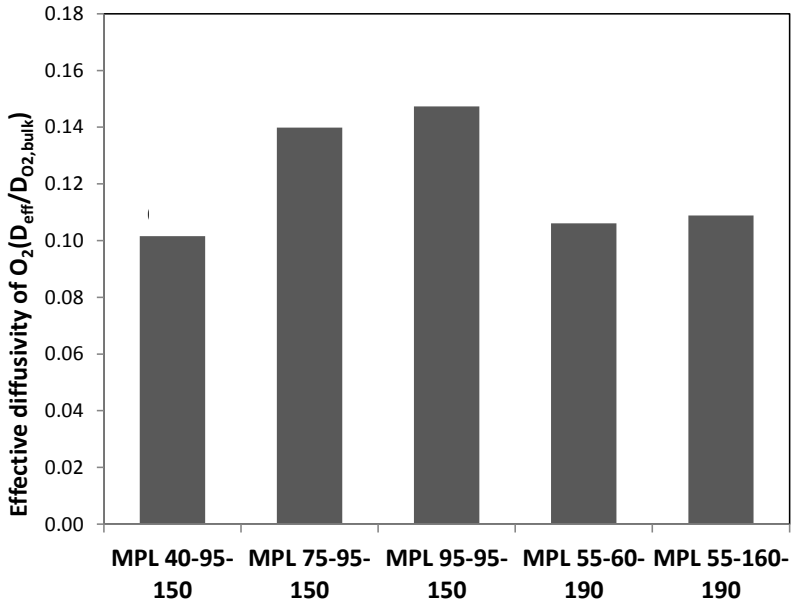

Figure 2.8. Effective diffusivity of the MPLs introduced in Figure 2.7.

For the last two cases where only the average pore size is varied, no considerable change is observed in the calculated effective diffusivity. However, by looking at variations of the effective diffusivity at different average pore size in Figure 2.9, an optimum pore size is found at which the effective diffusivity is a maximum. For the three porosities plotted in Figure 2.9, the optimum value of the average pore size and MPL porosity can be found from the following correlation. Note that this equation is obtained for $55\% < \varepsilon_{MPL} < 65\%$ and may not be applicable to larger/smaller porosity values.

$$d_{avg}^{opt} = 2.166\varepsilon_{MPL} \tag{16}$$

In Eq. (16), the unit for the optimum average pore diameter, d_{avg}^{opt}, is [nm], and the MPL porosity is considered in percent.

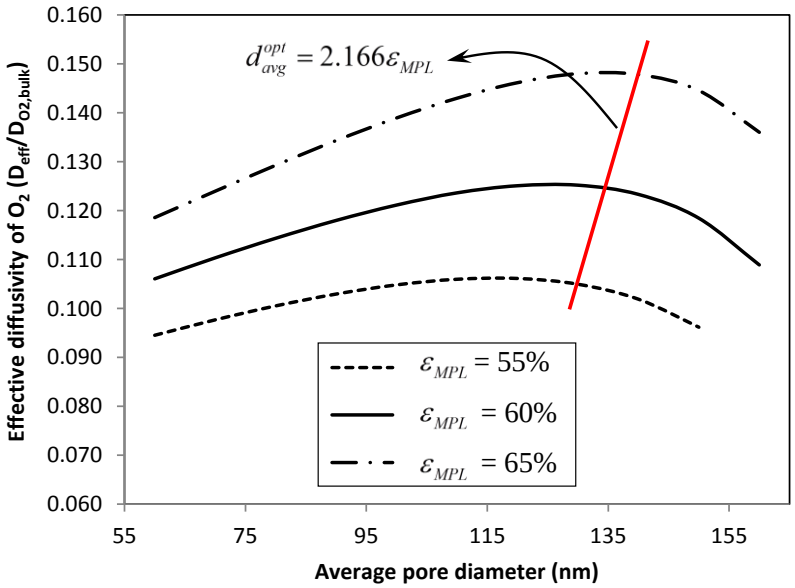

Figure 2.9. Variations of the effective diffusivity at different average pore size.

MPL Porosity

Plotted in Figure 2.10 is the MPL diffusivity as a function of its porosity. Here, the pore size distribution is considered fixed and the MPL porosity is varied between 35% and 65%. There is a 145% increase in the effective diffusivity when the MPL porosity is increased in this range. At lower porosities, mass transfer resistance is higher because the material is denser. So that the pathways for gas transport are narrower. This increases the contribution of Knudsen diffusion in the overall mass transfer process, and consequently reduces the effective diffusivity.

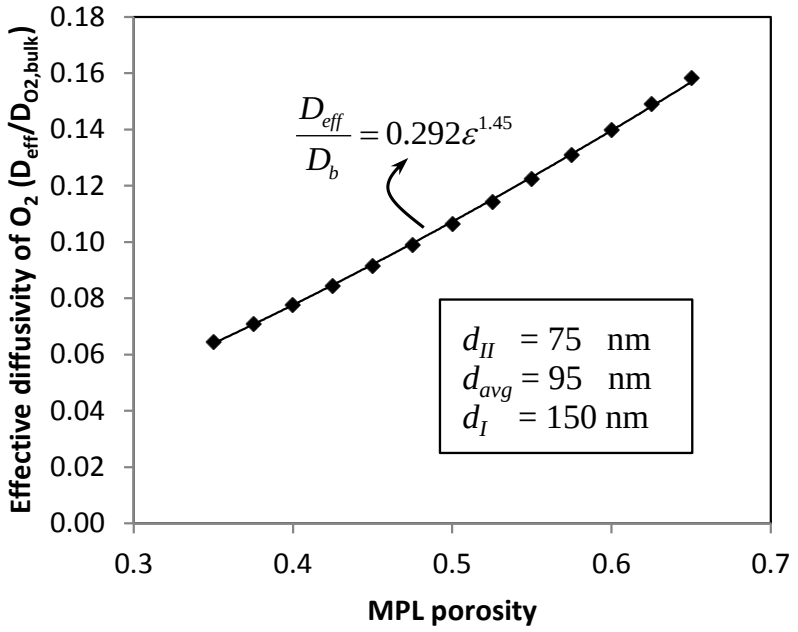

Figure 2.10. Variations of effective oxygen diffusivity by MPL porosity.

For the specified pore size distribution, the data can be fitted by $\frac{D_{eff}}{D_b} = 0.292\varepsilon^{1.45}$, which as an instance, is different from what Bruggeman's model [49] can predict, i.e., $\frac{D_{eff}}{D_b} = \varepsilon^{1.5}$. Here, only the Bruggeman's model is used for comparison, since it is simpler than other models and it is shown previously in other works that it over-predicts the properties [112]. Other models will also fail in predicting the MPL diffusivity for the same reasons explained in section 2.2.

2.4. Conclusions

In this study, a unit cell approach was used to model the effective diffusivity of MPLs analytically. A unique geometrical model was developed as the unit cell for the MPL. The available SEM images of the MPL were used to devise an appropriate unit cell for modeling. The unit cell was consisting of a spherical pore inside a porous cube. The analogy between the heat and mass transfer was utilized to find the effective diffusivity coefficient for the unit cell. The obtained results from the proposed analytical relationship

were compared to the experimental and numerical data available in the literature. Agreement between the present model's results and the available data were promising. The model was then used to find the sensitivity of the effective diffusivity to some of the structural parameters of the MPL. It was found that both the pore size distribution and porosity were influential in determining the effective MPL diffusivity.

In summary, the findings of this research can be listed as the followings:

- A new compact relationship was proposed to predict the effective MPL diffusivity as a function of the pore size distribution and porosity of the MPL.
- Effects of PTFE content on diffusivity was not studied directly, but the changes in pore size distribution and porosity due to addition of PTFE and their effects on diffusivity could be studied using the proposed model.
- Pore size was as influential on the effective diffusivity as the porosity. However, it is not easy to choose one as the main influential property. Since they are both effective on the final diffusivity value to the same extent and effects of both of them should be considered.
- Increasing porosity and the secondary domain pore size, d_{II}, would increase the effective diffusivity.

Chapter 3.

Analytical Model for the MPL Effective Thermal Conductivity

This chapter presents the developed analytical model for the effective MPL thermal conductivity. Similar to the diffusivity model, explained in Chapter 2, the input to this model is the pore size distribution and porosity. The modeling approach is presented in section 3.1, the conducted experiments for validation of the model are described in section 3.2, and the results are discussed in section 3.3.

3.1. Modeling Approach

This work is a continuation of the model presented in Chapter 2. Here we utilize the same unit cell model, which was used for diffusivity modeling, to model the MPL thermal conductivity. Unlike the mass diffusion coefficient estimation that only considers the mass transport through the gas phase domain, for the thermal conductivity estimation, the heat conduction through the solid structure plays an important role. The considered unit cell is the same as before (cf. Figure 2.2). The unit cell consists of a spherical pore (domain I) inside a porous cube (domain II); details on obtaining the geometrical model parameters from the pore size distribution can be found in [116]. The required equation for calculating the effective thermal conductivity for such geometry is [107]:

$$k_{eff} = \frac{3k_{II}k_I\alpha + (2k_{II} + k_I)k_{II}(1-\alpha)}{3k_{II}\alpha + (2k_{II} + k_I)(1-\alpha)} \tag{17}$$

where, k_I and k_{II} are the thermal conductivities for the domains *I* and *II*, *c.f.* Figure 2.2; and α is the ratio of sphere volume to the total cube volume and is calculated from Eq. (18), in which a is the unit cell dimension as shown in Figure 2.2.

$$\alpha = \frac{\pi}{6}\left(\frac{d_I}{a}\right)^3 \tag{18}$$

The spherical pore, domain *I*, only contains stagnant gas, with thermal conductivity k_I. The pores are small (d_I < 300 nm) and bulk thermal conductivity of the gas needs to be modified to include the rarefied gas or Knudsen regime effects. In Knudsen regimes, the gas thermal conductivity is a function of pore diameter in which the gas is stored. Kaganer [117] proposed the following relationship to approximate the gas thermal conductivity as a function of pore size.

$$k_I = \frac{k_{g,0}}{1+2\beta\frac{\lambda}{d_I}} \tag{19}$$

where $k_{g,0}$ is the gas thermal conductivity at standard conditions when Knudsen number is sufficiently small and the regime is continuum. The coefficient β is a parameter that is calculated from the gas accommodation coefficient, α_T, and the specific heat ratio of gas, γ.

$$\beta = \left(\frac{9\gamma-5}{2\gamma+1}\right)\left(\frac{2-\alpha_T}{\alpha_T}\right) \tag{20}$$

There is a complicated relationship for the gas accommodation coefficient [118], but α_T is 0.7-1.0 for common gases at room temperature [119]. For air at 25°C, γ is 1.4, α_T is 0.8, β is ~3 [119] and the mean free path, λ, is 68 nm [120].

Domain *II*, the MPL porous packed bed of spherical carbon nanoparticles, has a thermal conductivity, k_{II}, that can be approximated using the equation of Hsu *et. al.* for a

packed bed of spheres [121], which here, it is modified to include the gas rarefaction effects.

$$k_{II} = \left(1 - \frac{1}{\sqrt{1-\varepsilon_{II}}}\right)\frac{k_{g,0}}{1+6\frac{\lambda}{d_{II}}} + \left(\frac{1-r_s^{\,2}}{\sqrt{1-\varepsilon_{II}}}\right)k_{gs} + \left(\frac{r_s^2}{\sqrt{1-\varepsilon_{II}}}\right)k_s \tag{21}$$

In Eq. (21), the first term is the thermal conductance of the gas stored in domain II pores with diameter d_{II}, the second term is the equivalent conductance of a mixed gas-solid region, and the third term is the conductance of the solid phase. Parameter k_s is the solid phase thermal conductivity (carbon-PTFE), and r_s is the dimensionless contact radius. Here, the effect of PTFE is considered by assuming an effective value for k_s based on the mass fraction of PTFE. This might not be the most accurate approach to include the effect of PTFE on thermal conductivity; however, it is the least complex method. It is shown in [47], that the PTFE content is affecting the MPL thermal conductivity significantly; however, PTFE distribution in the MPL structure can influence the overall MPL thermal conductivity.

$$r_s^{\,2} = 1 - \frac{1}{(1+\omega B)^2} \tag{22}$$

In Eq. (22), B is the particle shape factor and ω is the deformed factor, which dictates the amount of contact area between the particles.

According to the Hertzian theory [122], the radius of the contact area between two identical spheres, η, under compression has the following relationship with the applied force, F.

$$\eta = \left(\frac{3FR}{8E^*}\right)^{1/3} \tag{23}$$

where R is the effective radius, and E^* is the effective modulus of elasticity that can be found from the Poisson's ratio, ν, and the elastic modulus, E, of carbon.

$$\frac{1}{E^*} = 2\frac{1-\nu^2}{E} \tag{24}$$

Figure 3.1 shows a free body diagram of a layer of MPL in which the area of particles in contact with the compression plane is determined from the solid fraction of MPL. Therefore, the amount of force exerted on each particle is $F = \frac{4PR^2}{1-\varepsilon_{MPL}}$. Substituting this in Eq. (23), the final relationship for calculating the contact radius is found as a function of compression pressure.

$$\eta = R\left(\frac{3P}{2(1-\varepsilon_{MPL})E^*}\right)^{1/3} \tag{25}$$

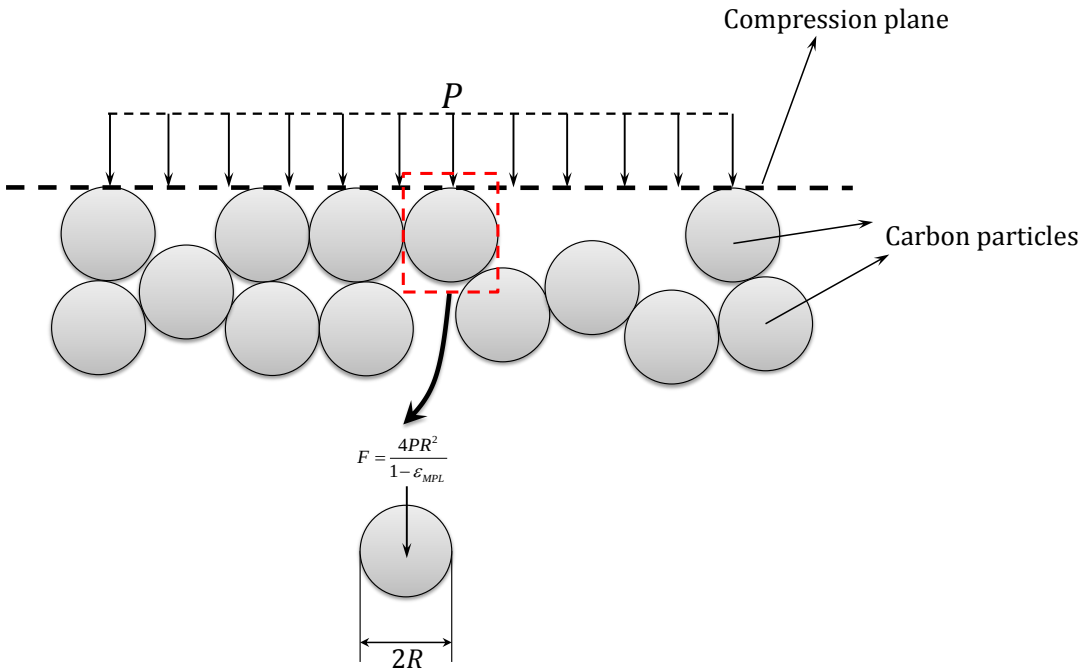

Figure 3.1. Schematic of the carbon particles of the porous MPL under compression.

Equating dimensionless contact radius, *η/R*, to Eq. (22), the equation for the deformed factor, ω is:

$$\omega = \frac{1}{B}\sqrt{\frac{1}{1-\left(\frac{3P}{2(1-\varepsilon_{MPL})E^*}\right)^{2/3}}} - \frac{1}{B} \tag{26}$$

The equivalent conductance of the mixed solid-gas can be calculated from Eq. (27).

$$\frac{k_{gs}}{k_g} = \frac{2}{1-\xi B+(1-\xi)\omega B}\left(\frac{(1-\xi)(1+\omega)B(1+\omega B)^2}{\left[1-\xi B+(1-\xi)\omega B\right]^2}\ln\left(\frac{1+\omega B}{(1+\omega)B\xi}\right) - \frac{B+1+2\omega B}{2} - \frac{(B-1)(1+\omega B)}{1-\xi B+(1-\xi)\omega B}\right) \tag{27}$$

where ξ is the ratio of gas to solid conductivity, and the shape factor, *B*, is calculated as follows [121].

$$B = 1.25\left(\frac{1-\varepsilon_{II}}{\varepsilon_{II}}\right)^{1.11} \tag{28}$$

ε_{II} is the domain *II* porosity, which can be found as a function of the MPL porosity and pore size distribution, using Eq. (29) [116].

$$\varepsilon_{II} = \frac{\left(d_I - d_{avg}\right)\varepsilon_{MPL}}{\left(d_{II} - d_{avg}\right)\varepsilon_{MPL} + d_I - d_{II}} \tag{29}$$

The unit cell size is [116]:

$$a = d_I\left(\frac{\pi}{6\left(1-\frac{1-\varepsilon_{MPL}}{1-\varepsilon_{II}}\right)}\right)^{\frac{1}{3}} \tag{30}$$

To calculate the thermal conductivity of MPL, the porosity and pore size distribution of the MPL are used to generate the geometrical parameters of the model,

i.e., d_I, d_{II}, and d_{avg}, as explained in our previous paper [116]. The sequence of calculations is depicted in Figure 3.2.

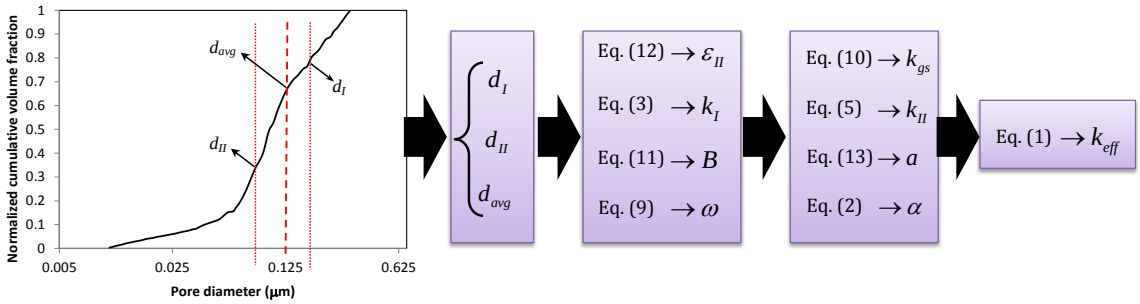

Figure 3.2. Steps to calculate thermal conductivity using the proposed model.

3.2. Experimental Study

3.2.1. Sample Specifications

Measurement of MPL properties is challenging because MPL is not available as a stand-alone layer. In this study, the microporous layer of Sigracet® GDL is selected for measurement and model validation purposes. GDLs 24BA and 34BA have different thicknesses but almost identical structure and porosity. The MPL coated versions of these substrates, SGL 24BC and 34BC, have 45 and 35 μm MPL layers, respectively. Specifications of the samples used in this work are listed in Table 3.1.

Table 3.1. Specifications of Sigracet® samples used in the present study.*

	Porosity (%)	Substrate thickness (μm)	MPL thickness (μm)
SGL 24BA	84	190	-
SGL 24BC	76	235	45
SGL 34BA	83	280	-
SGL 34BC	75	315	35

* Reported by SGL Group with inter-lot intra-lot homogeneity of less than ±10% [123,124].

3.2.2. Thermal Conductivity Measurements

A thermal constants analyser (TPS 2500S, ThermTest Inc., Fredericton, Canada) capable of precise measurement of thermal conductivity, diffusivity and specific heat was used for this study. The instrument has different sensor types and software modules to perform measurements on bulk materials (isotropic and anisotropic), thin films, powders and liquids. This machine uses the transient plane source method and theory in accordance with ISO Standard 22007-2. In this work, a thin film sensor (7280) with a 29.4 mm diameter nickel double spiral insulated in a thin layer of Kapton is used for both transient heating of the sample and precise temperature measurements.

For thin film measurements, a pair of identical samples are placed on either side of the sensor and compressed between two smooth stainless steel blocks. After 20 minutes for temperature equilibration, measurements are performed on each sample at different compression pressures between 1-6 bars. The sample-sensor assembly and the corresponding equivalent thermal resistance network including the contact resistances between the sample and sensor and the sample and steel are shown in Figure 3.3. The power from the heat source, $\dot{Q}$, the temperature rise between the sensor and steel block, ΔT, the sensor area, *A*, and the sample thickness, t_{sample}, are used to calculate the apparent sample thermal conductivity.

$$k_{sample} = \frac{\dot{Q}}{A}\frac{\Delta T}{t_{sample}} \tag{31}$$

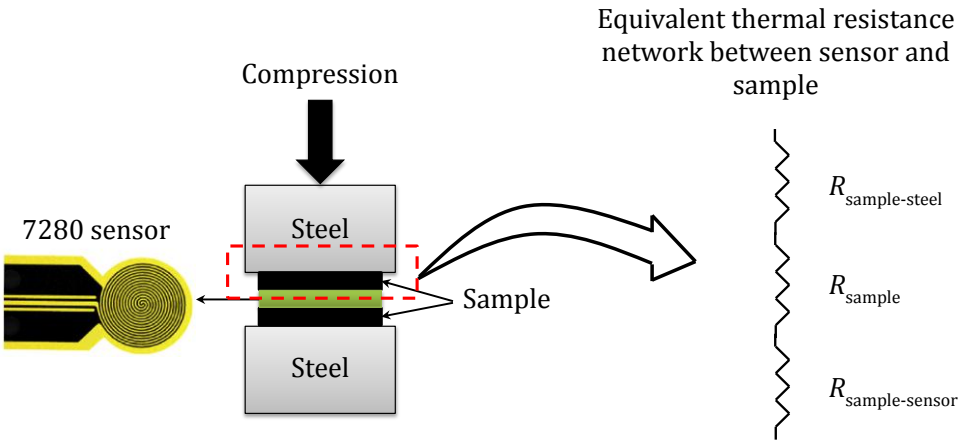

Figure 3.3. Schematic of the sample arrangement in TPS 2500S and the equivalent thermal resistance network.

Contact resistances are included in this measured apparent thermal conductivity and can be significant, especially for porous, rough or rigid thin materials with air gaps between the sensor and sample. Therefore, for accurate values for the thermal conductivity it is needed to remove those effects.

3.2.3. Removing the Contact Resistance Effects

To determine the k_{eff}, the total resistance, $R_{tot} = \frac{t_{sample}}{k_{tot}}$, is calculated, in which k_{tot} is the uncorrected value of the thermal conductivity which is reported by the TPS software. The corrected thermal conductivity value, k_{eff}, should be found after removing the contact resistance effects following the two thickness method [1].

$$R_{tot} = R_{sample} + R_c, \qquad R_{sample} = \frac{t_{sample}}{k_{eff}} \tag{32}$$

By measuring the resistance for two different thicknesses of the same material, it is possible to calculate k_{eff} and R_c, the two unknowns in two measurements.

$$k_{eff} = \frac{t_{sample,2} - t_{sample,1}}{R_{tot,2} - R_{tot,1}}, \quad R_c = R_{tot,1} - \frac{t_{sample,1}}{k_{eff}} \tag{33}$$

For each GDL type, five pairs of 4×4 cm^2 samples were prepared. The thermal conductivity of each pair of samples was measured three times with a rest interval of ten minutes between measurements.

3.2.4. Thickness Measurements

The thickness of GDLs under compression load was measured by a custom-made tool at Ballard Power Systems. GDL samples of each type were prepared with a circular punch (24.5 mm). Thickness measurements with accuracy of ±1 μm were made with loads from 1 to 6 bar. The MPL thickness is calculated by subtracting the thickness of the BC type GDL from the corresponding BA type GDL.

3.3. Results

Thermal resistance network for a GDL sample that has MPL includes the MPL resistance, the substrate resistance, and the contact resistance between these two layers. Subtracting the total resistances for two GDLs that has MPLs with different thicknesses, result in omitting that interfacial resistance, by assuming the interfacial resistances are identical due to the similarities in microstructures. Therefore, the MPL thermal conductivity can be calculated from the following equation.

$$k_{MPL} = \frac{t_{MPL,24BC} - t_{MPL,34BC}}{(R_{34BC,tot} - R_{34BC,sub}) - (R_{24BC,tot} - R_{24BC,sub})}$$
$$R_{24BC,sub} = \frac{t_{24BC,sub}}{k_{sub}}, \qquad R_{34BC,sub} = \frac{t_{34BC,sub}}{k_{sub}} \tag{34}$$

In Eq. (34), $t_{MPL,24BC}$ and $t_{MPL,34BC}$ are the MPL thicknesses for the 24BC and 34BC GDLs; $R_{24BC,tot}$ and $R_{34BC,tot}$ are the total resistances of SGL 24BC and 34BC; and $R_{24BC,sub}$ and $R_{34BC,sub}$ are the thermal resistances of the substrate for the SGL 24BC and 34BC.

3.3.1. GDL Thicknesses and Total Resistances

The changes in the GDL thickness under compression for various GDL types are plotted in Figure 3.4(a). Note that the overall GDL thickness reduces up to 5% with the applied compression.

Figure 3.4 (b) presents the total measured resistances for the four GDL types at various compression pressures. The uncertainty of the total resistance measurements, including the standard deviation of the apparent thermal conductivity measurements, was less than 2% for all sample types. The error bars are less than the height of the markers used for data in the plot. These resistances include the contact resistances, which their effects should be removed to obtain the effective thermal conductivities. As mentioned in section 3.2.1, thermal conductivity of SGL 24BA and 34BA are identical; and its corresponding value can be calculated from Eq. (33).

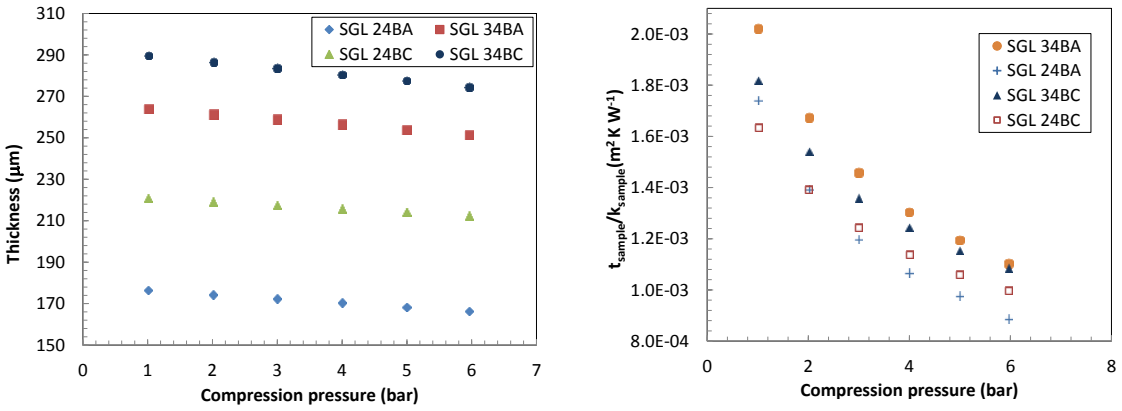

(a) (b)

Figure 3.4. (a) Variations of thickness under compression for different GDL types; and (b) total thermal resistance calculated from the raw data from TPS 2500S.

3.3.2. Effective Thermal Conductivity of MPL

Figure 3.5 shows the effective MPL thermal conductivity obtained from Eq. (34). The measured values for the substrate thermal conductivity are consistent with the reported values for the same GDL, i.e., SGL 24BA, in [1]. However, there is a discrepancy between the obtained MPL thermal conductivity values in this work and tests conducted by our colleagues using a different apparatus [1]. The average uncertainty of measurements is less than 8% for the GDL substrate and is less than 18% for MPL.

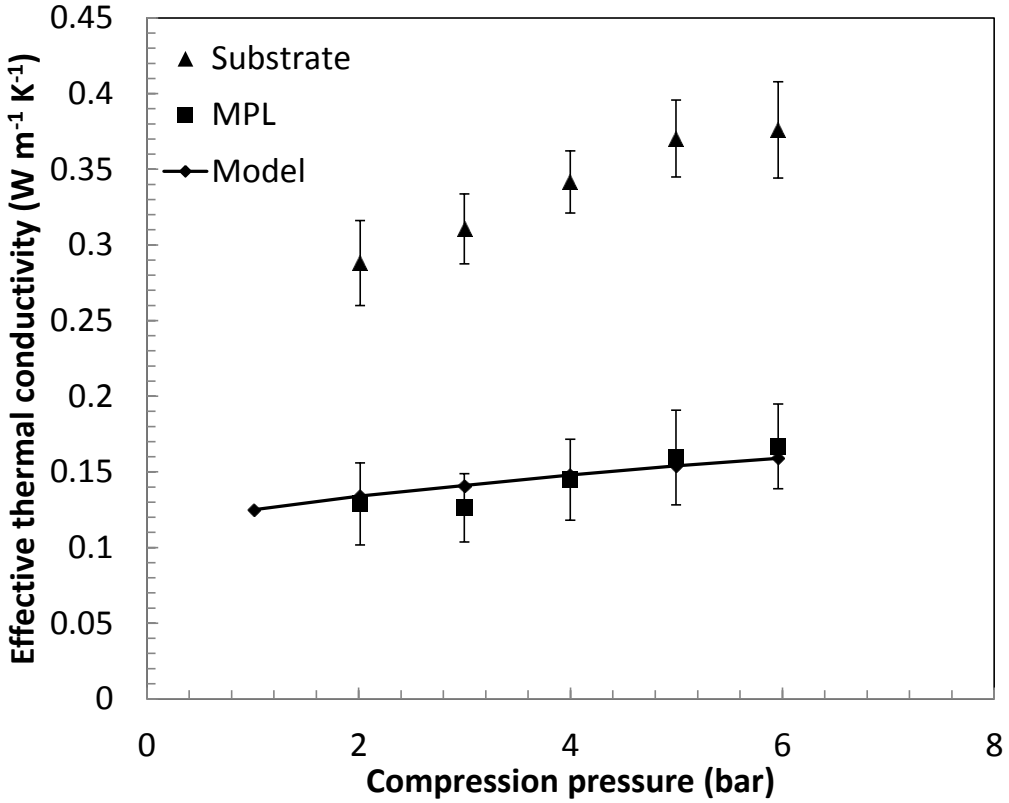

Figure 3.5. The measured thermal conductivity of the substrate (▲) and MPL (■), and the MPL thermal conductivity predicted by the present analytical model (line).

The MPL model results are plotted in Figure 3.5. The model predicts the thermal conductivity values as a function of pressure with a good accuracy within the uncertainty of the measurements. While the substrate shows a stronger dependence on compression, a slight functionality of pressure is observed for MPL. The same slope of the thickness-compression curve for samples with and without MPL shows that the

majority of the thickness changes occur in the substrate, *c.f.* Figure 3.4(a). Hence, one may conclude that due to the slight changes in the str ucture of MPL up to 6 bar, there is no significant alteration of thermal conductivity. However, this statement is not valid for the substrate that exhibited a sizable deformation under compression, and therefore a steeper thermal conductivity-pressure curve.

3.3.3. Compact Relationship Development

The analytical model was used to generate over 200 values for MPL thermal conductivity as a function of d_I, d_{II}, d_{avg}, and porosity. For the generated points, the range of pore size varied between 80-150 nm for d_I, d_{II}, d_{avg}, and porosity was kept between 0.4-0.6. A compact relationship between thermal conductivity and these parameters was developed that provides an estimation of the MPL thermal conductivity with less than 10% deviation from the predicted value by Eq. (17).

If all parameters are substituted in Eq. (17), it can be seen that $\frac{d_I - d_{avg}}{d_{avg} - d_{II}}$ is a suitable candidate for selection as a dimensionless characteristic pore size. Hence, it is chosen as one of the independent variables of the correlation. Denoting this parameter by d^*, the effective thermal conductivity would be only a function of d^*, ε_{MPL}, and compression pressure, i.e., $k_{eff} = f(d^*, \varepsilon_{MPL}, P)$. LAB Fit software [125] is used to find the best fit on the data out of 572 equations. The best fit to the data is shown in Eq. (35).

$$k_{eff} = \left(3\times10^{-7} P + 0.90\right)\left(-10.76\,\varepsilon_{MPL}^{-1+0.003/d^*} + \frac{10.77}{\varepsilon_{MPL}}\right) \tag{35}$$

The variations of thermal conductivity versus porosity for several d^* values at 1 bar compression are shown in Figure 3.6. The thermal conductivity is higher for lower porosities, i.e., materials with higher solid fraction and fewer air gaps. Therefore, the overall thermal conductivity is higher for low porosity MPLs, which is desirable; however, it is shown in our previous investigation [116] that mass diffusion coefficient decreases

as the porosity decreases. Hence, there should be optimal conditions, where both mass diffusivity and thermal conductivity are high. In section 3.3.4, specifications for an optimal MPL structure are proposed to get the maximum thermal conductivity and diffusivity.

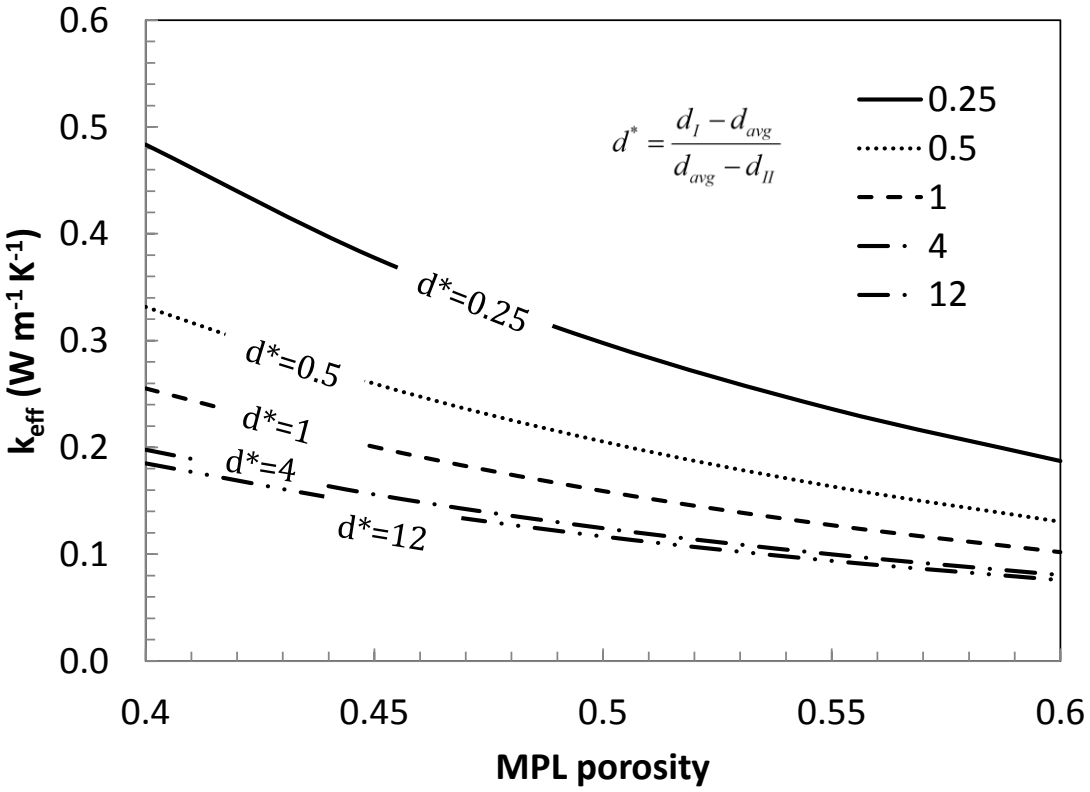

Figure 3.6. Variations of thermal conductivity at various d* and porosity values.

3.3.4. Optimal MPL Structure for Enhanced Heat and Mass Transfer

Better performance of fuel cells will not be achieved unless their components are designed optimally. In this section, a multi objective genetic algorithm ("gamultiobj" in MATLAB [35]) is used to find the optimal structural specifications of the MPL for the maximized effective thermal conductivity and diffusivity. The objective functions for the genetic algorithm are Eq. (35) and the relationship for diffusivity in [116]. The design variables are $\{d_I,\ d_{II},\ d_{avg},\ \varepsilon_{MPL}\}$ and the lower and upper bounds for these variables are set as {100 nm, 40 nm, 90 nm, 0.45} and {200 nm, 80 nm, 150 nm, 0.65},

respectively. The genetic algorithm parameters, e.g., mutation and cross over, are left at their default values.

Figure 3.7 presents the effective diffusivity and thermal conductivity at optimal design points. Each of the points in this figure corresponds to local maximum values for the diffusivity and thermal conductivity. Based on an arbitrary criterion chosen by the authors (k_{eff}>0.2 and D>0.1), the yellow shaded area in Figure 3.7 shows the high diffusivity region, and the blue shaded area shows the high thermal conductivity region. The corresponding limiting current density for D>0.1 is calculated to be higher than 1.4 A cm^{-2} by assuming purely gas diffusion inside the MEA by using Eq. (36). In Eq. (36) D_{eff} represents the effective diffusivity of the entire cathode electrode (entire GDL and catalyst layer), and C_∞ is the oxygen concentration in the cathode channel. The temperature gradient at this current density can also be obtained from 1D heat conduction assumption. At 1.4 A cm^{-2} the obtained temperature drop along the MPL thickness is 2.3 K for the MPL effective thermal conductivity of 0.2 W m^{-1} K^{-1} and 4.6 K for 0.1 W m^{-1} K^{-1}. To have less temperature gradient, it is preferred to choose the thermal conductivities higher than 0.2 for the optimal MPL conditions. The green area presents the region where both diffusivity and thermal conductivity are high. Therefore, the only design point within this region is selected as the optimal design point. The specifications of this design point, which is the optimal MPL structural properties, are listed in Table 2.

$$i_L = nFD_{eff}\frac{C_\infty}{\delta} \tag{36}$$

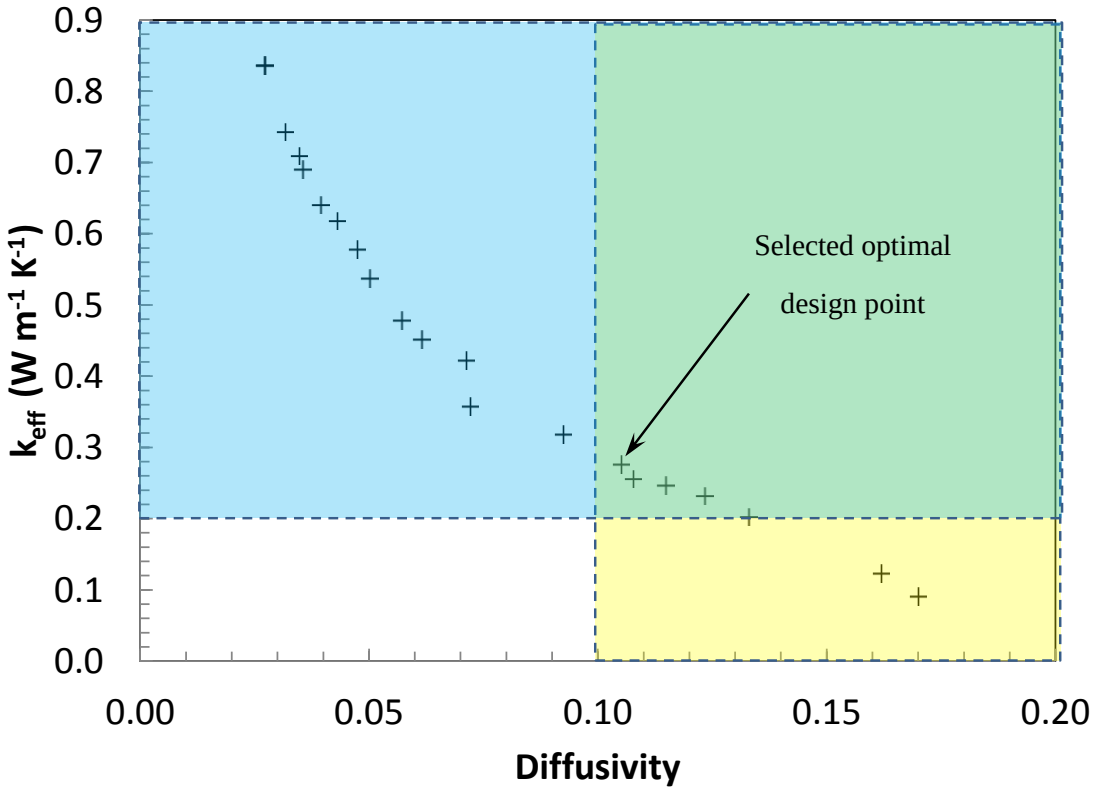

Figure 3.7. Effective diffusivity and thermal conductivity at optimal design points.

Table 3.2. Specifications of an optimal MPL design.

d_I (nm)	d_{II} (nm)	d_{avg} (nm)	ε_{MPL} (%)	k_{eff} ($Wm^{-1}K^{-1}$)	$D_{eff} = \frac{D}{D^0_{O_2}}$
128	71	122	63	0.28	0.11

This data reveals that the MPL structure should have large pores in between dense agglomerates of carbon; the large pores acts as the mass transport pathways, while the dense agglomerates provides the heat transfer pathways.

3.4. Conclusions

In the present study, a new analytical model was developed to estimate the effective thermal conductivity of MPL as a function of pore size distribution, porosity, and compression pressure. A series of experiments were performed to obtain the MPL thermal conductivity at various pressures. The changes in the thickness of the GDLs due to compression were also measured. The effects of the contact resistances between the samples and the sensor in the apparatus were removed using four GDL types. The measured thermal conductivity values for the MPL under 1-6 bar compression fell between 0.13-0.17 W m^{-1} K^{-1} with less than 18% measurement uncertainty. The observed changes in thermal conductivity due to compression were more pronounced in the substrate and only a slight increase in the MPL thermal conductivity was observed as a result of compression.

The model results were validated against experimental data and a compact correlation was proposed based on more than 200 thermal conductivity values generated by the analytical model. The obtained correlation for the MPL thermal conductivity and the diffusivity were used in a multi objective function to suggest an optimal MPL structure.

The following highlights the findings of this work:

- A new analytical relationship was developed for the MPL thermal conductivity as a function of pore size distribution, porosity, and compression pressure.
- MPL thermal conductivity was measured using transient plane source technique at various compression pressures, where effects of contact resistance on the TPS data were removed.
- A compact relationship was proposed to estimate the MPL thermal conductivity.
- A multi objective genetic algorithm was used to find an optimal MPL structure that operate optimally for mass and heat transfer.

Chapter 4.

Three-Dimensional Phase Segregation of MPLs by Nano-Scale X-Ray Computed Tomography

The overall objective of this chapter is to develop an accurate technique for three-dimensional, non-destructive, phase segregated visualization of MPLs used in fuel cells. Sample preparation techniques as well as image acquisition systems are described in section 4.1, and the obtained results are presented in section 4.2.

4.1. Experimental

4.1.1. Sample Preparation

Commercially available GDL samples from SGL Group (SIGRACET® GDL 24BC) of 235 μm thickness were used in this work. The 24BC material represents a typical GDL configuration with a PTFE treated non-woven carbon paper substrate coated with a carbon nanoparticle and PTFE based MPL. Two different sample preparation methods were evaluated for NXCT imaging, which requires small sample sizes for high-resolution scans. In the first technique, a 350 μm diameter circular GDL sample was manually punched from the larger sheet with a sample corer (Fine Science Tools; part#18035), while the second technique utilized an FEI Helios NanoLab 650 SEM/FIB system to extract a ~20 μm cubic MPL sample from the GDL sheet using a microscope assisted focused ion beam (FIB) lift-out approach. Each sample was fixed on the tip of a stainless steel needle which was then positioned in the NXCT sample holder for imaging. The cylindrical GDL sample was attached to the needle tip with the MPL facing upward while the FIB sample was secured on the needle tip using amorphous platinum.

For the FIB sample, we preferred to use cubic sample compared to cylindrical due to the higher possibility of destroying the samples by FIB in cylindrical preparation approach. In a cubical sample, it is only required to trim the edges of the sample four times; however, to make the sample cylindrical it should be exposed to FIB for a longer time during the trimming stage, which is very likely to destroy the sample.

4.1.2. Image Acquisition

X-ray tomography of low density materials such as carbon and PTFE benefits from the use of low energy X-rays as a key requirement to enable visualization of multiple solid phases in composite materials. Additionally, nanostructured materials such as MPLs require high resolution. A ZEISS Xradia 810 Ultra NXCT scanner was therefore chosen for this analysis, as it offers the lowest X-ray beam energy and highest resolution currently available with commercial systems. As shown in Figure 4.1, this system generates a monochromatic X-ray beam of 5.4 keV impinging on the sample which rotates up to 180° in user defined steps. Two resolution modes are available to the user: the large field of view (LFOV) mode spanning 65 μm at a resolution of 150 nm and the high resolution (HRES) mode spanning 16 μm at a resolution of 50 nm. In this work, the HRES mode was utilized to capture the nanoscale geometry of the MPL.

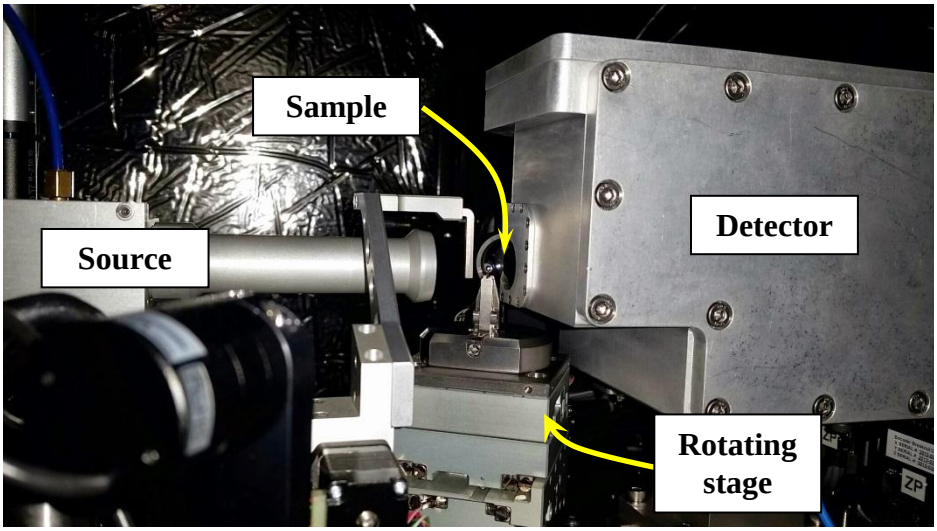

Figure 4.1. Arrangement of X-ray source, detector, and sample in the ZEISS Xradia 810 Ultra

The intensity of mono-energetic X-ray photons passing through a medium follows the Beer-Lambert law, Eq. (37), where I_0 and I are the X-ray intensities at the entrance and exit of the medium, respectively, μ is the linear attenuation coefficient, and t is the sample thickness in the beam direction. Additionally, the linear attenuation coefficient is a material specific property that is a function of density and effective atomic number. Therefore, when one considers obtaining an X-ray micrograph with adequate contrast, the sample density, effective atomic number, and thickness should be considered as important factors [126].

$$I = I_0 \exp(-\mu t) \tag{37}$$

In XCT systems, the exponent in Eq. (37) is calculated based on the detected intensity by the X-ray detector at every pixel within the field of view, and a gray level is assigned to each pixel to construct an X-ray micrograph. The resultant 2D micrographs obtained with different projections are then combined using complex and computationally intensive image processing algorithms to reconstruct the 3D structure of the scanned material.

The optimum image acquisition conditions for the punched and FIB prepared MPL samples in regards to preparation time and image quality are listed in Table 4.1. The exposure time was selected based on the number of counts, which is a measurable quantity that represents the amount of X-ray intensity acquired by the detector. Here, a number of counts of at least 2,000 was required to obtain good quality images. The corresponding exposure times for the punched and FIB prepared samples were 130 and 90 seconds per image, respectively. Notably, the longer exposure time required for the punched sample is due to its larger size and increased attenuation of the X-ray beam at each projection (*cf*., Eq. (37)). The number of projections for each scan was set to 901, i.e., an image was captured at each 0.2° during the full 180° sample rotation. Since the voxel size is 16 nm, 901 projections is sufficient to have angular sample displacements smaller than the pixel size, which satisfies the Nyquist criterion. Our region of interest was a 6 μm cube that was located at the center of our sample. Therefore, 0.2° angular rotation would be equal to ~10nm displacement which is less than 16 nm.

Table 4.1. NXCT system imaging conditions for the punched and FIB prepared MPL samples.

Specification	Punch	FIB
Sample preparation time (hr)	0.5	4*
Maximum sample size (μm)	350	20
Exposure time to reach 2,000 counts (sec)	130	90
Number of projections	901	901
Scan time (hr)	32.5	22.5
Total time (sample preparation + scan time)	33	26.5

*Time required by an expert technician.

By inspection of Table 4.1, the total processing time of the punched sample is longer than that of the FIB prepared sample. This is mainly due to the longer exposure time per projection for the punched sample as a consequence of its larger thickness; however, it should be noted that the FIB lift-out technique also requires an expert technician and specialized facilities only available in select locations. Punching the sample is more convenient and less costly. Table 4.2 summarizes the advantages and disadvantages associated with each of the two sample preparation techniques in the context of NXCT imaging of MPL materials.

Table 4.2. Comparison of the punch and FIB lift-out sample preparation techniques for NXCT scanning of MPL materials.

	Punch	FIB
Advantages	Convenient	Short scan time
	Minimal user training	Minimizes or eliminates 3D reconstruction artifacts
	Short preparation time	
	Low cost	Allows separation of MPL from substrate
Disadvantages	Long scan time	Long preparation time
	Perimeter deformation	Specialized facility
	Reduced X-ray transmission due to wide sample	User training
	Possible 3D reconstruction artifacts	High cost
	Possible interference from substrate	Needs conductive Pt layer to manipulate sample
		Ion beam damage on milled edges

4.2. Results and Discussion

4.2.1. Segmentation Analysis

Two tomographic data sets were measured using the HRES scanning mode of the NXCT system from the punched and FIB prepared MPL samples. The raw images were reconstructed in 3D and processed using the histogram equalization filter in Avizo® to enhance the contrast. Figure 4.2 shows two representative 2D slices from the 3D reconstructed images. The diameter of the circular image domain in Figure 4.2 is 16 μm with a pixel size of 16 nm. The black and white portions of the gray scale represent the pore phase (filled with air) and solid phase, respectively. The obtained image quality and resulting MPL structure appear to be comparable with the two sample preparation techniques, given the longer exposure time used for the punched sample.

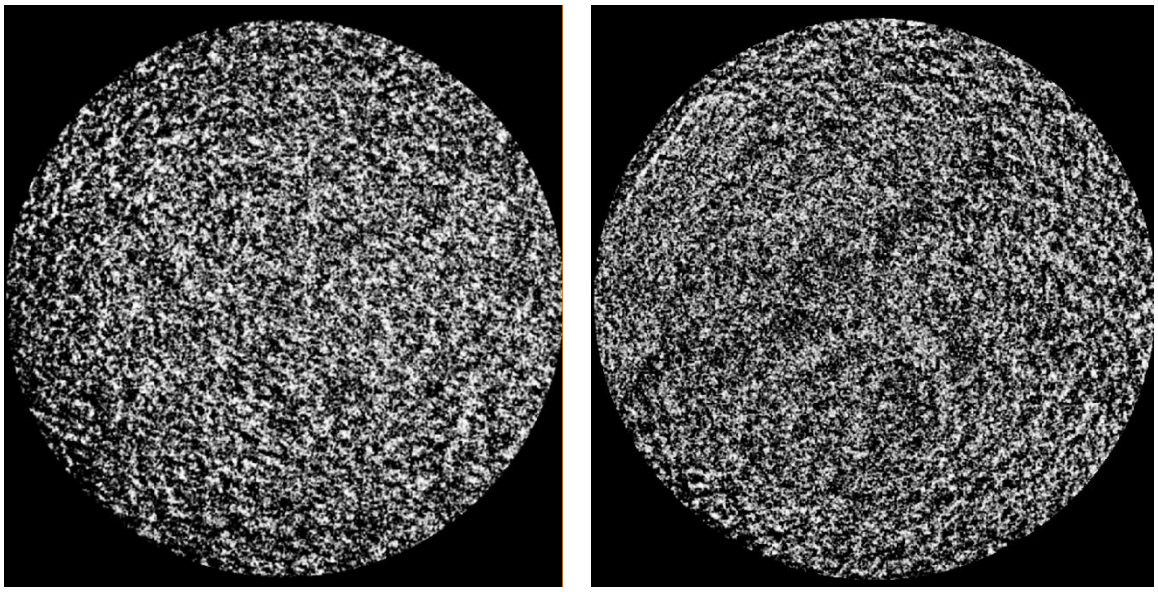

(a) (b)

Figure 4.2. Images of reconstructed 2D slices of the (a) punched and (b) FIB prepared MPL samples obtained in HRES mode with 16 nm pixel size and 16 μm field of view.

In the image segmentation process, determining the threshold value for the solid phase is the most important step in order to ultimately obtain the correct material structure. The importance of the threshold value and its effect on the reconstructed structure has been studied previously [127]; however, no systematic analysis of various auto-thresholding techniques has been reported. An automated method is generally preferred that does not require previously known information about the porosity of the material. Several algorithms are available for segmentation of images based on global or local histogram-derived thresholding methods. In the global methods, thresholding is performed on the calculated histogram for the entire image, while in the local methods the threshold is computed locally based on the histogram within a window of radius *r* around each point. In this work, due to the uniformity of the obtained images, the global auto-thresholding algorithms available in ImageJ [128] were applied to the obtained reconstructed 2D images for both samples. A comparison was then made between the threshold values and sample porosities resulting from each of these methods.

The image histogram for the stack of 2D images from the NXCT scan of the FIB prepared MPL sample is shown in Figure 4.3(a). The calculated threshold and porosity values obtained with the selected auto-thresholding algorithms are presented in Figure 4.3 (b). Since the acquired images are 16-bit, the images have 2^{16} or 65,536 gray scale levels (in contrast to 8-bit images that have merely 256 levels). The highest threshold value was calculated by the MaxEntropy approach while the lowest value was obtained from the Isodata method. Out of the eleven algorithms evaluated here, the three entropy-based algorithms (i.e., MaxEntropy, RenyiEntropy, and Yen) appear to over-predict the threshold value and the respective calculated porosity value, considering that typical MPL porosities generally range from 50% to 65% [45,70]. In contrast, the average porosity value calculated from the non-entropy-based methods was 50% with 2% standard deviation, which is more reasonable. The segmented structure obtained for the solid (mixed carbon and PTFE) and pore (air) phases of the MPL with a porosity of 50% $\pm$ 2% is presented in Figure 4.4. The resulting nanostructure of the MPL material reveals connected particles and pores in both solid and pore phases with typical feature sizes on the order of ~100 nm.

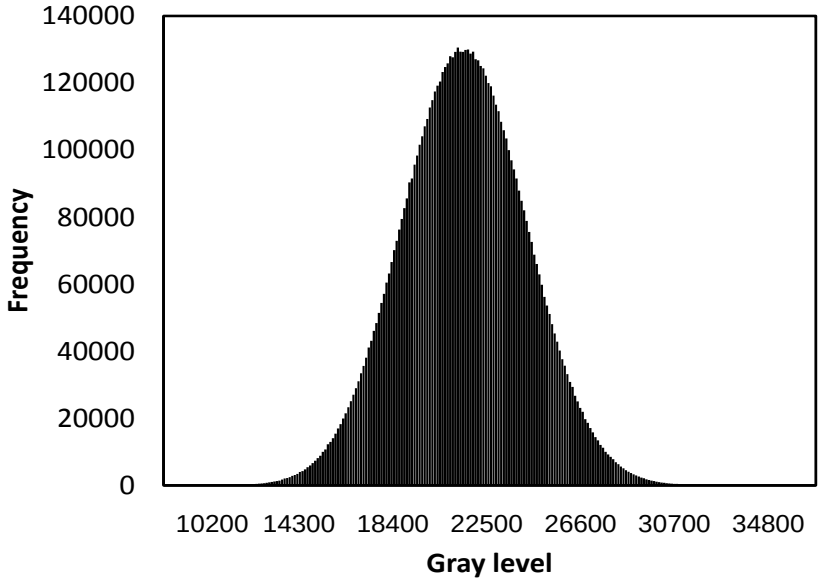

(a)

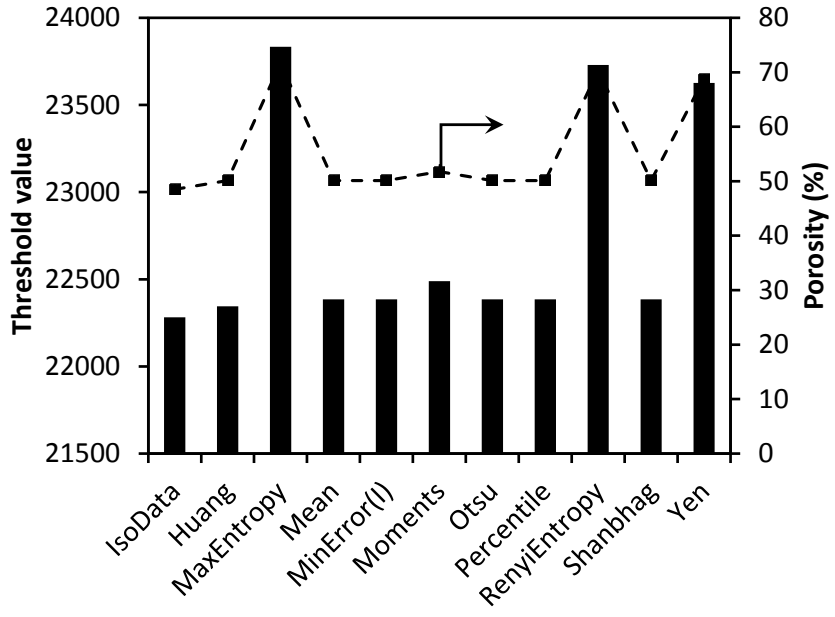

(b)

Figure 4.3. (a) Gray scale histogram for the stack of 2D images from the FIB prepared MPL sample and (b) bar chart of threshold values with corresponding porosity values calculated by eleven different auto-thresholding algorithms.

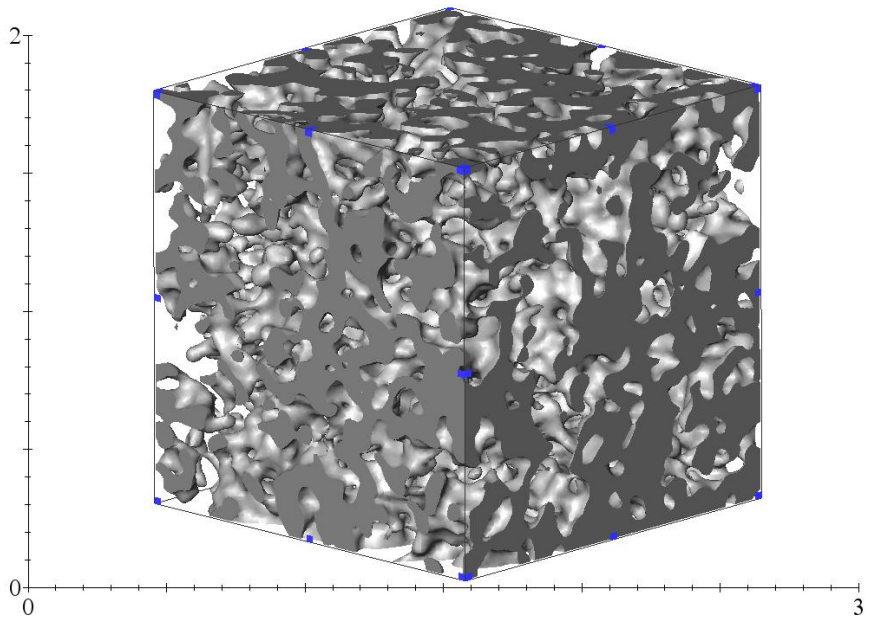

Figure 4.4. 3D segmented structure of the solid and pore phases of the MPL. The cube dimension is 1.5 μm and the voxel size is 16 nm.

4.2.2. Carbon and PTFE Distributions

The next goal of the present NXCT analysis is to segregate the internal carbon and PTFE phases that exist within the solid phase of the MPL material, which has not been previously accomplished with any characterization method. In section 4.1.2 it was shown that the gray scale of each pixel in a 2D X-ray micrograph is proportional to the X-ray intensity measured by the detector, which in turn is dependent on three sample characteristics: thickness, density, and effective atomic number. Imaging and discerning the component structure of the MPL should take into account all these effects. The MPL X-ray absorption effect due to the thickness can firstly be minimized by utilizing the FIB lift-out sample preparation method described above. The carbon and PTFE phases of the MPL have similar densities of 2,250 and 2,200 kg m^{-3}, respectively. The effective atomic numbers and mass attenuation coefficients, however, differ and may be used as a method to distinguish between carbon and PTFE.

The effective atomic number for chemical compounds can be found from Eq. (38) , in which α is the fractional number of electrons of the i^{th} element and m is a constant

that is suggested to be 4.1 for materials with $Z_{eff} > 6$.[31] Using Eq. (38), the effective atomic number of PTFE, with chemical formula of $(C_2F_4)_n$, was found to be 8.26, which is 38% higher than pure carbon with Z_{eff} of 6. This leads to a higher mass attenuation coefficient for PTFE compared to carbon.

$$Z_{eff} = \left(\sum_i \alpha_i Z_i^{m-1} \right)^{1/(m-1)} \tag{38}$$

A graph of the mass attenuation coefficients for carbon and PTFE at X-ray beam energies between 4-10 keV is given in Figure 4.5 [129]. Notably, the difference in the mass attenuation coefficients of carbon and PTFE decreases with increasing beam energy. The reason for this is that the higher energy X-ray photons are not scattered as easily as the lower energy X-ray photons from the lighter elemental atoms. This implies that one should use as high a contrast level as possible between carbon and PTFE to be able to distinguish between them; thus, lower energies. The presently employed ZEISS Xradia 810 Ultra NXCT scanner operates at 5.4 keV and from Figure 4.5 it is estimated that the difference between the carbon (1.54 m^2 kg^{-1}) and PTFE (4.43 m^2 kg^{-1}) mass attenuation coefficients is 2.89 m^2 kg^{-1}. To date, the ZEISS Xradia 810 Ultra has the lowest lab-scale X-ray beam energy, thus it provides the best contrast possible. In comparison, a system using a beam energy of 8.0 keV [70] cannot discriminate the carbon and PTFE as easily. That is, according to Figure 4.5, the difference in the mass attenuation coefficients at 8 keV for carbon (0.5 m^2 kg^{-1}) and PTFE (1.4 m^2 kg^{-1}) is 0.9 m^2 kg^{-1}. Hence, the difference at 5.4 keV is about 3x larger than the difference at 8 keV, making the visualization and discrimination of carbon and PTFE in the MPL more plausible. It should also be noted that, as light materials, carbon and PTFE are almost transparent to X-rays since their attenuation coefficients are orders of magnitude lower than high atomic number materials such as metals.

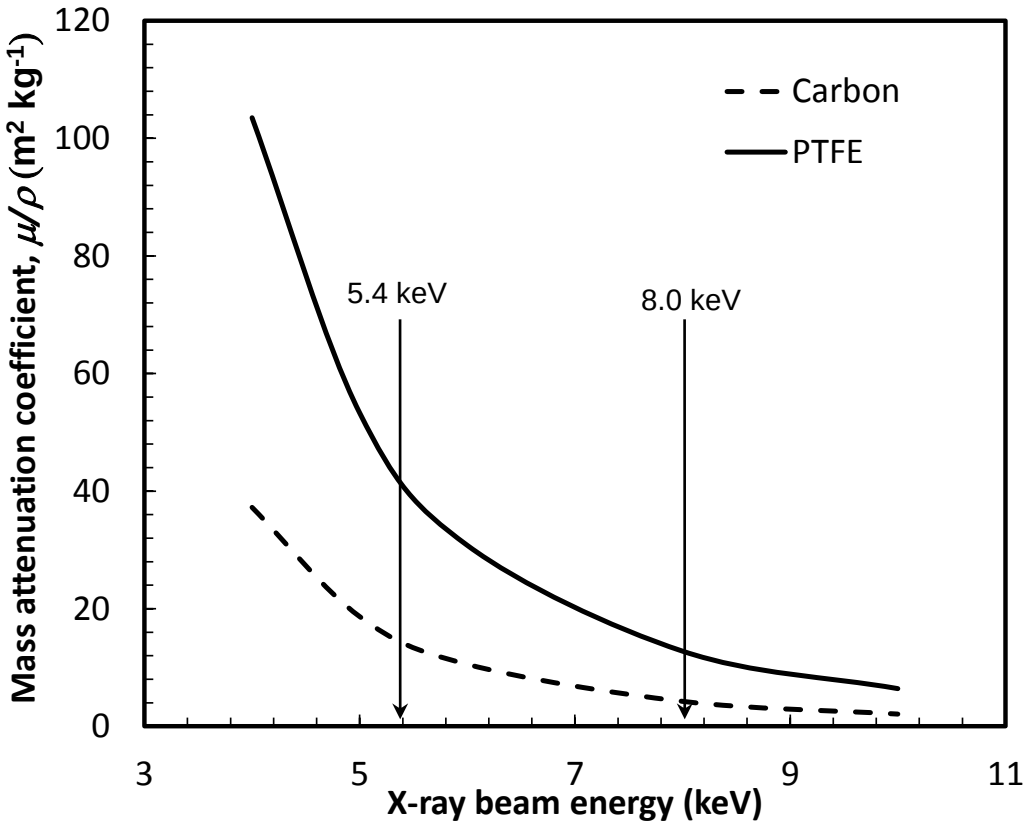

Figure 4.5. Mass attenuation coefficients for carbon and PTFE at different X-ray beam energies [129]**. The vertical guidelines indicate the mass attenuation coefficients for carbon and PTFE at 5.4 and 8.0 keV.**

During an acquisition of a tomographic data set with fixed voxel size, the product of density and mass attenuation coefficient, represented by μ, is the only parameter that governs the detected intensity and hence the gray scale value of each pixel. At 5.4 keV, μ_{PTFE} is 97.4, μ_C is 34.7, and μ_{air} is 4×10^{-2} cm^{-1}, which implies that the brightest region in the image corresponds to PTFE, while the darkest region is air (void space) and mid-range gray levels correspond to carbon. There is a linear relationship between the effective material attenuation coefficient and the assigned gray scale, although the absolute correspondence is software/machine dependent. Eq. (39) can be derived for a material composed of two different solid phases such as an MPL composed of carbon and PTFE, where G_i and μ_i are the gray scale level and attenuation coefficient of the i^{th} phase, respectively, μ_{bg} is the attenuation coefficient of the background (i.e., air in the

present case), and G_{bg} is the background gray scale level that varies depending on the conditions of the scan.

$$\frac{G_1 - G_{bg}}{G_2 - G_{bg}} = \frac{\mu_1 - \mu_{bg}}{\mu_2 - \mu_{bg}} \tag{39}$$

For an MPL with carbon and PTFE as the first and second phases in background air, the right hand side of Eq. (39) is equal to 0.35. This means that PTFE voxels are ~3x brighter than carbon voxels. To use this approach, it is important to capture X-ray transmission though background air within the field of view, such that G_{bg} can be found by averaging the gray scale level in that region.

Figure 4.6(a) shows a raw X-ray image captured in the LFOV mode (150 nm resolution) of the cubic MPL sample prepared by FIB lift-out and mounted on the tip of a needle; while Figure 4.6(b) shows a 2D reconstructed slice of the MPL sample measured in HRES mode (50 nm resolution) with air in the top right corner of the field of view. Selection of this region of interest was made by LFOV mosaic imaging of a 325 μm survey area from which a suitable 16 μm domain comprising of both MPL and background air was identified for subsequent HRES scanning. The subdomain used for reconstruction was then selected a sufficient distance away from the MPL cube surface (~2 μm) in order to avoid sample regions with potential ion beam damage from FIB milling.

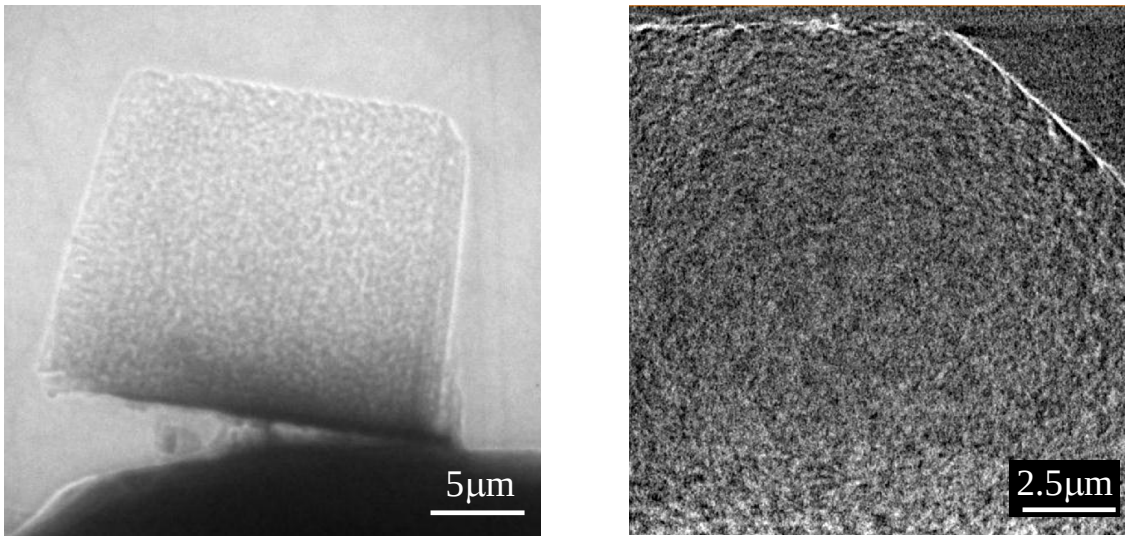

(a) (b)

Figure 4.6. (a) Raw LFOV X-ray image of the cubic MPL sampled prepared by FIB lift-out; and (b) a 2D reconstructed slice of a section of the same sample measured in HRES mode.

Discrimination of MPL component phases was initiated by identifying the air and removing the void space within the data set. The contributions of the carbon and PTFE portions can then be separated. The air contained in the top right corner of Figure 4.6 (b) was used to calculate G_{bg}. The average gray scale value, G_{bg}, for this region is 20,690, which was subsequently used to differentiate between the solid (mixed carbon-PTFE region) and void (pores) by using the auto-thresholding techniques introduced in section 4.2.1. Separation of the carbon and PTFE phases was then accomplished by auto-thresholding for carbon and assigning the gray scale value (G_{carbon}) in Eq. (39) to solve for the PTFE gray scale. Thus, G_{carbon} was found to be 22,365 from the auto-thresholding technique and G_{PTFE} was calculated as 25,480 from Eq. (39) for the present MPL sample. Note that G_{bg} is the average gray scale value of air, while G_{carbon} and G_{PTFE} are threshold values for separation of phases. The volume fraction of PTFE was found to be 11% and is equivalent to a 22% weight fraction, which compares favorably with the reported value for PTFE concentration in SIGRACET® MPLs of 23% by weight [130,131]. This approach has thus allowed the carbon and PTFE distributions in the MPL to be revealed, even without prior knowledge of the material composition.

A representative reconstructed cross-section of the obtained 3D distribution of carbon, PTFE, and combined carbon-PTFE phases are shown in Figure 4.7(a) to (c), respectively. It is discovered that the carbon particles are interconnected and the isolated PTFE domains are distributed randomly within the carbon domain and bind to the carbon particles. Moreover, in the regions indicated by the arrows in Figure 4.7(c), some of the PTFE domains have a surface portion exposed to the pore space, which likely contributes to a desirable hydrophobic material characteristic that supports gas phase transport in the pore phase. In contrast to the general notion that PTFE is coated on carbon in the form of a thin film, it is observed here that the PTFE forms isolated islands of relatively large size that are located near the center of the solid phase domains. It can thus be concluded that PTFE preferentially fills small pores located within the carbon phase rather than creating a coating on the outside of the carbon particles. Furthermore, this finding suggests that the overall pore-solid configuration in the MPL is primarily controlled by carbon particle interactions. These features can similarly be observed in the 3D reconstructed image in Figure 4.7(d).

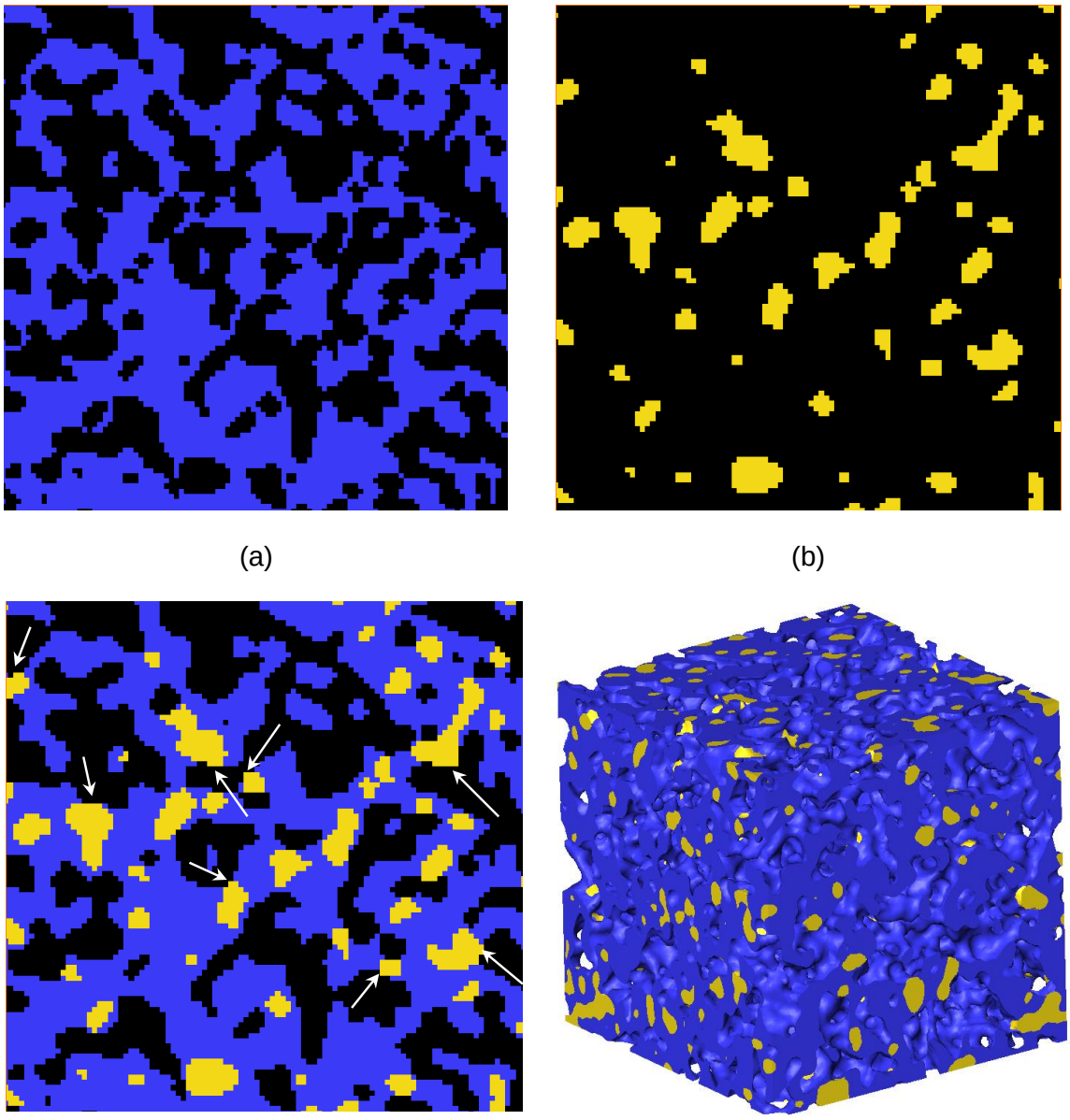

Figure 4.7. **Phase differentiated MPL structure: (a) carbon distribution; (b) PTFE distribution; (c) combined pore, carbon, and PTFE distributions; and (d) 3D structure. Carbon is shown in blue, PTFE in yellow, and pore phase in black. The cube dimension is 1.5 μm and the voxel size is 16 nm.**

It should be noted that the present approach is sensitive to noise levels in the images; thus, for samples prepared by FIB lift-out, where image noise is minimized, this approach yields a reasonable PTFE distribution. Thicker samples such as those prepared by the punch method, where noise levels are higher due to X-ray attenuation outside of the field of view, can yield the PTFE threshold value and hence the distribution based on the known value of PTFE content (mass or volume fraction), but are less amenable to strictly image based segregation and compositional analysis. In this study, only one type of MPL was used to demonstrate the technique, and the overall approach would benefit from further validation with other MPL materials of known composition, which is subject to future work.

4.2.3. MPL Properties

Knowledge of the full 3D structure of the MPL material enables calculation of its properties as an MEA component, which is valuable for MPL and GDL design, MEA integration, water management analysis, and fuel cell performance simulation. In this study, both structural and transport properties are evaluated for the first time on a fully phase segregated MPL structure. A comprehensive, custom-developed numerical framework for simulation of the effective properties of MPL and GDL materials was previously developed and validated by our group.[8,25,35] This numerical framework has so far been used to generate virtual 3D MPL and GDL substrate structures using stochastic methods and calculate their corresponding effective properties. Here, a portion of the same numerical framework was utilized to calculate the MPL properties for the 3D reconstructed structure obtained from NXCT.

The calculated pore size distribution for the presently analyzed SGL 24BC MPL is shown in Figure 4.8. The present methodology enables identification of pore sizes (diameters) as small as ~30 nm, as the simulation algorithm requires a minimum of two adjacent voxels to define a pore diameter. The volumetric average pore size was found to be 90 nm with the majority of pores in the 60-130 nm range, which is within the specified 50 nm resolution of the NXCT instrument. The pore size distribution was determined to be highly uniform in this range, as the present MPL sample contained no pores larger than 200 nm. Furthermore, the pore volume associated with small pores in

the ~30-60 nm range appears to be relatively insignificant, and it is therefore anticipated that potential pores below the present resolution limit would also be rather insignificant. The nanoscale pores in the MPL, compared to the microscale pores in the GDL substrate, is the reason for the apparently hydrophobic nature of the MPL due to the increase in capillary pressure in smaller pores ($P_{cap} \sim 1/d_{pore}$). The other calculated MPL properties are listed in Table 4.3. The relative gas diffusivities of the porous MPL (relative to bulk diffusion) were found to be ~0.10, which accounts for Knudsen effects and therefore has a unique value for each gas. The calculations of electrical and thermal conductivity of the MPL yielded 580 S m^{-1} and 0.60 W m^{-1} K^{-1}, respectively. The results for these effective transport properties, which are primarily controlled by the solid phase structure, are expected to benefit from the knowledge of the individual carbon and PTFE distributions within the material. For comparison, if the entire solid phase is assumed to be carbon, the corresponding properties would be 770 S m^{-1} and 0.80 W m^{-1} K^{-1}, which overestimates the phase resolved conductivity values by more than 30%.

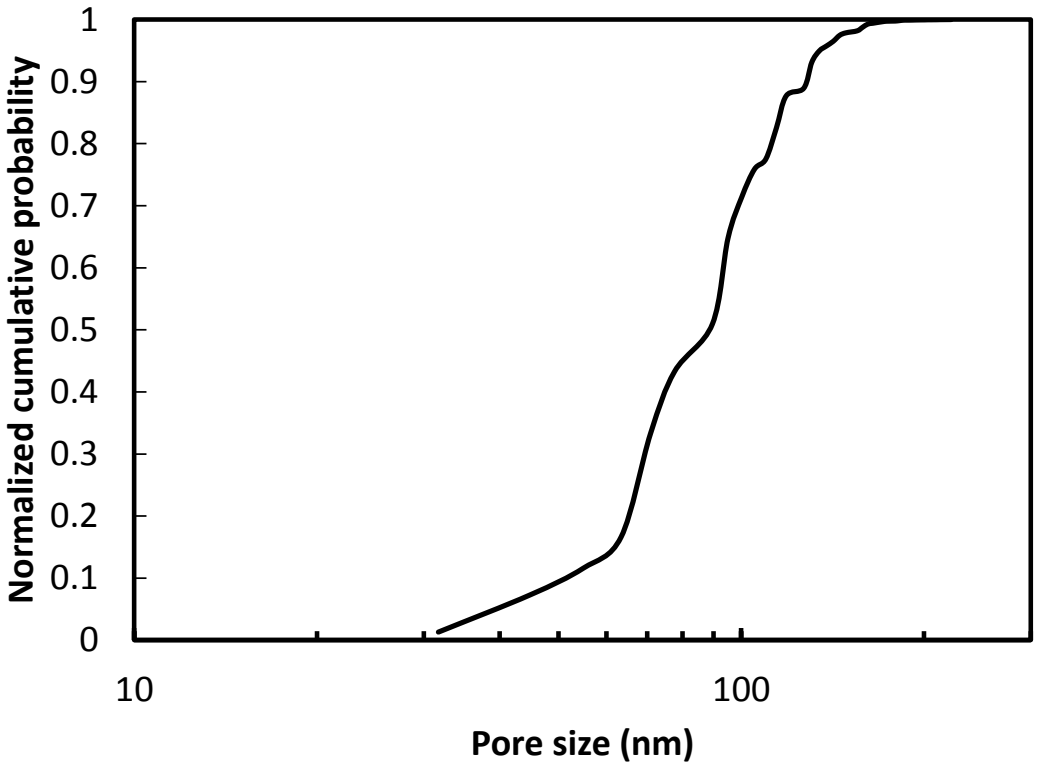

Figure 4.8. Cumulative pore size distribution of the SGL 24BC MPL calculated numerically based on the 3D reconstructed structure obtained from NXCT.

Table 4.3. MPL properties for the SGL 24BC GDL calculated numerically based on the 3D reconstructed structure obtained from NXCT.

Property	Value
Porosity (%)	50
PTFE content (wt.%)	22
Average pore size (nm)	90
Oxygen diffusivity ($m^2\ s^{-1}$)	1.6×10^{-6}
Relative diffusivity ($D_{eff,O2}/D_{O2,b}$)	0.09
Water vapor diffusivity ($m^2\ s^{-1}$)	1.9×10^{-6}
Relative diffusivity ($D_{eff,H2O}/D_{H2O,b}$)	0.11
Thermal conductivity ($W\ m^{-1}\ K^{-1}$)*	0.60
Electrical conductivity ($S\ m^{-1}$)**	580

*The thermal conductivities used for carbon and PTFE are 150 [88] and 0.25 $W\ m^{-1}\ K^{-1}$ [132].
**The electrical conductivities used for carbon and PTFE are 147,000 and 0 $S\ m^{-1}$ [88].

4.3. Conclusions

Nano-scale X-ray computed tomography was used in this work to determine the 3D nanostructure of a standard MPL used in the membrane electrode assembly of polymer electrolyte fuel cells. Complete phase segregation of pore, carbon, and PTFE phases within the MPL material was uniquely enabled by the present low X-ray energy NXCT method and associated image processing techniques, even without prior knowledge of the material composition. Carbon nanoparticles were shown to form an interconnected backbone of the solid phase of the MPL that provides a continuous pathway for solid phase transport, i.e., electrical and thermal conduction. The PTFE phase was found to form small, isolated island domains within the porous carbon phase rather than the previously anticipated film coating of the particles. However, the PTFE still acted as a binder and structural support of the carbon nanoparticles and had surfaces exposed to the pore phase that are expected to facilitate the desired hydrophobicity of the internal pores of the MPL.

Sample preparation by microscopic FIB lift-out and manual punching methods was compared in terms of sample preparation time and convenience for obtaining similar X-ray intensities. Compared to the simple punching method, the FIB lift-out technique provided higher image quality with less noise and more contrast, but carries substantially

higher cost and requires a specialized facility. Therefore, even with a low energy X-ray beam (5.4 keV), a fairly small sample size (ideally <20 μm) is required for assessing different solid phases in a porous material, which was validated in this work by accurate quantification of the PTFE content of the SGL 24BC MPL.

An in-house developed numerical framework was utilized to quantify the structural and transport properties of the MPL material. The porosity and average pore size were found to be 50% and 90 nm. The diffusive transport properties of the pore phase were quantified by the effective diffusivity of oxygen and water vapor, while the solid phase transport properties were quantified by the calculated effective electrical and thermal conductivities. The accuracy of these simulated properties benefit particularly from the new knowledge of the segregated phase distributions discovered in this work.

Looking ahead, the present NXCT based characterization method could become invaluable for MPL design and analysis in order to develop higher performing fuel cells, for example by advanced water management strategies. A similar approach could also be employed to determine nanoscale phase distributions in other composite and porous materials (e.g., catalyst layers) of relevance for a wide range of electrochemical energy conversion and storage systems for clean energy applications.

Chapter 5.

Evidence for MPL Degradation Under Accelerated Stress Test Conditions

In this work, the cathode MPL of a highly corroded MEA is analyzed using NXCT. Samples for this study are obtained from a cathode corrosion accelerated stress test, in which the MEA is subjected to voltage cycling at high temperature and relative humidity. The goal is to compare the structure and properties of GDL at the BOL and degraded states. Explained in section 5.1 are the experimental steps taken for this study. The changes in the structure as well as the changes in diffusivity, thermal conductivity, and hydrophobicity/surface roughness are also discussed in section 5.2. The reported diffusivity and thermal conductivity in this chapter are based on the developed analytical models in Chapter 2 and Chapter 3.

5.1. Experimental

Scanning a GDL with a wide range of pore size, nano-pores in the MPL to micro-pores in the substrate, requires two instruments with different resolution. In this work, ZEISS Xradia 520 Versa with achievable resolution of 0.7 μm is chosen for scanning of the substrate. This system has a polychromatic X-ray source with variable power and accelerating voltage. To scan the MPL, the higher resolution ZEISS Xradia 810 Ultra is used. Unlike the Versa, the Ultra has a monochromatic X-ray source of 5.4 keV, which is low enough to provide a good contrast for even low density materials. The arrangement of source and detector in these two instruments are different. In the Versa, position of source and detector, as well as the objective lenses, can be changed according to the required resolution and the size of the region of interest. However, in the Ultra the

source and detector positions are fixed and there are only two modes of imaging: *i*) large field of view (LFOV) with 150 nm resolution, 64 nm voxel size, and 60 μm field of view; and *ii*) high resolution (HRES) with 50 nm resolution, 16 nm voxel size, and 16 μm field of view. Here, the Versa imaging conditions for scanning the GDL substrate was 0.6 μm voxel size in 600 μm field of view; and the Ultra was in the HRES mode for the MPL scanning with the above-mentioned conditions.

5.1.1. Samples Specifications

One of the main possible mechanisms for MPL degradation is corrosion of carbon nanoparticles. Accelerated cathode catalyst layer corrosion test is devised for simulation of cathode carbon support degradation in a rapid and harsh condition. These conditions may lead to degradation of MPL, because similar to the catalyst layer, MPL is also composed of carbon nano-particles. Therefore, the degraded samples in this work were taken out from the MEAs that had been under harsh accelerated cathode corrosion test. In this work, the degraded sample is called the EOL sample and the fresh sample is called the BOL sample. The EOL sample was subjected to more than 4000 voltage cycles (high and low voltages) in fully humidified conditions at 80 °C to generate cathode corrosion.

SEM Samples

Thickness of the MPL can be captured by using either NXCT or SEM imaging. Both methods should yield similar results. However, here, since the MPL scans were performed in HRES mode, the FOV was smaller than the total thickness of the MPL. Therefore, to measure the thickness in a larger portion of the MPL and to have more data points, SEM images from the cross section of the GDL were acquired. Samples were prepared by casting MEAs in epoxy pucks, which were polished in a Struers TegraPol-11 polisher with 120–1200 grit silicon carbide paper, and then carbon coated with an Edwards Scancoat Six Sputter Coater.

XCT Samples

Generally, to reduce noise in the acquired images, the samples for X-ray scanning systems should be smaller than their field of view. Specially, for the HRES mode of the Ultra system with 50 nm resolution, the samples have to be smaller than 16 μm to guarantee the best image quality. For micro-scale scanning of the GDL substrate using the Versa system, the samples were prepared simply by cutting a triangle with ~3 mm base and ~1 cm height, where the region of interest for scanning was chosen somewhere close to the tip of the triangle, *cf*. Figure 5.1(a). The samples for the nano-scale imaging of MPL using the Ultra system were prepared by cutting a cube with dimensions less than ~15 μm, using the focused ion beam (FIB) assisted lift-out approach, and placing the cube on tip of a stainless steel needle at SFU 4D LABS , *cf*. Figure 5.1(b).

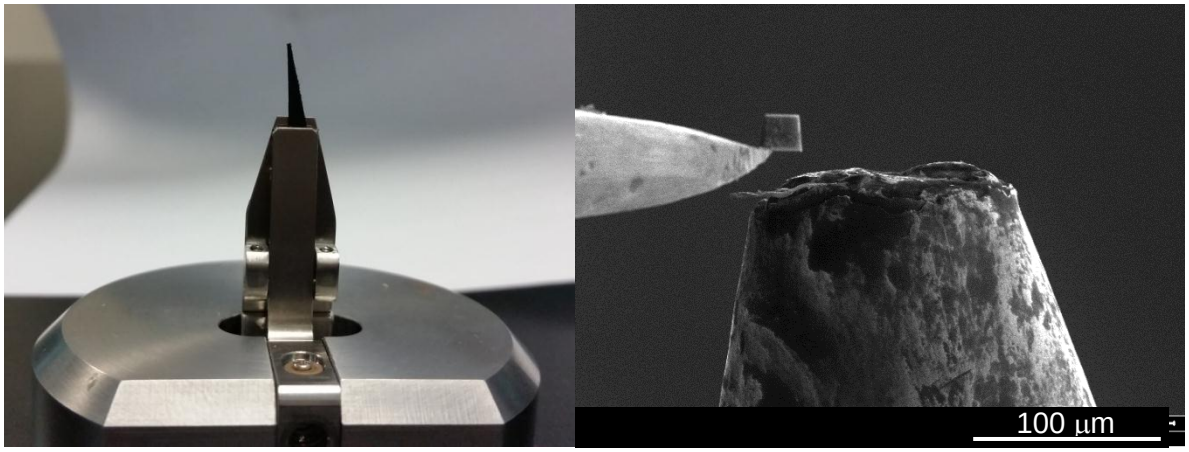

(a) (b)

Figure 5.1. (a) The prepared sample for the Versa system, mounted on a sample holder; (b) SEM image from one stage of sample preparation for the Ultra system. Notice the significant difference in the sample size for the two instruments.

5.2. Results and Discussion

5.2.1. MPL Thickness Changes

SEM images are used to measure the MPL thickness at several spots by ImageJ software. 142 spots were selected randomly for assessment. Distribution of normalized MPL thickness is plotted in Figure 5.2(a) for the BOL and EOL samples. Significant difference is observed between the mean values of the two populations (thicknesses of BOL and EOL), using t-test with p-value less than 1%. Figure 5.2(b) presents the difference between the mean values for the available sample sets, where the error bars are calculated based on the standard deviation of the obtained thicknesses. There is ~40% reduction in the MPL thickness in the EOL sample, due to degradation. The reduction in the thickness is the first evidence of MPL degradation due to corrosion and material (either carbon/PTFE) loss. This is going to be discussed in the next sections.

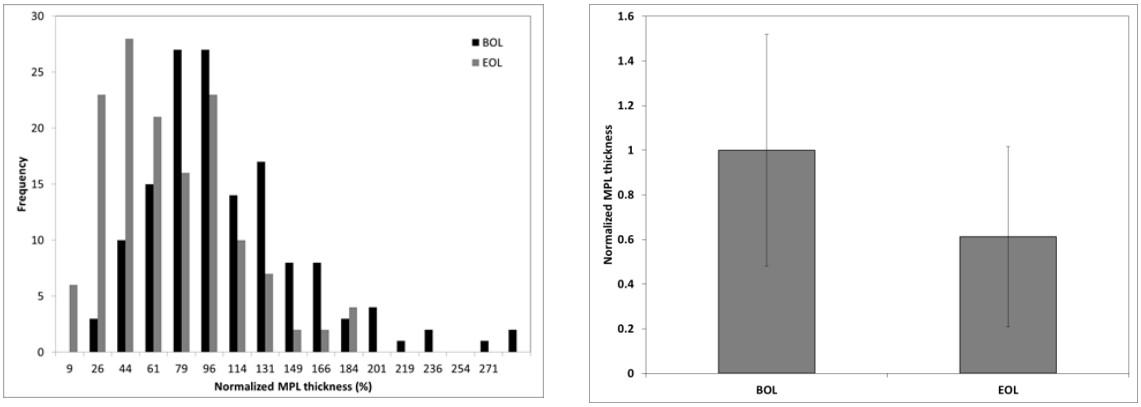

(a) (b)

Figure 5.2. (a) Distribution of normalized BOL and EOL MPL thickness; and (b) the normalized mean values of MPL samples.

5.2.2. Structure Changes

The changes in the GDL structure can reveal insightful information about the undergone phenomena during its degradation. Here, the powerful XCT systems at FCReL (i.e., micro-scale Versa and nano-scale Ultra) are utilized to capture the 3D structure of the entire GDL. Due to the intrinsic differences in the substrate and MPL structures, different instruments should be implemented for each layer. Versa, which is our micro-scale scanner, is used to visualize the substrate structure and Ultra, which is the nano-scale scanner, is used for MPL. Several steps of image processing and noise reduction algorithms were performed, using Avizo®, prior to the 3D structure generation. The procedure for obtaining the 3D structure from the raw images is explained in our previous work [133].

The average obtained porosity for the BOL and EOL substrates are 75% and 71%, respectively, and the changes in the through plane GDL porosity for these samples are shown in Figure 5.3. The porosity is reduced from the GDL surface towards its core for both samples, and it has its smallest value close to the mixed MPL-substrate region (where the MPL particles penetrate into the substrate's pores). The BOL and EOL porosities are similar on the left portion of the diagram (up to ~70% of the thickness). However, the EOL sample has lower porosities close to the mixed substrate-MPL region. Considering the observed reduction in the MPL thickness for the EOL, one reason for this difference in porosity can be the collapse of structure and movement of particles from MPL towards the substrate, as a result of corrosion of carbon particles in the MPL during the cathode corrosion accelerated stress tests. The other reason for this profile can be the flatter surface of the EOL sample due to either corrosion or MEA assembly during the fuel cell operation.

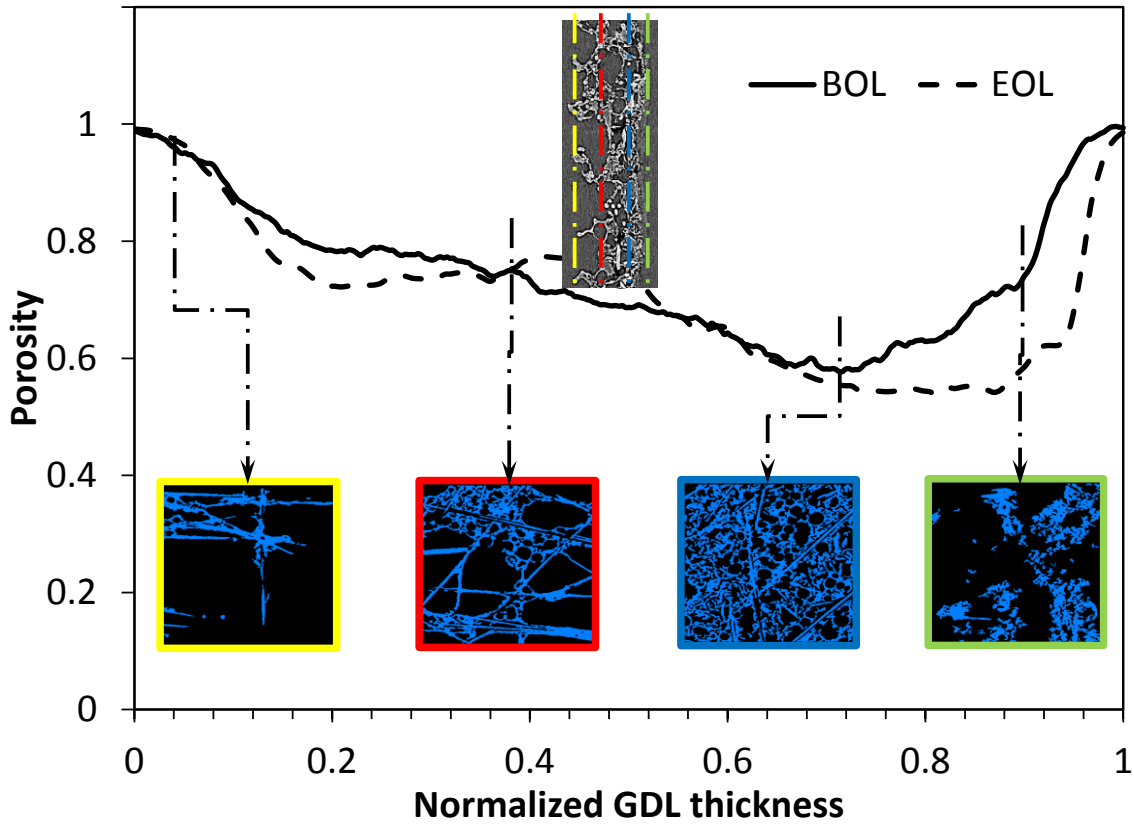

Figure 5.3. Through-plane porosity of GDL for the BOL and EOL samples obtained by using Versa with 0.6 μm voxel size at 50 kV acceleration voltage and 4 W power. The sample structures at the bottom are the binarized images at various cross sections that are highlighted by colored borders corresponding to the colored lines shown in the GDL image at the top.

The question of structure collapse in the MPL, due to corrosion, can be answered by imaging the MPL structure at higher resolution. The obtained data from our nano-scale scanner is therefore used to reconstruct the 3D structure of MPL in both BOL and EOL conditions. The structure is then used in a numerical framework, developed at FCReL [71,88], to calculate the MPL pore size distribution (PSD) and porosity. Shown in Figure 5.4 are the pore size distributions for the available MPL samples. The data are calculated based on the PSD of three different 4.5 μm cubic domains for each sample type. The average pore sizes are 168 and 144 nm for the BOL and EOL samples, respectively, with approximately identical porosity values of 52±2%. The smaller average pore size in the EOL sample can be attributed to partial collapse of the MPL structure due to the structure weakening as a result of corrosion of carbon particles. The extent of

the thickness reduction and associated material loss (~40%) suggests that it is dominated by carbon corrosion rather than PTFE loss, considering that the original MPL contains more carbon than PTFE.

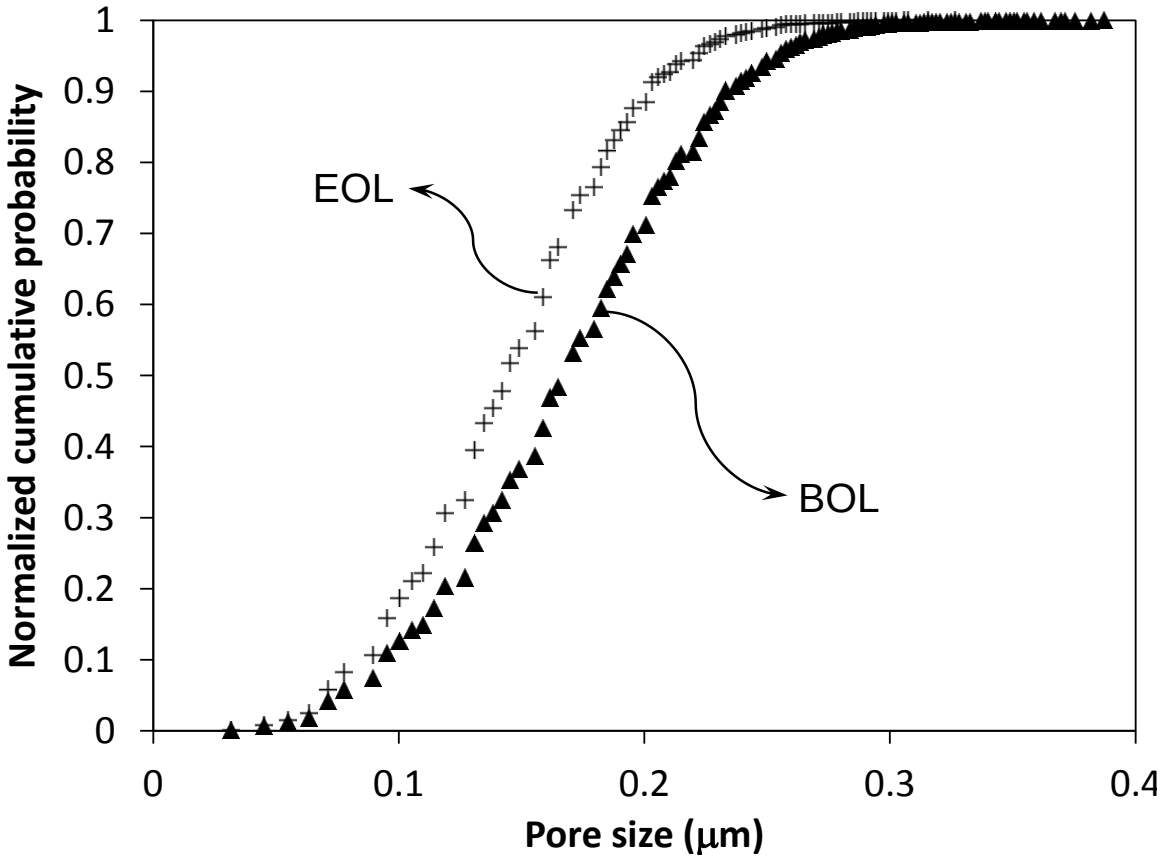

Figure 5.4. MPL pore size distributions for the BOL and EOL samples obtained from reconstructed 3D structure of the samples using Ultra at 16 nm voxel size. Each curve is plotted after averaging the PSD of three cubic domains of 4.5 μm.

5.2.3. BOL and EOL Properties

The BOL and EOL effective oxygen diffusivity and thermal conductivity are calculated by the developed analytical models in Chapter 2 and Chapter 3, respectively. The obtained pore size distributions in section 5.2.2 (*cf*. Figure 5.4) are used to calculate the primary and secondary pore sizes required by the analytical models and the results are listed in Table 5.1.The results show that the effective diffusivity of the EOL sample was reduced by ~12% and the effective thermal conductivity had a slight reduction of ~5%. The reduction in the gas diffusivity for the EOL sample was predictable due to the

structure collapse and reduction in the average pore size (i.e., 144 nm for the EOL compared to 168 nm for the BOL). This is in line with our findings in Chapter 2 which is published in Ref [72]. The slight change in the effective thermal conductivity can also be attributed to the Knudsen effects. The smaller pore size, in the EOL sample, reduces the gas conductivity in the gas phase domain. Since the base of the present analytical model is [121], in which the effective thermal conductivity has a direct relationship with the gas conductivity inside the pores of the porous medium, the reduction in pore size affected the gas conductivity and hence the overall effective conductivity.

Table 5.1 Effective oxygen diffusivity and thermal conductivity of BOL and EOL samples*.

Property	BOL	EOL
Relative diffusivity	0.16±0.01	0.14±0.01
Effective thermal conductivity (W m^{-1} K^{-1})	0.18±0.01	0.17±0.02

*The values are calculated using the analytical models presented in Chapter 2 and Chapter 3

One of the main functions of MPL is enhancement in water management. Therefore, hydrophobicity of MPL is one of its key properties. High capillary pressure is an identification of a hydrophobic material. Two main factors can influence the capillary pressure in a porous medium: *i*) the surface contact angle, and *ii*) the pore size. Eq. (40) shows the relationship between the surface tension γ, contact angle θ, pore size r, and capillary pressure p_c.

$$p_c = \frac{2\gamma \cos\theta}{r} \tag{40}$$

Contact angle in this work is measured using a static sessile drop test by a goniometer at SFU 4D LABS. Figure 5.5 presents the measured contact angle values. Each data point is obtained from seven measurements and the error bars are calculated based on the standard deviation. Surface contact angle, apart from the material type, is a function of surface roughness and heterogeneity [134]. There is a slight decrease in the mean value of the contact angle for the EOL sample; however, the difference is not statistically significant. This shows that the surface roughness and heterogeneity is not changed significantly during the degradation process. It also suggests that the level of

PTFE loss at the surface of the MPL is negligible, which again indicates a carbon corrosion dominated degradation process.

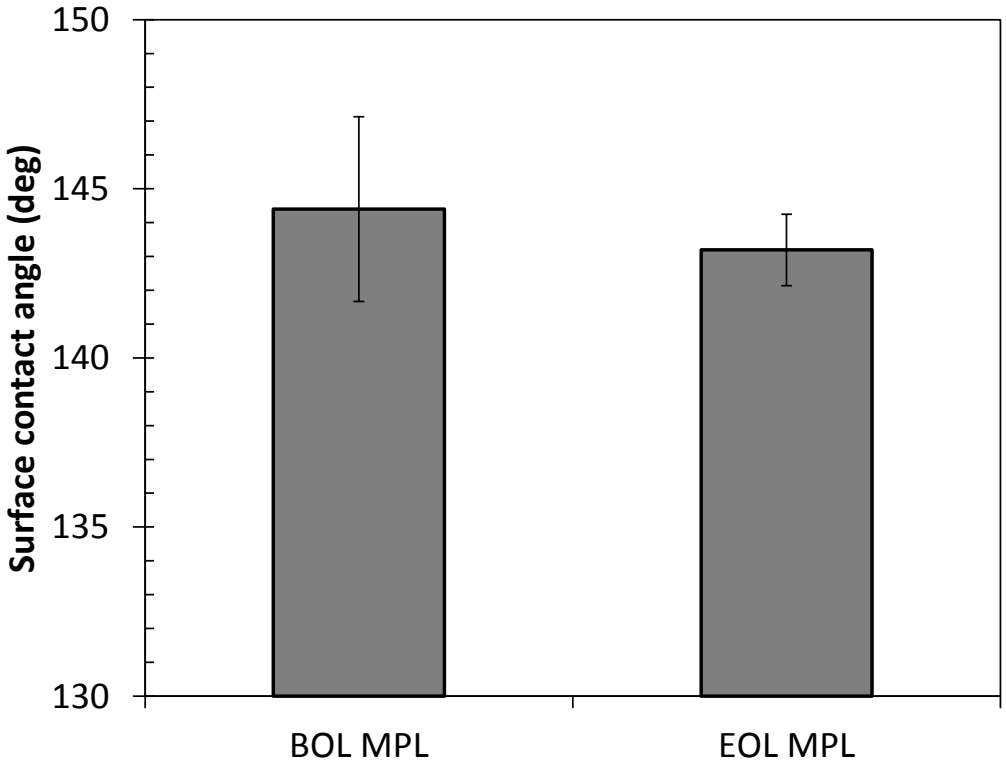

Figure 5.5. The contact angle for the BOL and EOL samples, measured by static sessile drop technique using a goniometer.

5.3. Conclusions

The structural changes in a degraded GDL (substrate + MPL) were investigated in this chapter. It was observed that in the degraded sample, the MPL thickness was reduced and the MPL-substrate overlap was increased. Thus, it can be concluded that the following mechanism is possibly dictating the MPL degradation:

- Corrosion of carbon particles
- Loss of carbon in form of CO and CO_2 (material loss from the structure)
- Weakening of structure due to loss of carbon
- Collapse of the weakened structure under compression
- Reduction of the thickness as a result of collapse

- Intrusion of MPL particles into the substrate

Note that more investigation is required to make a solid conclusion on the degradation mechanism; specifically, more samples are needed to verify that the difference in the porosity profiles for the BOL and EOL samples are not due to sample variability.

In summary the observed changes in the MPL properties, after degradation, can be listed as the following.

- Reduction of average pore size
- Reduction of diffusivity
- Slight reduction of thermal conductivity
- No change in hydrophobicity or surface roughness

Chapter 6.

Fuel Cell Modeling, Part I: Hygrothermal PEFC Model

The initial step towards developing a performance model is undertaken by building up a simpler hygrothermal model. This chapter describes this model which is used to investigate the thermal and hydration behavior of PEFCs. Sections 6.1 to 6.3 discuss the model geometry and the implemented numerical approach. In section 6.4 model validation is performed by comparing the results from the available numerical model to experimental data. Section 1.1 presents the effects of various parameters and scenarios on hygrothermal behavior of the cell.

6.1. Model Geometry

Ballard FCgen®-1020ACS air-cooled stack is chosen as the pilot for building and validating the hygrothermal model. Low humidity air-cooled stacks operate in a very non-uniform hydration states. Therefore, they are suitable candidates for hygrothermal studies, where we are interested in observing the non-uniformities in the MEA hydration. The left part of Figure 6.1 shows a schematic of this stack, which consists of a variable number of cells that are stacked vertically. The cathode channels used jointly for oxygen supply and cooling are straight and the air is provided by a fan placed near the outlet. On the anode side, the channels are dead-ended and filled by stagnant pressurized hydrogen. The hydrogen channels are purged periodically during operation. In this analysis, one cell of a generalized open cathode stack is modeled and the governing equations for its heat and mass transfer are solved numerically in three dimensions. The geometrical model and boundary conditions are depicted in Figure 6.1. Periodic boundary conditions are applied at the top and bottom sides of the plate, which is representative of a given cell in the main body of the stack. Note that the symmetric boundary is invalid in this case due to the lack of symmetry in the x-z plane and heat

transfer between adjacent cells. For the inlet and outlet boundaries, constant pressure is set, and the inlet air composition based on the ambient relative humidity and temperature is defined. The cell shown in Figure 6.1 (b) has a symmetry boundary condition at the central symmetry plane on the right and a convection heat transfer boundary condition at the edge of the cell on the left. The positions of the main MEA components including the catalyst coated membrane (CCM) and GDLs that are considered in this model are shown in Figure 6.1 (d).

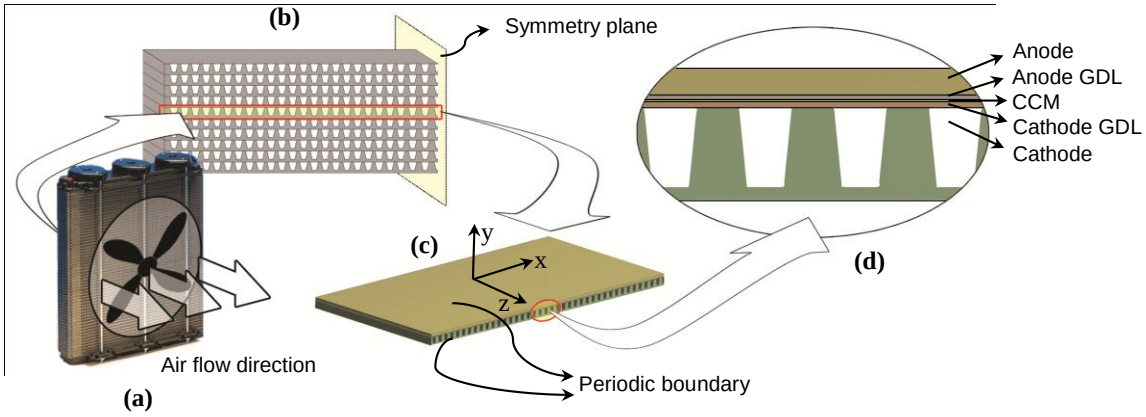

Figure 6.1. Model geometry, cell components, and boundary conditions: (a) the actual air-cooled stack (FCgen®-1020ACS); (b) half stack model geometry; (c) half-cell model; (d) detailed view of the cell with the considered components.

6.2. Governing Equations

The physics of the hygrothermal model are governed by the conservation of mass, momentum, chemical species, and energy. Since the channel Reynolds number is less than 2300, even for the highest volumetric flow rate considered in this research, laminar flow is assumed. In addition, the flow is incompressible as a result of low Mach numbers inside the channels.

The general form of the mass conservation equation for an incompressible steady state flow is shown in Eq. (41), in which ρ is the gas mixture density, $\vec{V}$ is the velocity, and S_{mass} is the mass source term for the electrochemical reactions in the cell:

$$\nabla.(\rho\vec{V}) = S_{mass} \tag{41}$$

$$S_{mass} = -\frac{M_{O_2} J}{4F} + \frac{M_{H_2O} J}{2F} \tag{42}$$

In Eq. (42), *M* is the molar mass, *F* is the Faraday's constant, and *J* is the volumetric current density. Here, *J*, which is equal to the current density divided by the CCM thickness, is assumed to be known *a priori* based on the measured current density distributions. More details about this assumption are explained in section 6.4.

Conservation of momentum is brought in Eq. (43), where *p* is the gas pressure and μ is the mixture viscosity that can be obtained from the mass-weighted mixing law theory shown in Eq. (44):

$$\nabla.\rho\vec{V}\vec{V} = -\nabla p + \nabla.(\mu\nabla.\vec{V}) + S_{Mom} \tag{43}$$

$$\mu = \sum_i \frac{\chi_i \mu_i}{\sum_j \chi_j \phi_{ij}}, \qquad i, j = O_2, N_2, H_2O \tag{44}$$

In Eq. (44), χ_i is the mole fraction of each chemical species and ϕ_{ij} has the following formulation:

$$\phi_{ij} = \frac{\left[1 + \left(\frac{\mu_i}{\mu_j}\right)^{1/2} \left(\frac{M_j}{M_i}\right)^{1/4}\right]^2}{\left[8\left(1 + \frac{M_i}{M_j}\right)\right]^{1/2}} \tag{45}$$

The last term in the momentum equation is the source term which is only non-zero in the porous GDL and CCM layers. In other words, a sink is added to the general momentum equation that represents the flow resistance due to the existence of porous materials. This source term can be obtained from the following equation:

$$S_{Mom} = -\frac{\mu}{\kappa}\vec{V} \tag{46}$$

where κ is the gas permeability inside a porous medium.

Conservation of energy and chemical species equations are shown in Eqs. (47) and (48), respectively:

$$\nabla.\left(c_p \rho \vec{V} T\right) = \nabla.\left(k \nabla T\right) + S_T \tag{47}$$

$$\nabla.\left(\rho \vec{V} Y_j\right) = \nabla.\left(\rho D_{eff} \nabla Y_j\right) + S_j \qquad j = O_2, N_2, H_2O \tag{48}$$

where c_p is the specific heat of the mixture calculated from Eq. (49) and k is the mixture thermal conductivity obtained based on the weighing model used for the viscosity (*cf*., Eq. (44)). Y_j is the mass fraction of the j^{th} species in the mixture and D_{eff} is the effective diffusion coefficient, assumed to be constant.

$$c_p = \sum_i Y_i c_{p,i} \tag{49}$$

The last terms in Eqs. (47) and (48) are the source terms. In Eq. (47), the source term is the total heat generation rate which consists of reversible and irreversible heat losses calculated from Eq. (50) [135]. Similarly in Eq. (48), the source term represents consumption of oxygen and production of water vapor obtained from Eq. (51):

$$S_T = (E_{th} - V_{cell})J \tag{50}$$

$$S_{O_2} = -\frac{J}{4F} M_{O_2}, \quad S_{H_2O} = \frac{J}{2F} M_{H_2O} \tag{51}$$

In Eq. (50), E_{th} is the thermal voltage [26] defined by Eq. (52) and V_{cell} is the cell voltage. The cell voltage and current density distribution are applied based on measured data.

$$E_{th} = \frac{-\Delta H}{2F} \tag{52}$$

Here, the low heating value of hydrogen, ΔH, is used to calculate the thermal voltage, i.e., the product water is assumed to be generated in the vapor phase. Furthermore, since the stack operates at low humidity conditions, high air flow rates, and relatively low current densities, it is expected that there will be no water vapor condensation. In contrast to most previous cell/stack level simulations, see for example [136], a uniform current density assumption is not required in the present model, which is essential for accurate modeling of open cathode devices with large gradients. Here, the coupled heat and mass transfer equations are solved simultaneously and the distribution of heat and water vapor generation is assumed to be a function of the current density distribution.

6.3. Numerical Scheme

Commercial software, ANSYS Fluent 14.0, is used to solve the governing equations. The SIMPLE algorithm is implemented to solve the pressure-velocity coupling and the power-law scheme is used for the discretization of the equations. A mesh independency study is performed for different mesh sizes, and finally a structured mesh with 3.1 million cells is chosen. For the convergence criterion of 1.0e-6 for the absolute error, the solution converges after 250 iterations. This number will increase to 500 if 1.0e-12 is chosen for the convergence criterion. Approximately 4 to 6 hours are required for 500 iterations in parallel mode with 4 cores on an Intel® Core™ i7 Processor system with 12 GB RAM.

The unique cell-level hygrothermal model of an open cathode air-cooled fuel cell developed in this work is first validated with experimental data measured using a standard stack configuration and then applied to investigate the key hygrothermal characteristics of the stack under a range of typical operating conditions.

6.4. Model Validation

Figure 6.2 shows the normalized current density distribution measured at different locations in a single cell within a Ballard Power Systems FCgen®-1020ACS stack. The normalization is performed based on the average cell current density. Experimental observations show that the normalized current density distribution is essentially independent of the stack power rating. Therefore, it is possible to use the same normalized distribution for different stack power levels. This assumption is valid as long as no major changes are made in the stack geometry. Moreover, as inferred from Figure 6.2, the variations of current density along the downstream position, z/z*, are small. Hence, it is assumed that the current density is only a function of the lateral position, i.e., the distribution is one dimensional.

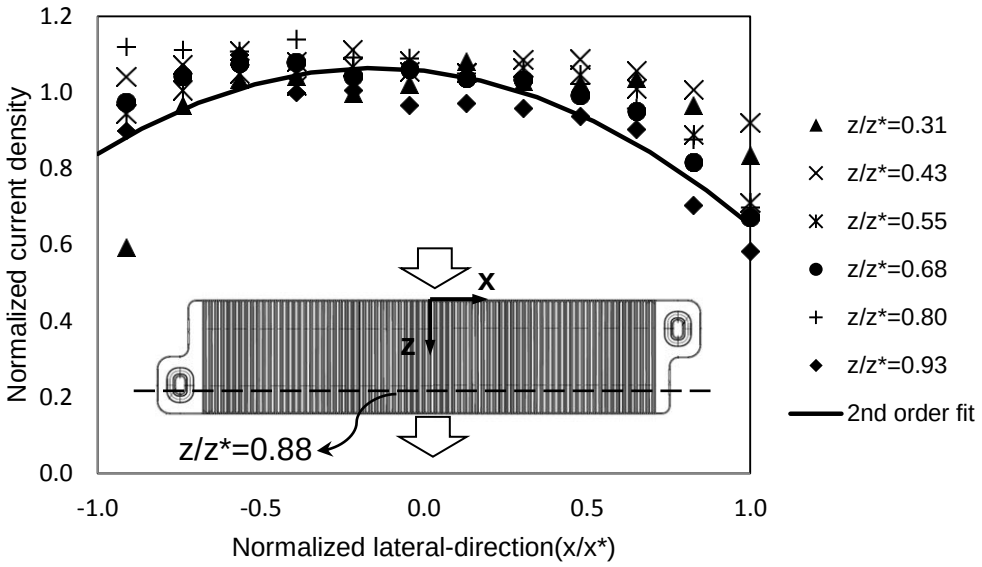

Figure 6.2 Normalized current density distribution measured at different downstream positions (indicated by the symbols) along the lateral direction (indicated by the dashed line) of a single cell in the center of the stack.

To examine the validity of these two assumptions, two different scenarios are considered. In the first one, the simulated temperatures by using 1D and 2D current density distributions are compared to the measured temperature data. Figure 6.3 shows the temperature distribution along the lateral direction in the cell at the downstream position of z/z* = 0.88 for the first scenario. The difference between implementation of

1D and 2D distribution is less than 2.8%. Hence, variations of current density along the channel direction can be neglected.

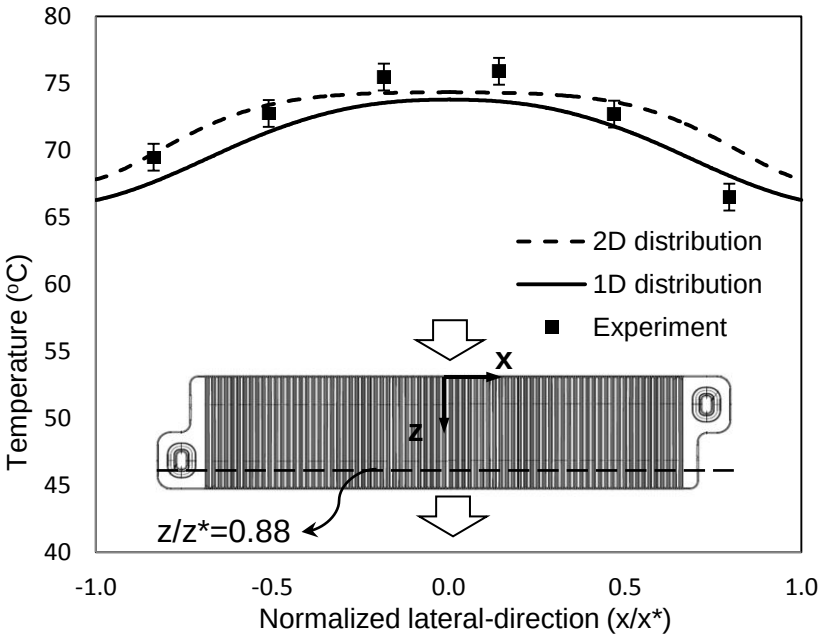

Figure 6.3. Temperature distribution at z/z* = 0.88. Square symbols represent experimental data; solid line indicates modeling results with 2D current distribution assumption; and dashed line shows modeling results with 1D current distribution assumption.

In the second scenario, simulated and measured temperatures for two typical stack power levels are compared at z/z* = 0.88. Since the 1D current density distribution provides reasonable accuracy, the same assumption is used here. Details on the stack operating conditions for the two power levels are tabulated in Table 6.1. Demonstrated in Figure 6.4 are the obtained results for this scenario. Good agreement can be seen between the model predictions and the experimental measurements. As shown in Figure 6.4 for x/x* > 0, which indicates the right half of the cell, the deviation between the present numerical model and the experimental data is larger. This is due to the assumption of symmetric boundary condition at the center. The FCgen®-1020ACS stack does not have completely symmetric cells and the current density distribution, as a consequence of the non-uniform temperature distribution, is not fully symmetric (*cf.*, Figure 6.2). In general, the numerical results from the model are in good agreement with the experimental data and the maximum relative difference is less than 6%.

Table 6.1. Operating conditions of the stack used for model validation.

	Case A	Case B
Stack current (A)	87.0	57.1
Cell voltage (V)	0.569	0.712
Air flow rate (lpm)	86.7	29.6
Ambient temperature (°C)	21	20

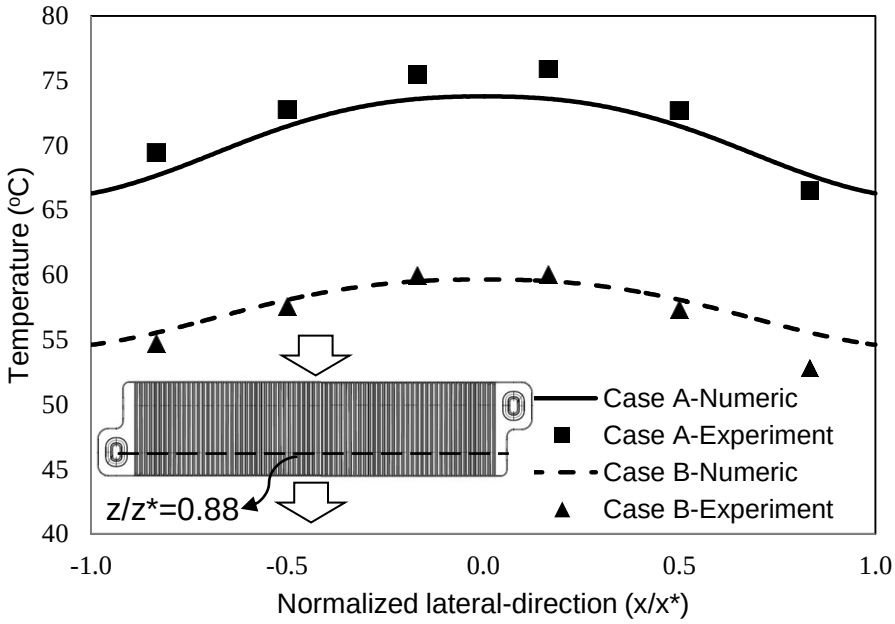

Figure 6.4. Temperature distribution at z/z* = 0.88 for two stack power levels obtained by the present model (lines) and from the measurements (symbols).

6.5. Baseline Case

An open cathode cell with the dimensions and operating conditions listed in Table 6.2 is considered as the baseline case. The conditions assumed for the baseline case represent a fuel cell with an efficiency of 50% and power output of 110 W per cell. The simulated temperature contours for this case are shown in Figure 6.5(a). The maximum temperature is predicted to occur at the outlet of the central channel and the

temperature gradients in the cell have the same trends as the experimental data. The maximum temperature for this case is calculated to be 79.5 °C.

Table 6.2. Baseline case conditions.

Parameter	Value
Stack current	80 A
Cell voltage	0.57 V
Air flow rate	51.5 lpm
Ambient temperature	20 °C
MEA thickness	500 μm
Cathode channel height	3.0 mm
Anode thickness	1.0 mm
Rib width	1.5 mm
Cathode channel length	70.0 mm
Number of cathode channels	80
Flow distribution	Uniform

The simulated RH contours at the interface between the cathode GDL and CCM for the baseline case are presented in Figure 6.5(b). In contrast to typical liquid-cooled PEFCs with gas humidification, air-cooled PEFCs operate under remarkably dry conditions. Provided that ambient air supply of low temperature and humidity is utilized directly on the cathode, the average RH value in the cathode side of the air-cooled stack is much lower than those of other types of PEFCs. This can be seen in Figure 6.5(b), where the RH is ranging from 10% to 35% for the baseline conditions. The RH is higher under the lands, where the water vapor transport from the MEA to the channel is more constrained than directly under the channel. Moreover, although the water generation rate is higher close to the center of the cell, the RH is lower at those locations. This shows the high dependence of RH on temperature, thus demonstrating the important hygrothermal coupling of the open cathode design. The driest portion of the cell coincides with the highest temperature, which indicates that excessive heat generation can overshadow water production in terms of the overall hygrothermal performance of the cell.

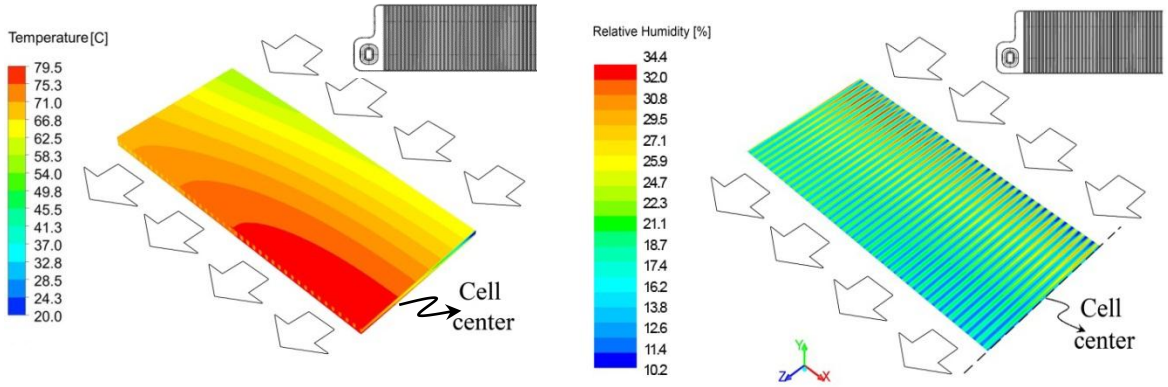

(a) (b)

Figure 6.5. Simulated (a) temperature and (b) RH contours for the baseline open cathode fuel cell. The modeling domain shown here is the left half of a single cell in the stack.

6.6. Conclusions

A hygrothermal model was developed as a basis for a more complex performance model. An air-cooled stack was chosen for model verification. The characteristics of open cathode PEFC stacks can be examined by the developed model under various flow and design conditions. The model was extensively validated with experimental data. Significant coupling of temperature and humidity was observed and comprehensively addressed under various conditions. Areas of abnormally high or low temperature and humidity as well as major temperature and humidity gradients were recognized and thoroughly assessed based on the complete cell domain.

Chapter 7.

Fuel Cell Modeling, Part II: Performance Model

In this chapter, details of the developed performance model for studying the impacts of MPL properties on PEFC performance are explained. Since the focus of this study is only on the MPL, the model geometry is reduced in size from a full plate to a unit cell composed of single anode and cathode channels and the MEA components. Model geometry and the numerical approach are described in sections 7.1 to 7.3, model validation in performed in section 7.4 and the impact of MPL thermal/electrical conductivity and diffusivity on PEFC performance is investigated in section 7.5.

7.1. Model Geometry

As mentioned in the chapter preface, the domain size is reduced from one full size cell to two parallel channels, representing the anode and cathode flow fields. The cell geometry and the considered MEA components in the model are shown in Figure 7.1. In this work, the GDL is assumed to consist of a carbon fiber substrate and a homogeneous MPL. The model dimensions and physical properties of different components are listed in Table 7.1.

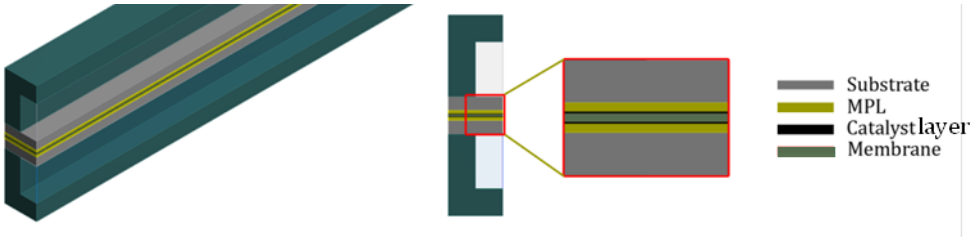

Figure 7.1. Model geometry and the considered MEA components in the model.

Table 7.1. Dimensions and physical properties of the model components.

Model geometry	
Anode and cathode channel height, H	1 mm
Channel length, L	60 mm
Channel width, w	1 mm
Rib width, r_b	1 mm
Anode and cathode substrate thickness, t_{subs}	0.254 mm
Anode and cathode MPL thickness*, t_{MPL}	0.02 mm
Anode and cathode catalyst layer thickness, t_{cat}	0.013 mm
Membrane thickness, t_{mem}	0.051 mm
Physical properties	
k_{subs} , k_{MPL} , k_{cat} , k_{mem}	1.5, 0.5, 1.5, 0.16 W m^{-1} K^{-1}
$\kappa_{subs}, \kappa_{MPL}, \kappa_{cat}$	7.3×10^{-12}, 5.0×10^{-13}, 7.3×10^{-13} m^2
$\sigma_{subs}, \sigma_{MPL}, \sigma_{cat}$	2500, 1500, 800 S m^{-1}
$\theta_{subs}, \theta_{MPL}, \theta_{cat}$	110^o, 140^o, 100^o

* MPL properties are for the baseline case.

7.2. Governing Equations

The coupled thermo-electro-chemical model is an upgrade to the thermal model, in which thecurrent density distribution and heat generation profiles are not an input to the model. Conservation of mass, momentum, energy, and chemical species are solved in flow fields, GDLs, and catalyst layers. In the catalyst layers, apart from the aforementioned conservation equations, the electron and proton transport equations are also solved. In the membrane, which is assumed to be solid, the energy equation along with the transport of proton and dissolved water are solved. Liquid water transport is also added to the model by assuming condensation of water vapor into liquid phase when the partial pressure of water vapor is higher than the saturation pressure of water at that specific temperature.

The new equations and their corresponding source terms are respectively listed in Table 7.2 and Table 7.3, based on the regions in which they are being solved.

Table 7.2. The list of governing equations in each computational domain.

	Transport equation	Corresponding zones	Equation number
Chemical species	$\nabla.\left(\rho\vec{V}Y_i\right)=\nabla.(D_{eff,i}\nabla Y_i)+S_i$	flow field, catalyst layers, substrates, MPLs	(53)
Electron transport	$\nabla.(\sigma_{eff}^{s}\nabla\phi_s)-S_{pot}=0$	catalyst layers, substrates, MPLs, bipolar plate	(54)
Proton transport	$\nabla.(\sigma_{eff}^{m}\nabla\phi_m)+S_{pot}=0$	catalyst layers, membrane	(55)
Dissolved water	$\nabla.\left(-\frac{2.5M_{H_2O}}{22F}\sigma_{eff}^{m}\nabla\phi_m\lambda-\frac{\rho_m}{M_m}D_{H_2O,eff}^{m}\nabla\lambda\right)=0$	Membrane	(56)
Liquid water transport	$-\nabla.\left(\rho_l D^c\nabla s\right)=\dot{m}_{H_2O}$	substrates, MPLs, catalyst layers	(57)

Table 7.3. Source terms at each zone.

Source term	Zone	Value	Equation number
S_{mass}	cathode catalyst	$-\frac{M_{O_2}J_c}{4F}+\frac{M_{H_2O}J_c}{2F}$	(58)
	anode catalyst	$-\frac{M_{H_2}J_a}{2F}$	
	elsewhere	0	
S_i	O_2 cathode catalyst	$-\frac{M_{O_2}J_c}{4F}$	(59)
	H_2O cathode catalyst	$\frac{M_{H_2O}J_c}{2F}$	
	H_2 anode catalyst	$-\frac{M_{H_2}J_a}{2F}$	
	elsewhere	0	
S_{pot}	cathode catalyst	$-J_c$	(60)
	anode catalyst	$-J_a$	
	elsewhere	0	
S_{temp}	cathode catalyst	$J_c\left(-T\Delta S+\lvert\eta_c\rvert\right)+\sigma_{eff}^{m}\left(\nabla\phi_m\right)^2$	(61)

	anode catalyst	$J_a\eta_a + \sigma_{eff}^m \left(\nabla\phi_m\right)^2$	
	membrane	$\sigma_{eff}^m \left(\nabla\phi_m\right)^2$	
$\dot{m}_{H_2O}$	substrates, MPLs, catalyst layers	$\max\left\{(1-s)\frac{p_{H2O}^g - p_{H2O}^{sat}}{RT}M_{H2O}, -s\rho^l\right\}$	(62)

The physical properties of the mixture such as viscosity, μ, and effective thermal conductivity, k_{eff}, are obtained based on the mass-weighted mixing law for mixtures [141]. In Eq. (53), the effective mass diffusivity of the *i*th species in the mixture, $D_{eff,i}$, is calculated from Eq. (63).

$$D_{eff,i} = \frac{1-\chi_i}{\sum_{j\neq i}^{N} D_{ij}}, \qquad i = O_2, N_2, H_2O, H_2 \tag{63}$$

In the above equation, D_{ij}, is the binary mass diffusion coefficient that can be found in the literature at standard pressure and temperature [142]. Here, those values are modified based on the local temperature and pressure by using Eq. (64). In Eq. (64), P^0 and T^0 are the standard pressure and temperature, i.e., 289.15 K and 1 atm.

$$D_{ij} = D_{ij}^0 \left(\frac{P^0}{P}\right)\left(\frac{T}{T^0}\right)^{1.5} \tag{64}$$

In the porous substrate, MPL, and catalyst layer the value of effective diffusivity needs to be modified to account for the effects of porosity. Several works in the literature used the Bruggeman's approximation to obtain the effective gas diffusivity in those regions [143–147]. However, comparing the Bruggeman model's result with the recent measurements of the effective diffusivity for GDLs and catalyst layers, remarkable discrepancy could be observed [46]. Therefore, in this work the effective mass diffusivity in these components is assumed based on the recent published data and the analytical models developed in this research. Values for the effective electron conductivity, σ_{eff}^s, in the substrate, MPL, and catalyst layer are also adopted from literature [5,45]. For the

effective proton conductivity, σ_{eff}^{m}, in the membrane and catalyst layers the relation proposed by Springer *et al*. [15] is used.

$$\sigma_{eff}^{m} = (0.5193\lambda - 0.326)\exp\left[1268\left(\frac{1}{303.15} - \frac{1}{T}\right)\right] \tag{65}$$

In the catalyst layer the value obtained from Eq. (65) is corrected by the volume fraction of ionomer. λ in Eq. (65) is the water content which is obtained from solving the dissolved water transport equation, Eq. (56). In the dissolved water transport equation, the first term is the electro-osmotic drag in which the electro-osmotic drag coefficient $\frac{2.5\lambda}{22}$ is substituted from [15], and the second term is the back diffusion flux. The bulk density of dry membrane, ρ_m, is assumed to be 2000 kg m^{-3}, the membrane equivalent weight, M_m, is considered as 1.1 kg mol^{-1}. The effective membrane water diffusivity is also found from Eq. (66) [15].

$$D_{H_2O,eff}^{m} = \begin{cases} 3.1\times10^{-7}\times\lambda\left[\exp(0.28\lambda)-1\right]\exp(-\frac{2436}{T}) & \text{for } \lambda \le 3 \\ 4.17\times10^{-8}\times\lambda\left[1+161\exp(-\lambda)\right]\exp(-\frac{2436}{T}) & \text{for } \lambda > 3 \end{cases} \tag{66}$$

In Table 7.3, the anode and cathode volumetric exchange current densities, J_a and J_c, are obtained from the modified Butler-Volmer (BV) kinetics model, Eqs. (67) and (68).

$$J_a = j_a^{ref}\left(\frac{[H_2]}{\left[H_2^{ref}\right]}\right)^{0.5}\left[\exp\left(\frac{F}{R_uT}\eta_a\right) - \exp\left(\frac{-1.5F}{R_uT}\eta_a\right)\right] \tag{67}$$

$$J_c = j_c^{ref}\left(\frac{[O_2]}{\left[O_2^{ref}\right]}\right)\left[-\exp\left(\frac{F}{R_uT}\eta_c\right) + \exp\left(\frac{-1.5F}{R_uT}\eta_c\right)\right] \tag{68}$$

Due to the reported high kinetic rates for the anode reaction, the anode volumetric reference exchange current density is set to 10^9 A m^{-3} but the temperature dependence of the cathode volumetric exchange current density is found from Eq. (69).

$$j_c^{ref} = j_{c,0}^{ref} \exp\left[-\frac{73270}{R_u}\left(\frac{1}{T}-\frac{1}{353.15}\right)\right] \tag{69}$$

In Eqs. (67) and (68), the anode and cathode overpotentials, η_a and η_c, are defined as follows:

$$\eta_a = \phi_s - \phi_m \tag{70}$$

$$\eta_c = \phi_s - \phi_m - E_{rev} \tag{71}$$

where the reversible potential is obtained from Eq. (72).

$$E_{rev} = 1.23 - 0.85\times10^{-3}(T-298.15) + \frac{R_u T}{4F}\ln\left[O_2\right] \tag{72}$$

In the liquid water transport equation, Eq. (57), the transport of liquid water is based on the capillary pressure gradient inside the porous medium. A semi-empirical relation correlating the capillary pressure and saturation data for clean unconsolidated sands of various permeability and porosity is obtained in [148].

$$P^c = \gamma\cos\theta\left(\frac{\phi}{\kappa}\right)^{1/2} J(s) \tag{73}$$

where $\gamma = 6.25\times10^{-2}$ N m^{-1} is the surface tension, θ is the surface contact angle, ϕ is the porosity, κ is the permeability, *s* is the saturation level, and *J(s)* is the Leverett J-function found by Eq. (74) [149].

$$J(s)=\begin{cases} 1.417(1-s)-2.12(1-s)^2+1.263(1-s)^3 & if\ \theta<90^\circ \Rightarrow \text{Hydrophilic} \\ 1.417s-2.12s^2+1.263s^3 & if\ \theta>90^\circ \Rightarrow \text{Hydrophobic} \end{cases} \quad (74)$$

7.3. Numerical Scheme

The above-mentioned governing equations in Section 7.2, are highly coupled and should be solved numerically. ANSYS Fluent® software is used for solving the governing equations. A relatively complicated User Defined Code (UDF) is written and compiled with this software to add the constitutive equations. The pressure-velocity coupling is addressed by SIMPLE algorithm and all the transport equations are discretized using the second order upwind method. A mesh independency study is performed for different mesh sizes, and finally a structured mesh with ~40000 cells is chosen, where in the through plane direction, 10 nodes for the anode and cathode catalysts, 10 nodes for the MPL, 25 nodes for the substrate, 12 nodes for the membrane, 32 nodes for the anode and cathode channels, and 12 nodes for the bipolar plate were considered.

Applying the boundary conditions particularly for the transport of dissolved water equation in the ionomer is complicated in ANSYS Fluent®. To address this issue, the local water content, λ, in the catalyst layer is calculated based on the local water activity using the Springer *et al*.'s model [15]. Then Eq. (56) is solved for the water content in the membrane with the known water content at the boundaries in anode and cathode catalyst layers.

$$\lambda=\begin{cases} 0.043+17.81a-39.85a^2+36a^3 & a\le 1 \\ 14+1.4(a-1) & 1<a\le 3 \\ 16.8 & a>3 \end{cases} \quad (75)$$

Modeling the flux of water into/out of membrane from/towards both anode and cathode catalyst layers is another challenging issue in ANSYS Fluent® software. This issue is tackled by assigning an equivalent source term in the first row of the computational cells adjacent to the membrane zone in both catalyst layers. The flux is calculated from Eq. (76).

$$\dot{m}''_{H_2O} = -\frac{2.5\lambda M_{H_2O}}{22F}\sigma^m_{eff}\nabla\phi_m - \frac{\rho_m}{M_m}M_{H_2O}D^m_{H_2O,eff}\nabla\lambda \quad (76)$$

Setting the other boundary conditions for the computational domain is straight forward. For the inlet to the channels, flow velocity and temperature as well as the mixture composition is assigned. For all the outer boundaries, temperature is set at the operating temperature of the stack. Pressure is set at both channel outlets. Cell voltage is set at the cathode end plate for the electrical potential equation and zero is set for the anode electrical potential. Zero flux boundaries are used for the proton transport equation at all the corresponding boundaries. Setting all boundary conditions, the simulations are performed using an Intel® Core™ i7 workstation with 12 GB of RAM.

7.4. Model Validation

The simulated polarization curve from the model is compared to the experimental investigation conducted by Siegel [150]. The experiments in [150] were performed under the conditions stated in Table 7.4. Qualitatively, the simulated polarization curve has an acceptable accuracy compared to the reported data. The difference between the simulated results and the experimental data could be associated with the uncertainties on the value used for the reference exchange current density. A wide range of values is reported in the literature for this parameter and in this work this parameter is fitted against the data of [150].

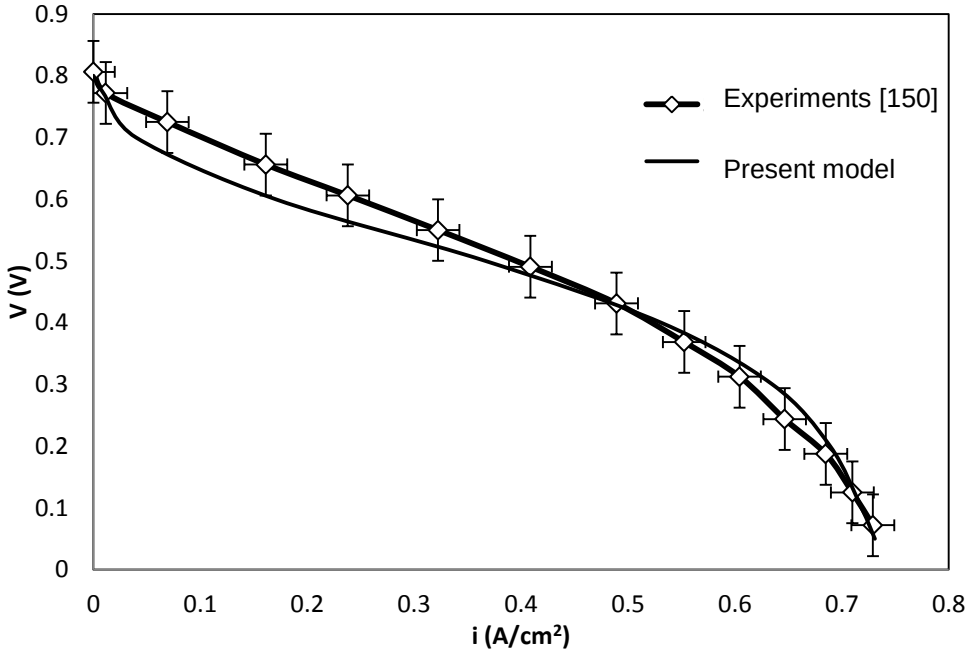

Figure 7.2. Comparison of the simulated polarization curve with the experimental data of [150]**.**

Note that the main purpose in global performance modeling of fuel cell is to predict the average current density under different operating conditions.

Table 7.4. Experimental conditions for the experimental investigation reported in [150]**.**

Variable	Value
Cathode inlet velocity (humid air)	8.932 m s^{-1}
Anode inlet velocity (humid H_2)	6.1 m s^{-1}
Operating pressure	142 kPa
Operating temperature	353 K
Anode and cathode humidity condition	Fully humidified

7.5. Case Studies

7.5.1. MPL Thermal and Electrical Conductivity

The effects of effective MPL thermal/electrical conductivity on performance is plotted in Figure 7.3(a) and (b), respectively. The model predicts that the dependence of

performance on these two parameters is negligible within the considered range. This can be attributed to the small thickness of MPL, compared to the entire GDL, which makes the MPL thermal/electrical resistance small, and diminishes its effect on performance.

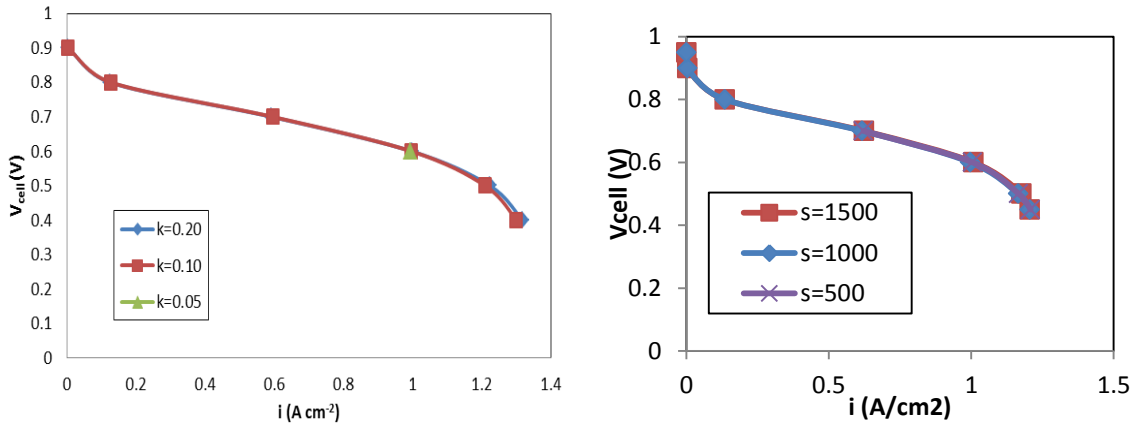

(a) (b)

Figure 7.3. Effects of (a) MPL effective thermal conductivity and (b) MPL electron conductivity on PEFC performance.

7.5.2. MPL Diffusivity

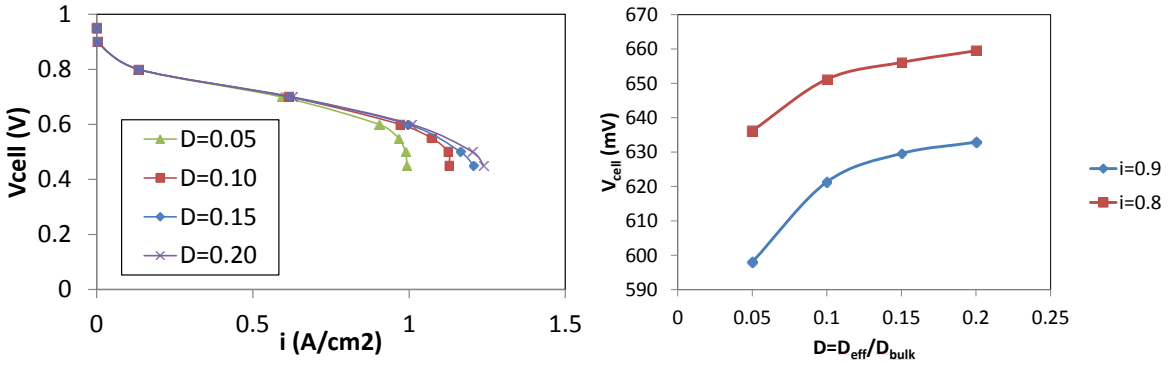

(a) (b)

Figure 7.4. Effects of MPL diffusivity on PEFC performance: (a)polarization curve; (b) cell voltage.

Depicted in Figure 7.4(a) are the polarization curves for the PEFC operating with the properties and conditions stated in Table 7.1. The only parameter that is varied is the effective diffusivity of the cathode MPL. It is observed in Figure 7.4(b) that the cell

voltage drops more than 20 mV at 0.8 and 0.9 $A.cm^{-2}$, when the relative effective diffusivity reduces from 0.2 to 0.05. The considered range of diffusivity in this study is taken from the literature values.

7.6. Conclusions

In this chapter a 3D numerical model was developed to predict PEFC performance. The model includes the anode and cathode substrates, MPLs, and catalyst layers, and a membrane in between. The model is capable of predicting the performance at various operating conditions and can be used to study the impact of various component properties on performance. Here, the parametric study was only performed on MPL electrical and thermal conductivity, and effective diffusivity. It was observed that the PEFC performance is more affected by the MPL diffusivity rather than thermal/electrical conductivity.

Chapter 8.

Conclusions and Future Works

8.1. Thesis Conclusions

In this thesis, MPL structure was reconstructed by using nano-scale computed tomography and two analytical models for estimation of the effective diffusivity and thermal conductivity were developed. The obtained methodology for reconstruction of the structure was applied to study the MPL structures of BOL and EOL samples and a possible pathway for MPL degradation was proposed. Furthermore, a numerical model was developed to predict the PEFC performance for different MPL properties. As a first step of that model another decoupled hygrothermal model was developed to study the hygrothermal behavior of a PEFC operating at low humidity conditions. In summary, followings are the findings resulted from this research.

- Analytical relationships were developed for estimation of MPL diffusivity and thermal conductivity.
- Accurate prediction of MPL effective diffusivity can be achieved only when the effect of pore size is considered.
- Increasing porosity and the secondary domain pore size, d_{II}, would increase the effective diffusivity.
- MPL effective thermal conductivity was measured at various compression pressures by exclusion of the contact resistance between the samples and the measurement instrument.
- A multi objective genetic algorithm was used to find an optimal pore size that operates optimally for mass and heat transfer.
- The 3D nanostructure of a standard MPL was determined and complete phase segregation of pore, carbon, and PTFE phases within the MPL material was performed by the low X-ray energy NXCT method and associated image processing techniques, without prior knowledge of the material composition.

- Carbon nanoparticles were shown to form an interconnected backbone of the solid phase of the MPL that provides a continuous pathway for solid phase transport, i.e., electrical and thermal conduction.
- The PTFE phase was found to form small, isolated island domains within the porous carbon phase rather than the previously anticipated film coating of the particles.
- The PTFE acted as a binder and structural support of the carbon nanoparticles and had surfaces exposed to the pore phase that are expected to facilitate the desired hydrophobicity of the internal pores of the MPL.
- The diffusive transport properties of the pore phase were quantified by the effective diffusivity of oxygen and water vapor, while the solid phase transport properties were quantified by the calculated effective electrical and thermal conductivities. The accuracy of these simulated properties benefit particularly from the new knowledge of the segregated phase distributions discovered in this work.
- The structural changes in a degraded GDL (substrate + MPL) were investigated and a possible MPL degradation mechanism was proposed.
- A degraded MPL sample was found to have smaller average pore size and effective diffusivity. Additionally, a slight change in the thermal conductivity and no significant change in surface contact angle were observed.
- PEFC performance was observed to be affected by MPL diffusivity.
- Thermal/electrical conductivity of MPL was observe not to significantly change the PEFC performance

8.2. Future Works

There were some steps that I was not able to perform due to time limitations and would be a nice addition to this research topic.

- The MPL phase segregation procedure was only done on one SGL sample. This approach can be further validated by more samples.
- The same approach can also be applied on fresh MPLs and degraded MPLs to assess the changes in PTFE distribution of degraded and fresh MPLs.
- In this research, the MPL degraded sample was taken out from MEAs which were under cathode catalyst corrosion accelerated tests. Preparing eroded samples and examining the possible changes in the structure can also reveal another possible MPL degradation mechanism.
- In the modeling side, it should be possible to develop an analytical model for electrical conductivity based on the thermal conductivity model, as they are

both having similar transport mechanism. Validation of the model is remaining as the future work.

- The liquid water transport sub-model can be upgraded to more advanced models to capture the saturation level in the catalyst layer, and MPL-substrate interface more precisely. In the present model the leveret function was implemented to correlate the capillary pressure and saturation relationship, which might not the best option to choose.

References

[1] Sadeghifar H, N Djilali, M Bahrami. Effect of Polytetrafluoroethylene (PTFE) and micro porous layer (MPL) on thermal conductivity of fuel cell gas diffusion layers: Modeling and experiments, J. Power Sources. 248 (2014) 632–641.

[2] Weber AZ, J Newman. Effects of Microporous Layers in Polymer Electrolyte Fuel Cells, J. Electrochem. Soc. 152 (2005) A677.

[3] Pasaogullari U, CY Wang, KS Chen. Two-Phase Transport in Polymer Electrolyte Fuel Cells with Bilayer Cathode Gas Diffusion Media, J. Electrochem. Soc. 152 (2005) A1574.

[4] Wang C-Y. Fundamental models for fuel cell engineering., Chem. Rev. 104 (2004) 4727–65.

[5] Sasmito AP, E Birgersson, AS Mujumdar. Numerical evaluation of various thermal management strategies for polymer electrolyte fuel cell stacks, Int. J. Hydrogen Energy. 36 (2011) 12991–13007.

[6] Alhazmi N, DB Ingham, MS Ismail, KJ Hughes, L Ma, M Pourkashanian. Effect of the anisotropic thermal conductivity of GDL on the performance of PEM fuel cells, Int. J. Hydrogen Energy. 38 (2013) 603–611.

[7] Ben Salah Y, Y Tabe, T Chikahisa. Two phase flow simulation in a channel of a polymer electrolyte membrane fuel cell using the lattice Boltzmann method, J. Power Sources. 199 (2012) 85–93.

[8] Falcucci G, E Jannelli, M Minutillo, S Ubertini. Fluid Dynamic Investigation of Channel Design in High Temperature PEM Fuel Cells, J. Fuel Cell Sci. Technol. 9 (2012) 021014.

[9] Hashemi F, S Rowshanzamir, M Rezakazemi. CFD simulation of PEM fuel cell performance: Effect of straight and serpentine flow fields, Math. Comput. Model. 55 (2012) 1540–1557.

[10] Jung S-P, C-I Lee, C-C Chen. An efficient method for numerical predictions of the performance characteristics of fuel cells. I. Model development and validation, J. Power Sources. 199 (2012) 179–194.

[11] Eikerling M. Water Management in Cathode Catalyst Layers of PEM Fuel Cells, J. Electrochem. Soc. 153 (2006) E58.

[12] Zamel N, X Li, J Shen. Numerical estimation of the effective electrical conductivity in carbon paper diffusion media, Appl. Energy. 93 (2012) 39–44.

[13] Lange KJ, P-C Sui, N Djilali. Pore scale modeling of a proton exchange membrane fuel cell catalyst layer: Effects of water vapor and temperature, J. Power Sources. 196 (2011) 3195–3203.

[14] Ramos-Alvarado B, A Hernandez-Guerrero, F Elizalde-Blancas, MW Ellis. Constructal flow distributor as a bipolar plate for proton exchange membrane fuel cells, Int. J. Hydrogen Energy. 36 (2011) 12965–12976.

[15] Springer TE, TA Zawodzinski, S Gottesfeld. Polymer Electrolyte Fuel Cell Model, J. Electrochem. Soc. 138 (1993) 2334–2342.

[16] Kermani MJ, JM Stockie. The effect of slip velocity on saturation for multiphase condensing mixtures in a PEM fuel cell, Int. J. Hydrogen Energy. 36 (2011) 13235–13240.

[17] Ju H, H Meng, C-Y Wang. A single-phase, non-isothermal model for PEM fuel cells, Int. J. Heat Mass Transf. 48 (2005) 1303–1315.

[18] Bapat CJ, ST Thynell. Anisotropic Heat Conduction Effects in Proton-Exchange Membrane Fuel Cells, J. Heat Transfer. 129 (2007) 1109.

[19] Matian M, A Marquis, N Brandon. Model based design and test of cooling plates for an air-cooled polymer electrolyte fuel cell stack, Int. J. Hydrogen Energy. 36 (2011) 6051–6066.

[20] Choi K-S, H-M Kim, HC Yoon, ME Forrest, P a. Erickson. Effects of ambient temperature and relative humidity on the performance of Nexa fuel cell, Energy Convers. Manag. 49 (2008) 3505–3511.

[21] Sasmito AP, E Birgersson, AS Mujumdar. A novel flow reversal concept for improved thermal management in polymer electrolyte fuel cell stacks, Int. J. Therm. Sci. 54 (2012) 242–252.

[22] Tolj I, D Bezmalinovic, F Barbir. Maintaining desired level of relative humidity throughout a fuel cell with spatially variable heat removal rates, Int. J. Hydrogen Energy. 36 (2011) 13105–13113.

[23] Jeon DH, KN Kim, SM Baek, JH Nam. The effect of relative humidity of the cathode on the performance and the uniformity of PEM fuel cells, Int. J. Hydrogen Energy. 36 (2011) 12499–12511.

[24] Tanuma T, S Kinoshita. Impact of Gas Diffusion Layers (GDLs) on Water Transport in PEFCs, J. Electrochem. Soc. 159 (2012) B150.

[25] Murakawa H, T Ueda, K Sugimoto, H Asano, N Takenaka. Measurement of water thickness in PEM fuel cells and analysis of gas velocity distributions, Nucl. Instruments Methods Phys. Res. Sect. A Accel. Spectrometers, Detect. Assoc. Equip. 651 (2011) 290–296.

[26] Zhang J, Y Tang, C Song, X Cheng, J Zhang, H Wang. PEM fuel cells operated at 0% relative humidity in the temperature range of 23–120°C, Electrochim. Acta. 52 (2007) 5095–5101.

[27] Shahsavari S, A Desouza, M Bahrami, E Kjeang. Thermal analysis of air-cooled PEM fuel cells, Int. J. Hydrogen Energy. 37 (2012) 18261–18271.

[28] Springer TE, S Gottesfeld. Pseudohomogeneous catalyst layer model for polymer electrolyte fuel cell, in: Symp. Model. Batter. Fuel Cells, Pennington, NJ, 1991: pp. 197–208.

[29] Broka K, P Ekdunge. Modelling the PEM fuel cell cathode, J. Appl. Electrochem. 27 (1997) 281–289.

[30] Sui PC, LD Chen, JP Seaba, Y Warrishi. Modeling and Optimization of a PEMFC Catalyst Layer, in: SAE Congr., 1999: pp. 61–70.

[31] Marr C, X Li. Composition and Performance modeling of catalyst layer in a proton exchange membrane fuel cell, J. Power Sources1. 77 (1999) 17–27.

[32] Wang ZH, CY Wang. Two-Phase Flow and Transport in the Interdigitated Air Cathode of Proton Exchange Membrane Fuel Cells, in: Proc. ASME Heat Transf. Div., 2000: pp. 27–33.

[33] Natarajan D, T Van Nguyen. A Two-Dimensional, Two-Phase, Multicomponent, Transient Model for the Cathode of a Proton Exchange Membrane Fuel Cell Using Conventional Gas Distributors, J. Electrochem. Soc. 148 (2001) A1324.

[34] Harvey D, JG Pharoah, K Karan. A comparison of different approaches to modelling the PEMFC catalyst layer, J. Power Sources. 179 (2008) 209–219.

[35] Sasmito AP, AS Mujumdar. Performance evaluation of a polymer electrolyte fuel cell with a dead-end anode: A computational fluid dynamic study, Int. J. Hydrogen Energy. 36 (2011) 10917–10933.

[36] Sun P, S Zhou, Q Hu, G Liang. Numerical Study of a 3D Two-Phase PEM Fuel Cell Model Via a Novel Automated Finite Element/Finite Volume Program Generator, Commun. Comput. Phys. 11 (2011) 65–98.

[37] Sadiq Al-Baghdadi M a. R. Performance comparison between airflow-channel and ambient air-breathing PEM fuel cells using three-dimensional computational fluid dynamics models, Renew. Energy. 34 (2009) 1812–1824.

[38] Wang CY, C Beckermann. A two-phase mixture model of liquid-gas flow and heat transfer in capillary porous media-I. Formulation, Int. J. Heat Mass Transf. 36 (1993) 2747–2758.

[39] Yan WM, DK Wu, XD Wang, AL Ong, DJ Lee, A Su. Optimal microporous layer for proton exchange membrane fuel cell, J. Power Sources. 195 (2010) 5731–5734.

[40] Spernjak D, J Fairweather, R Mukundan, T Rockward, RL Borup. Influence of the microporous layer on carbon corrosion in the catalyst layer of a polymer electrolyte membrane fuel cell, J. Power Sources. 214 (2012) 386–398.

[41] Chun JH, KT Park, DH Jo, JY Lee, SG Kim, SH Park, et al. Development of a novel hydrophobic/hydrophilic double micro porous layer for use in a cathode gas diffusion layer in PEMFC, Int. J. Hydrogen Energy. 36 (2011) 8422–8428.

[42] Schweiss R, M Steeb, PM Wilde, T Schubert. Enhancement of proton exchange membrane fuel cell performance by doping microporous layers of gas diffusion layers with multiwall carbon nanotubes, J. Power Sources. 220 (2012) 79–83.

[43] Kitahara T, T Konomi, H Nakajima. Microporous layer coated gas diffusion layers for enhanced performance of polymer electrolyte fuel cells, J. Power Sources. 195 (2010) 2202–2211.

[44] Gallo Stampino P, C Cristiani, G Dotelli, L Omati, L Zampori, R Pelosato, et al. Effect of different substrates, inks composition and rheology on coating deposition of microporous layer (MPL) for PEM-FCs, Catal. Today. 147 (2009) S30–S35.

[45] Nanjundappa A, AS Alavijeh, M El Hannach, D Harvey, E Kjeang. A customized framework for 3-D morphological characterization of microporous layers, Electrochim. Acta. 110 (2013) 349–357.

[46] Chan C, N Zamel, X Li, J Shen. Experimental measurement of effective diffusion coefficient of gas diffusion layer/microporous layer in PEM fuel cells, Electrochim. Acta. 65 (2012) 13–21.

[47] Burheim OS, H Su, S Pasupathi, JG Pharoah, BG Pollet. Thermal conductivity and temperature profiles of the micro porous layers used for the polymer electrolyte membrane fuel cell, Int. J. Hydrogen Energy. 38 (2013) 8437–8447.

[48] Ostadi H, P Rama, Y Liu, R Chen, XX Zhang, K Jiang. 3D reconstruction of a gas diffusion layer and a microporous layer, J. Memb. Sci. 351 (2010) 69–74.

[49] Bruggeman DAG. Calculation of various physics constants in heterogenous substances I dielectricity constants and conductivity of mixed bodies from isotropic substances, Ann. Der Phys. 24 (1935) 636–664.

[50] Neale GH, WK Nader. Prediction of transport processes within porous media: diffusive flow processes within a homogeneous swarm of spherical particles, AIChE J. 19 (1973) 112–119.

[51] Mezedur MM, M Kaviany, W Moore. Effect of pore structure, randomness and size on effective mass diffusivity, AIChE J. 48 (2002) 15–24.

[52] Tomadakis MM, SV Sotirchos. Ordinary and transition regime diffusion in random fiber structures, AIChE J. 39 (1993) 397–412.

[53] Zamel N, X Li, J Shen. Correlation for the Effective Gas Diffusion Coefficient in Carbon Paper Diffusion Media, Energy & Fuels. 23 (2009) 6070–6078.

[54] Sadeghifar H, M Bahrami, N Djilali. A statistically-based thermal conductivity model for fuel cell Gas Diffusion Layers, J. Power Sources. 233 (2013) 369–379.

[55] Cho KT, MM Mench. Effect of material properties on evaporative water removal from polymer electrolyte fuel cell diffusion media, J. Power Sources. 195 (2010) 6748–6757.

[56] Ziegler C, S Thiele, R Zengerle. Direct three-dimensional reconstruction of a nanoporous catalyst layer for a polymer electrolyte fuel cell, J. Power Sources. 196 (2011) 2094–2097.

[57] Zils S, M Timpel, T Arlt, a. Wolz, I Manke, C Roth. 3D Visualisation of PEMFC Electrode Structures Using FIB Nanotomography, Fuel Cells. 10 (2010) 966–972.

[58] Epting WK, J Gelb, S Litster. Resolving the Three-Dimensional Microstructure of Polymer Electrolyte Fuel Cell Electrodes using Nanometer-Scale X-ray Computed Tomography, Adv. Funct. Mater. 22 (2012) 555–560.

[59] Kuroda CS, Y Yamazaki. Novel Technique of MEA Sample Preparation Using a Focused Ion Beam for Scanning Electron Microscope Investigation, ECS Trans. 11 (2007) 509–516.

[60] Takeya S, a. Yoneyama, J Miyamoto, Y Gotoh, K Ueda, K Hyodo, et al. Phase-contrast X-ray imaging of the gas diffusion layer of fuel cells, J. Synchrotron Radiat. 17 (2010) 813–816.

[61] Gaiselmann G, C Tötzke, I Manke, W Lehnert, V Schmidt. 3D microstructure modeling of compressed fiber-based materials, J. Power Sources. 257 (2014) 52–64.

[62] Tötzke C, G Gaiselmann, M Osenberg, J Bohner, T Arlt, H Markötter, et al. Three-dimensional study of compressed gas diffusion layers using synchrotron X-ray imaging, J. Power Sources. 253 (2014) 123–131.

[63] Odaya S, RK Phillips, Y Sharma, J Bellerive, a. B Phillion, M Hoorfar. X-ray Tomographic Analysis of Porosity Distributions in Gas Diffusion Layers of Proton Exchange Membrane Fuel Cells, Electrochim. Acta. 152 (2015) 464–472.

[64] Kim S-G, S-J Lee. Tomographic analysis of porosity variation in gas diffusion layer under freeze-thaw cycles, Int. J. Hydrogen Energy. 37 (2012) 566–574.

[65] Flückiger R, F Marone, M Stampanoni, A Wokaun, FN Büchi. Investigation of liquid water in gas diffusion layers of polymer electrolyte fuel cells using X-ray tomographic microscopy, Electrochim. Acta. 56 (2011) 2254–2262.

[66] Markötter H, K Dittmann, J Haußmann, R Alink, D Gerteisen, H Riesemeier, et al. Electrochemistry Communications In fl uence of local carbon fi bre orientation on the water transport in the gas diffusion layer of polymer electrolyte membrane fuel cells, Electrochem. Commun. 51 (2015) 133–136.

[67] Lee J, R Yip, P Antonacci, N Ge, T Kotaka, Y Tabuchi, et al. Synchrotron Investigation of Microporous Layer Thickness on Liquid Water Distribution in a PEM Fuel Cell, 162 (2015).

[68] Eller J, J Roth, F Marone, M Stampanoni, A Wokaun, FN Büchi. Implications of polymer electrolyte fuel cell exposure to synchrotron radiation on gas diffusion layer water distribution, J. Power Sources. 245 (2014) 796–800.

[69] Litster S, WK Epting, E a. Wargo, SR Kalidindi, EC Kumbur. Morphological Analyses of Polymer Electrolyte Fuel Cell Electrodes with Nano-Scale Computed Tomography Imaging, Fuel Cells. (2013) n/a–n/a.

[70] Wargo E a., T Kotaka, Y Tabuchi, EC Kumbur. Comparison of focused ion beam versus nano-scale X-ray computed tomography for resolving 3-D microstructures of porous fuel cell materials, J. Power Sources. 241 (2013) 608–618.

[71] El Hannach M, R Singh, N Djilali, E Kjeang. Micro-porous layer stochastic reconstruction and transport parameter determination, J. Power Sources. 282 (2015) 58–64.

[72] Andisheh-tadbir M, M El, E Kjeang. An analytical relationship for calculating the effective diffusivity of micro-porous layers, Int. J. Hydrogen Energy. 40 (2015) 10242–10250.

[73] Andisheh-Tadbir M, E Kjeang, M Bahrami. Thermal conductivity of microporous layers : Analytical modeling and experimental validation, J. Power Sources. 296 (2015) 344–351.

[74] Merida W. Porous Transport Layer Degradation, in: X.Z. Yuan (Ed.), PEM Fuel Cell Fail. Mode Anal., CRC Press, 2012.

[75] Wu J, XZ Yuan, JJ Martin, H Wang, J Zhang, J Shen, et al. A review of PEM fuel cell durability: Degradation mechanisms and mitigation strategies, J. Power Sources. 184 (2008) 104–119.

[76] Wong KH, E Kjeang. Mitigation of chemical membrane degradation in fuel cells: understanding the effect of cell voltage and iron ion redox cycle.pdf, ChemSusChem. 8 (2015) 1072–1082.

[77] Venkatesan SV, C Lim, E Rogers, S Holdcroft, E Kjeang. Evolution of water sorption in catalyst coated membranes subjected to combined chemical and mechanical degradation, Phys. Chem. Chem. Phys. 17 (2015) 13872–13881.

[78] Sadeghi Alavijeh A, M-A Goulet, R Khorsany, J Ghataurah, C Lim, M Lauritzen, et al. Decay in Mechanical Properties of Catalyst Coated Membranes Subjected to Combined Chemical and Mechanical Membrane Degradation, Fuel Cells. (2014) Under Review.

[79] Macauley N, L Ghassemzadeh, C Lim, M Watson, J Kolodziej, M Lauritzen, et al. Pt Band Formation Enhances the Stability of Fuel Cell Membranes, ECS Electrochem. Lett. 2 (2013) F33–F35.

[80] Kangasniemi KH, D a. Condit, TD Jarvi. Characterization of Vulcan Electrochemically Oxidized under Simulated PEM Fuel Cell Conditions, J. Electrochem. Soc. 151 (2004) E125.

[81] Reiser C a., L Bregoli, TW Patterson, JS Yi, JD Yang, ML Perry, et al. A Reverse-Current Decay Mechanism for Fuel Cells, Electrochem. Solid-State Lett. 8 (2005) A273.

[82] Mench MM, EC Kumbur, TN Veziroglu, EC Kumbar, N Veziroglu. Polymer Electrolyte Fuel Cell Degradation, Elsevier, Academic Press, Oxford, 2012.

[83] De Bruijn F a., V a T Dam, GJM Janssen. Review: Durability and degradation issues of PEM fuel cell components, Fuel Cells. 8 (2008) 3–22.

[84] Yousfi-Steiner N, P Moçotéguy, D Candusso, D Hissel. A review on polymer electrolyte membrane fuel cell catalyst degradation and starvation issues: Causes, consequences and diagnostic for mitigation, J. Power Sources. 194 (2009) 130–145.

[85] Zhang S, X-Z Yuan, JNC Hin, H Wang, KA Friedrich, M Schulze. A review of platinum-based catalyst layer degradation in proton exchange membrane fuel cells, J. Power Sources. 194 (2009) 588–600.

[86] Yu Y, H Li, H Wang, X-Z Yuan, G Wang, M Pan. A review on performance degradation of proton exchange membrane fuel cells during startup and shutdown processes: Causes, consequences, and mitigation strategies, J. Power Sources. 205 (2012) 10–23.

[87] Borup R, J Meyers, B Pivovar, YS Kim, R Mukundan, N Garland, et al. Scientific Aspects of Polymer Electrolyte Fuel Cell Durability and Degradation, (2007) 3904–3951.

[88] El Hannach M, E Kjeang. Stochastic Microstructural Modeling of PEFC Gas Diffusion Media, J. Electrochem. Soc. 161 (2014) F951–F960.

[89] Wu J, JJ Martin, FP Orfino, H Wang, C Legzdins, X-Z Yuan, et al. In situ accelerated degradation of gas diffusion layer in proton exchange membrane fuel cellPart I: Effect of elevated temperature and flow rate, J. Power Sources. 195 (2010) 1888–1894.

[90] Lee C, W Mérida. Gas diffusion layer durability under steady-state and freezing conditions, J. Power Sources. 164 (2007) 141–153.

[91] Enz S, T a. Dao, M Messerschmidt, J Scholta. Investigation of degradation effects in polymer electrolyte fuel cells under automotive-related operating conditions, J. Power Sources. 274 (2015) 521–535.

[92] Schmittinger W, A Vahidi. A review of the main parameters influencing long-term performance and durability of PEM fuel cells, J. Power Sources. 180 (2008) 1–14.

[93] Borup RL, JR Davey, FH Garzon, DL Wood, M a. Inbody. PEM fuel cell electrocatalyst durability measurements, J. Power Sources. 163 (2006) 76–81.

[94] Hou J, H Yu, S Zhang, S Sun, H Wang, B Yi, et al. Analysis of PEMFC freeze degradation at −20°C after gas purging, J. Power Sources. 162 (2006) 513–520.

[95] Chang H-M, C-W Lin, M-H Chang, H-R Shiu, W-C Chang, F-H Tsau. Optimization of polytetrafluoroethylene content in cathode gas diffusion layer by the evaluation of compression effect on the performance of a proton exchange membrane fuel cell, J. Power Sources. 196 (2011) 3773–3780.

[96] Chun JH, DH Jo, SG Kim, SH Park, CH Lee, SH Kim. Improvement of the mechanical durability of micro porous layer in a proton exchange membrane fuel cell by elimination of surface cracks, Renew. Energy. 48 (2012) 35–41.

[97] Erkan S. Effect of Different Construction Materials on Proton Exchange Membrane Fuel, (2005) 13–15.

[98] Gulzow E, M Schulze, N Wanger, T Kaz, A Schneider, R Reissner. New dry preparation technique for membrane electrode assemblies for PEM fuel cells, Fuel Cells Bull. 15 (n.d.).

[99] Daud WR., AB Mohamad, AAH Kadhum, R Chebbi, SE Iyuke. Performance optimisation of PEM fuel cell during MEA fabrication, Energy Convers. Manag. 45 (2004) 3239–3249.

[100] Frey T, M Linardi. Effects of membrane electrode assembly preparation on the polymer electrolyte membrane fuel cell performance, Electrochim. Acta. 50 (2004) 99–105.

[101] Wang H, H Li, X-Z Yuan, eds. PEM Fuel Cell Failure Mode Analysis, CRC Press, Taylor & Francis Group, Boca Raton, 2012.

[102] Young a. P, J Stumper, S Knights, E Gyenge. Ionomer Degradation in Polymer Electrolyte Membrane Fuel Cells, J. Electrochem. Soc. 157 (2010) B425.

[103] Kumar RJF, V Radhakrishnan, P Haridoss. Effect of electrochemical aging on the interaction between gas diffusion layers and the flow field in a proton exchange membrane fuel cell, Int. J. Hydrogen Energy. 36 (2011) 7207–7211.

[104] Sadeghi E, N Djilali, M Bahrami. Effective thermal conductivity and thermal contact resistance of gas diffusion layers in proton exchange membrane fuel cells. Part 2: Hysteresis effect under cyclic compressive load, J. Power Sources. 195 (2010) 8104–8109.

[105] Bazylak a., D Sinton, Z-S Liu, N Djilali. Effect of compression on liquid water transport and microstructure of PEMFC gas diffusion layers, J. Power Sources. 163 (2007) 784–792.

[106] Chun JH, KT Park, DH Jo, JY Lee, SG Kim, ES Lee, et al. Determination of the pore size distribution of micro porous layer in PEMFC using pore forming agents under various drying conditions, Int. J. Hydrogen Energy. 35 (2010) 11148–11153.

[107] Carslaw HS, JC Jaeger. Conduction of Heat in Solids, Second edi, Oxford University Press, London, 1959.

[108] Hirschfelder JO, RB Curtiss. Molecular Theory of Gases and Liquids, John Wiley, New York, 1954.

[109] Pollard WG, RD Present. On gaseous self-diffusion in long capillary tubes, Phys. Rev. 73 (1948) 762–774.

[110] Marrero TR, EA Mason. Gaseous diffusion coefficients.pdf, J. Phys. Chem. Ref. Data. 1 (1972) 3–118.

[111] Kast W, CR Hohenthanner. Mass transfer within the gas-phase of porous media, Int. J. Heat Mass Transf. 43 (2000) 807–823.

[112] Zamel N, J Becker, A Wiegmann. Estimating the thermal conductivity and diffusion coefficient of the microporous layer of polymer electrolyte membrane fuel cells, J. Power Sources. 207 (2012) 70–80.

[113] Nam JH, M Kaviany. Effective diffusivity and water-saturation distribution in single- and two-layer PEMFC diffusion medium, Int. J. Heat Mass Transf. 46 (2003) 4595–4611.

[114] Park S, JW Lee, BN Popov. Effect of PTFE content in microporous layer on water management in PEM fuel cells, J. Power Sources. 177 (2008) 457–463.

[115] Tseng CJ, SK Lo. Effects of microstructure characteristics of gas diffusion layer and microporous layer on the performance of PEMFC, Energy Convers. Manag. 51 (2010) 677–684.

[116] Andisheh-Tadbir M, M El Hannach, E Kjeang, M Bahrami. An analytical relationship for calculating the effective diffusivity of micro-porous layers, Int. J. Hydrogen Energy. (2015).

[117] Kaganer MG. Thermal Insulation in Cryogenic Engineering, Israel Program for Scientific Translation, 1969.

[118] Bahrami M, MM Yovanovich, JR Culham. Thermal Joint Resistances of Conforming Rough Surfaces with Gas-Filled Gaps, J. Thermophys. Heat Transf. 18 (2004).

[119] Kwon J-S, CH Jang, H Jung, T-H Song. Effective thermal conductivity of various filling materials for vacuum insulation panels, Int. J. Heat Mass Transf. 52 (2009) 5525–5532.

[120] Jennings SG. The mean free path in air, J. Aerosol Sci. 19 (1988) 159–166.

[121] Hsu CT, P Cheng, KW Wong. Modified Zehner-Schlunder models for stagnant thermal conductivity of porous media, Int. J. Heat Mass Transf. 37 (1994) 2751–2759.

[122] Johnson KL. Contact Mechanics, Cambridge University Press, 1985.

[123] SIGRACET GDL 24 & 25 Series Gas Diffusion Layer, Germany, 2009.

[124] SIGRACET GDL 34 & 35 Series Gas Diffusion Layer, Germany, 2007.

[125] Silvia WP, CMDP. Silvia. LAB Fit Curve Fitting Software (Nonlinear Regression and Treatment of Data Program), (2015).

[126] Sprawls P. The Physical Principles of Medical Imaging, 2nd ed., Medical Physics Pub Corp, 1995.

[127] Ostadi H, P Rama, Y Liu, R Chen, XX Zhang, K Jiang. Influence of threshold variation on determining the properties of a polymer electrolyte fuel cell gas diffusion layer in X-ray nano-tomography, Chem. Eng. Sci. 65 (2010) 2213–2217.

[128] Rasband WS. ImageJ, (n.d.).

[129] Hubbell JH, SM Seltzer. Tables of X-Ray Mass Attenuation Coefficients and Mass Energy-Absorption Coefficients (version 1.4), Natl. Inst. Stand. Technol. Gaithersburg, MD. (2004).

[130] Wood D, R Mukundan, R Borup. In-plane mass-transport studies of GDL variation using the segmented cell approach, ECS Trans. 25 (2009) 1495–1506.

[131] Mukundan R, JR Davey, T Rockward, JS Spendelow, BS Pivovar, DS Hussey, et al. Imaging of water profiles in PEM fuel cells using neutron radiography: effect of operating conditions and GDL composition, ECS Trans. 11 (2007) 411–422.

[132] Price DM, M Jarratt. Thermal conductivity of PTFE and PTFE composites, 393 (2002) 231–236.

[133] Andisheh-Tadbir M, F Orfino, E Kjeang. Three-dimensional, phase distinguished nano-scale X-ray computed tomography of micro-porous layers for fuel cells, Submitt. Publ. (2015).

[134] Yuan Y, TR Lee. Contact Angle and Wetting Properties, in: G. Bracco, B. Holst (Eds.), Surf. Sci. Tech., Springer, Berlin, 2013.

[135] Mench M. Fuel Cell Engines.pdf, John Wiley & Sons, Inc., Hoboken, New Jersey, 2008.

[136] Matian M, a Marquis, D Brett, N Brandon. An experimentally validated heat transfer model for thermal management design in polymer electrolyte membrane fuel cells, Proc. Inst. Mech. Eng. Part A J. Power Energy. 224 (2010) 1069–1081.

[137] Kergourlay G, S Kouidri, GW Rankin, R Rey. Experimental investigation of the 3D unsteady flow field downstream of axial fans, Flow Meas. Instrum. 17 (2006) 303–314.

[138] Pharoah JG, OS Burheim. On the temperature distribution in polymer electrolyte fuel cells, J. Power Sources. 195 (2010) 5235–5245.

[139] Alofi A, GP Srivastava. Thermal conductivity of graphene and graphite, Phys. Rev. B. 87 (2013) 115421.

[140] Wen C-Y, Y-S Lin, C-H Lu, T-W Luo. Thermal management of a proton exchange membrane fuel cell stack with pyrolytic graphite sheets and fans combined, Int. J. Hydrogen Energy. 36 (2011) 6082–6089.

[141] ANSYS Fluent User's Guide, 2010.

[142] Perry R, DW Green, JO Maloney. Perry's Chemical Engineers' Handbook, 6th ed., McGraw-Hill, New York, 1984.

[143] Cheema TA, SMJ Zaidi, SU Rahman. Three dimensional numerical investigations for the effects of gas diffusion layer on PEM fuel cell performance, Renew. Energy. 36 (2011) 529–535.

[144] Meng H, C-Y Wang. Electron Transport in PEFCs, J. Electrochem. Soc. 151 (2004) A358.

[145] Adzakpa KP, J Ramousse, Y Dubé, H Akremi, K Agbossou, M Dostie, et al. Transient air cooling thermal modeling of a PEM fuel cell, J. Power Sources. 179 (2008) 164–176.

[146] Chupin S, T Colinart, S Didierjean, Y Dubé, K Agbossou, G Maranzana, et al. Numerical investigation of the impact of gas and cooling flow configurations on current and water distributions in a polymer membrane fuel cell through a pseudo-two-dimensional diphasic model, J. Power Sources. 195 (2010) 5213–5227.

[147] Zahi I, C Rossi, V Faucheux. Micro PEM fuel cell current collector design and optimization with CFD 3D modeling, Int. J. Hydrogen Energy. 36 (2011) 14562–14572.

[148] Udell KS. Heat transfer in porous media considering phase change and capillarity-the heat pipe effect, Int. J. Heat Mass Transf. 28 (1985) 485–495.

[149] Leverett MC. Capillary behavior in porous solids, Am. Inst. Mining, Metall. Pet. Eng. 142 (1941) 152–162.

[150] Siegel NP. Development and Validation of a Computational Model for a Proton Exchange Membrane Fuel Cell, Virginia Polytechnic Institute and State University, 2004.